

A BIFURCATED STUDY OF SPIN-LATTICE RELAXATION INFORMATION
IN NUCLEAR MAGNETIC RESONANCE IMAGING:
QUANTITATIVE ANALYSIS WITH CONVENTIONAL TECHNIQUES AND THE
UNCONVENTIONAL STIMULATED ECHO IMAGING TECHNIQUE

By

WILLIAM SATTIN

A DISSERTATION PRESENTED TO THE GRADUATE SCHOOL
OF THE UNIVERSITY OF FLORIDA IN
PARTIAL FULFILLMENT OF THE REQUIREMENTS
FOR THE DEGREE OF DOCTOR OF PHILOSOPHY

UNIVERSITY OF FLORIDA

1985

Copyright 1985

by
William Sattin

For Wendy and Emily, my life

ACKNOWLEDGMENTS

There are many people to whom I am indebted for their assistance in accomplishing this work. Let me begin with my high school physics instructor, Sedgewick Duckworth. The love of life through understanding which he instilled within me shall never waver.

I sincerely appreciate the freedom and guidance offered me by my advisor, Dr. Katherine N. Scott. Her door is always open to me.

I thank Dr. Alan M. Jacobs for seeing me through this work, literally, from start to finish. Also, I am grateful to have had the chance to interact with Dr. E. Raymond Andrew, for he embodies the wisdom, wonder, and charm of the discipline of nuclear magnetic resonance.

The other members of my committee contributed in a variety of ways to strengthen this work, as did my fellow students. At appropriate points in the text I acknowledged those individuals who made specific contributions.

Special thanks go to the Department of Radiology for partial financial support. Additional financial support was supplied by NIH grant P41-RR-02278.

TABLE OF CONTENTS

	<u>PAGE</u>
ACKNOWLEDGMENTS.....	iv
LIST OF TABLES.....	vi
LIST OF FIGURES.....	vii
ABSTRACT.....	ix
CHAPTER	
I INTRODUCTION.....	1
II UTILIZATION OF THE SPIN-LATTICE RELAXATION TIME IN NMR IMAGING.....	5
Introduction.....	5
Theory of Spin-Lattice Relaxation.....	5
Clinical Use of Spin-Lattice Relaxation.....	8
III INVESTIGATION INTO T1 DETERMINATION ON A WHOLE BODY NMR IMAGER.....	10
Introduction.....	10
Methods and Materials.....	13
Results.....	44
Discussion.....	54
IV EXPLOITING THE STIMULATED ECHO IN NMR IMAGING..	71
Introduction.....	71
Theory.....	74
Materials and Methods.....	91
Results.....	121
Discussion.....	138
V SUMMARY AND CONCLUSIONS.....	147
REFERENCES.....	151
BIOGRAPHICAL SKETCH.....	155

LIST OF TABLES

<u>NUMBER</u>	<u>TABLE</u>	<u>PAGE</u>
3-1	Concentration of Copper Sulfate Doped Water and Resultant Spin-Lattice Relaxation Time for Phantom Material.....	17
3-2	Typical Raw Data Acquired for T1 Determination.....	33
4-1	Four-Step Phase Cycling Used in Stimulated Echo Imaging.....	101

LIST OF FIGURES

<u>NUMBER</u>	<u>TABLE</u>	<u>PAGE</u>
3-1	Phantom used for all T1 measurements.....	15
3-2	Field mapping apparatus.....	20
3-3	Spatial homogeneity mapping of the main magnetic field.....	21
3-4	Spatial homogeneity mapping of the transmitted rf field.....	22
3-5	Color NMR images of phantom.....	29
3-6	Examples of fitted data sets yielding good T1 estimates.....	35
3-7	Examples of fitted data sets which yielded poor T1 estimates.....	36
3-8	Sample computer output of data correlation program.....	39
3-9	Hypothetical output of data correlation program.....	42
3-10	Representative data indicating independence to position in field-of-view.....	47
3-11	Representative data indicating independence to actual T1 value.....	48
3-12	Representative data indicating independence to number of images.....	50
3-13	Summary of results.....	51
3-14	Effect of rf attenuating material upon measurement precision and accuracy.....	63
4-1	Basic stimulated echo imaging sequence.....	78
4-2	The formation of a primary echo.....	79
4-3	The formation of a stimulated echo.....	86

4-4	The evaluation of a residual gradient.....	97
4-5	Effect of residual gradients on image formation.....	99
4-6	The extended stimulated echo imaging sequence.....	108
4-7	The tip angle reduced T1 (TART) imaging sequence.....	112
4-8	The formation of a series of TART images.....	114
4-9	The stimulated echo-diffusion coefficient imaging sequence.....	120
4-10	The response to the stimulated echo sequence.....	122
4-11	The William Tell phantom.....	124
4-12	The quantitative use of the STE image.....	126
4-13	A water-lipid image of a hen's egg.....	128
4-14	A STE chemical shift image.....	130
4-15	An extended STE multiecho series of images....	132
4-16	A comparison of the spin echo image and the primary echo image.....	134
4-17	A series of TART images.....	136

Abstract of Dissertation Presented to the
Graduate School of the University of Florida in Partial
Fulfillment of the Requirements for the Degree of Doctor of
Philosophy

A BIFURCATED STUDY OF SPIN-LATTICE RELAXATION INFORMATION
IN NUCLEAR MAGNETIC RESONANCE IMAGING:
QUANTITATIVE ANALYSIS WITH CONVENTIONAL TECHNIQUES AND THE
UNCONVENTIONAL STIMULATED ECHO IMAGING TECHNIQUE

By

William Sattin

December 1985

Chairman: Katherine N. Scott

Major Department: Nuclear Engineering Sciences

This work is comprised of two separate investigations, both related to spin-lattice relaxation, or T_1 , information in nuclear magnetic resonance (NMR) imaging. One study explored the ability of commercially available NMR imagers to accurately and precisely determine the T_1 value of imaged objects. The specific goal was to evaluate empirically the advice found in the NMR spectroscopy literature on T_1 determination, and how well this advice applied to NMR imaging with its unique set of experimental constraints. The primary conclusion was that if one wished to obtain a direct estimate of the actual T_1 value in an object which might be

within a spatially inhomogeneous radio frequency field, the most accurate, precise, and time-effective technique to use was three fast inversion recovery images, with suitably chosen values of the inverting time, whose signal intensities were fitted by a three-parameter exponential function.

The other study concerned itself with the detailed theory, practical considerations, and possible applications of the stimulated echo (STE) in NMR imaging. Whereas conventional NMR imaging techniques rely upon the spin echo, which has solely T2 relaxation weighting unless the NMR signal is saturated, STE NMR imaging is unique in that the STE has intrinsic T1 weighting. Possible applications abound. In addition to generating T1 contrast images, it is possible to calculate quantitative T1 information from a series of STE images. Additionally, STE images effectively enhance objects with long T1 values over those with shorter T1 values, whereas spin echo images do not. Also, it was demonstrated that the STE easily integrates into chemical shift imaging schemes. Of prime interest are two STE imaging sequences which permit the acquisition of a series of STE images within one imaging sequence, where each image has progressively increased T1 weighting. Finally, a method of in vivo determination of diffusion coefficients is proposed, which utilizes STE imaging to lessen the effect of T2 weighting.

CHAPTER I INTRODUCTION

From modest but promising beginnings in the 1940s and 1950s, nuclear magnetic resonance (NMR) spectroscopy has developed into an important research tool. The first applications of NMR yielded insights into the properties of the atomic nucleus. Early in its history, NMR spectroscopy was adapted from the sole use by physicists, to the realm of chemists, who saw the potential of the chemical shift phenomenon as a structural probe. This first useful parameter has now been supplemented by many other experimentally accessible quantities, making NMR a powerful and versatile technique that yields information related to molecular structure, interactions, and dynamics. Most new applications of NMR have been derived from parallel improvements in instrumentation and methods, resulting in applications in physics, chemistry, biology, geology, and medicine. Particular applications include two-dimensional Fourier transform NMR [Au76], high resolution NMR in solids [Ha76], chemically induced dynamic nuclear polarization [Ka78], multiple quantum NMR [Ve77], and NMR imaging [La73]. The conclusions of the present investigation are particularly applicable to NMR imaging.

The technique of NMR imaging is one that interests not only scientists, but also nonscientists, for it promises to provide a safe and noninvasive method for diagnosing dysfunction or disease in human tissue. Most whole body NMR imagers in use today detect the NMR signals from the protons in the object. In in vivo applications the major source of protons is water. Many applications of NMR imaging are based on the fact that different regions of the object (i.e. different tissues or organs) have different water contents and different values of the characterizing times, T_1 and T_2 . For soft tissue differentiation, where relative water content is essentially a constant, it is the wide variability in the values of T_1 and T_2 which makes possible images with anatomical detail, and more importantly, images which contain pathological detail. These images, which contain pathological detail, are of particular interest because of the proposal [Da71] that T_1 values of water protons in cancerous or damaged cells are longer than those of protons in normal cells [Le81]. The present investigation explored the role of T_1 , the spin-lattice relaxation time, in NMR imaging.

Chapter II offers a brief account of the theory of spin-lattice relaxation and discusses the impetus for the present investigation: the dual role of T_1 in NMR imaging. One role of T_1 in NMR is qualitative in nature, T_1 as a source of image contrast. The other role is quantitative, for T_1 values have the potential of being diagnostic.

Chapter III explores the ability of commercially available NMR imagers to accurately and precisely determine the T1 value of imaged objects. The specific goal was to evaluate empirically the advice on T1 determination found in the NMR spectroscopy literature and to see how well it applied to NMR imaging with its unique set of experimental constraints. The primary result presented in Chapter III is concerned with the direct estimate of the actual T1 value in an object which may be within a spatially inhomogeneous rf field. The most accurate, precise, and time effective technique to use is three fast inversion recovery images, with suitably chosen values of the inverting time, whose signal intensities are fitted by a three-parameter exponential function.

Chapter IV presents the detailed theory, practical considerations, and, by way of examples, the possible applications of the stimulated echo (SIE) [HaSO] in NMR imaging. Whereas conventional NMR imaging techniques rely upon the spin echo, SIE NMR imaging incorporates the unique T1 dependence of the SIE. The results reported in Chapter IV take the form of specific applications of the STE to NMR imaging. First, it is shown that in addition to generating T1 contrast images, it is possible to calculate quantitative T1 information from a series of images. Second, a novel application of the T1 weighted STE image is demonstrated, either the enhancement or the suppression of elements in the object with different T1 values. Third, it is shown that the

STE is easily integrated into chemical shift imaging schemes. Fourth, two stimulated echo imaging methods are presented which permit the acquisition of a series of STE images within one imaging sequence, where each image has progressively increased T1 weighting. Finally, a method of in vivo determination of molecular translational self-diffusion coefficients, which utilizes STE imaging to lessen the effect of T2 weighting, is proposed.

In the final chapter, Chapter V, a summary of results is presented, as well as the final conclusions, which identify the thread which runs through this entire work, a thread that, at once, connects and binds.

CHAPTER II UTILIZATION OF THE SPIN-LATTICE RELAXATION TIME IN NMR IMAGING

Introduction

The two NMR relaxation times, T1 and T2, play a pivotal role in the understanding of the organization of biological systems at the molecular level in general, and in NMR imaging in particular. Differences in proton NMR relaxation times of normal and pathological tissue are the key to NMR image contrast and the discrimination of disease, a fact responsible for their widespread use as diagnostic parameters in clinical NMR imaging. T1 and T2 directly affect the selection of imaging pulse sequence timing parameters, and consequently, the total imaging times and patient throughput. Also, T1 may influence the choice of the optimum operational magnetic field strength for NMR imaging, due to T1's significant variation with frequency [Bo84].

Theory of Spin-Lattice Relaxation

A detailed description of the complete theory of spin-lattice relaxation is beyond the scope of this work, rather, those elements of the theory crucial to the understanding of this investigation are presented. Consider an ensemble of identical, interacting atoms, whose nuclei contain either an odd number of protons, an odd number of neutrons, or both. At room temperature, the majority of

nuclei will reside in the lowest energy level, the so called ground state. In the absence of a magnetic field the nuclear spin states are degenerate all with the same energy, though the application of a magnetic field removes this degeneracy. Additionally, the nuclei will precess about the direction of the applied magnetic field, a concept which is more fully explained in Chapter IV. Radiofrequency electromagnetic radiation stimulation will cause the nuclei to absorb energy, raising them to an excited state. The nuclei in an excited state can return to the ground state only by dissipating the excess energy to their surroundings. Return to the ground state, or relaxation, also requires a stimulating rf field. The fields causing this spin-lattice relaxation are provided by the surrounding nuclear environment, the so-called lattice. The term, lattice, was first introduced to describe the positions of molecules in crystalline solids, but has since been extended to other phases in addition to the solid phase, and now simply indicates the magnetic environment of the nuclei.

The rf fields provided by the lattice for relaxation result from the presence of other magnetic nuclei, paramagnetic ions and molecules, and molecular magnetism which is the result of the fast rotation of electronic charges. The most common source of lattice fields is the dipole field produced by neighboring magnetic nuclei. For example, in the water molecule, one of the hydrogen nuclei produces a magnetic field, thus affecting the adjacent

proton. The lattice field must fluctuate to transfer energy effectively from the excited proton to the lattice. Thus, these fluctuations must occur at a rate which matches the transitional frequency of the excited protons.

In liquids, the fluctuations in the lattice field are the result of molecules undergoing Brownian motion, which may be either translational or rotational in nature. Both intramolecular and intermolecular relaxation processes occur. With intramolecular relaxation, energy is transferred between nuclei within the same molecule, whereas intermolecular relaxation involves nuclei of different molecules. The protons in water and lipid, the primary sources of protons in the human body, relax predominantly by the intramolecular dipole-dipole mechanism.

Typically, the average rate at which the molecules reorient themselves is related to the size of the molecule. Small molecules, such as water, reorient more quickly than larger molecules, such as lipids, with correlation times on the order of 10^{-11} and 10^{-8} seconds respectively. Indeed, the large macromolecules, such as DNA and proteins, tumble rather slowly, with correlation times three or four orders of magnitude slower than lipid. The frequency of rotation for the medium-sized molecules, such as lipids, most closely corresponds to the transitional frequency of the excited protons, at typical nuclear magnetic resonance magnetic field strengths. Hence, lipid-based protons will relax faster than water-based protons, which rotate at a frequency

that is typically greater than the transitional frequency of the protons. Similarly, the macromolecules are inefficient in causing relaxation, for they rotate at frequencies which are much less than the transitional frequency.

Efficient relaxation correlates to short T1 values, whereas inefficient relaxation results in long T1 values. For example, in fat, which has a high lipid content, T1 is typically of the order of a few hundred milliseconds, yet the T1 of pure water is about three seconds. Although free water relaxes slowly, the water in biological tissue tends to relax much faster, with typical T1 values of only several hundred milliseconds. In an attempt to explain this phenomenon, it was postulated that a fraction of water in tissues is bound to the surface of proteins [Zi57]. Hence, the motion of bound water is reduced, thus more closely matching the transitional frequency of the protons. This enhanced relaxation results in shorter T1 values. In practice, an equilibrium exists between bound and free water. It is thought that this equilibrium is perturbed in certain pathological conditions, resulting in the clinically observed elevation in T1 values of certain tumors [Da71].

Clinical Use of Spin-Lattice Relaxation

Although spin density images are useful in a number of clinical situations, there is nearly universal agreement that images which depend significantly on the relaxation parameters T1 and T2 show considerably greater soft tissue contrast. This increased contrast allows improved

differentiation and recognition of anatomical detail and helps to demonstrate and assess mass effects [St85].

The explanation for this increased contrast lies in the fact that relaxation times of tissue cover a wider range of values than the range of proton densities in the same tissues. For example, at low magnetic field strengths, the difference in T1 between liver and kidney is over 50%, whereas the difference in proton density is less than 10%. Perhaps more important is the large alteration in relaxation time that occurs in various disease states, even when the proton density itself is not altered significantly. For example, tumors often have T1 values which are increased by 200% or 300% compared to the surrounding normal tissue.

The determination of absolute numbers for T1 promises to aid in tissue specification, although there is still considerable variability of values being reported from investigator to investigator. Recently, Bottomley et al. have collated a vast body of relaxation time information for the purpose of establishing the range of normal values [Bo84]. Deficiencies in measurement techniques were identified as a major source of data irreproducibility. Additionally, there is significant overlap between normal and abnormal tissue in some types of pathology, for example, diffuse liver disease [Do82]. Thus, to date, measured T1 values are still too variable, and have yet to improve significantly the tissue specificity of NMR imaging.

CHAPTER III
INVESTIGATION INTO T1 DETERMINATION ON A
WHOLE BODY NMR IMAGER

Introduction

Proton nuclear magnetic resonance (NMR) imaging may yield both qualitative images which are evaluated visually and quantitative information which is evaluated numerically. The quantitative information may be used to generate values of localized in vivo NMR parameters such as the spin density, the spin-spin relaxation time, T2, and the spin-lattice relaxation time, T1. The NMR spectroscopy literature is full of suggestions on how best to determine these parameters, particularly T1, in conventional samples studied by physicists and chemists [Gr83, Ha81]. Similarly, the NMR imaging literature offers a multitude of suggestions for in vivo T1 determination, based on both empirical and theoretical arguments [Py83]. The goal of this work was to evaluate empirically the advice found in the NMR spectroscopy literature as to how well it applied to NMR imaging, with its unique experimental constraints.

The pulse programming capabilities of commercial NMR imagers are typically limited, yet there are no fewer than four distinct pulse sequences available which may be used to

provide estimates of the actual in vivo T1: the spin echo (SE) sequence [Ha50], the progressive saturation (PS) sequence [Fr71], the inversion recovery (IR) sequence [Vo68], and the fast inversion recovery (FIR) sequence [Ko77]. Each of these sequences has at least two timing parameters, values of which need to be optimized so as to reduce the overall error in the determined T1 value. In addition, a rational choice of the number of images to be generated, the spacing of the variable timing parameters, and the form of the fitting function must be made with consideration towards the resultant precision and accuracy in measurement, and the net imaging time required. Precision is used in this work to mean the degree of exactness with which a quantity is stated, while accuracy is used to indicate the conformity of an indicated value to an accepted standard value [Va76]. A precise T1 estimate is not necessarily accurate, whereas it is hoped that all accurate T1 estimates are precise. Furthermore, other constraints of the system must be incorporated into the decision process, namely the spatially inhomogeneous rf field, which is the result of rf coil design and the rf attenuating properties of the object [Bo78].

In the present study, experiments were conducted on a phantom consisting of an array of vials containing paramagnetically doped water, whose T1 values spanned the range of clinical concern. Each previously mentioned parameter was systematically varied, and single slice images

of the phantom were generated while the phantom was first immersed in air, and second, in a saline solution of physiological concentration. The effect of the saline solution was to dissipate the rf energy in a similar fashion to the human body, resulting in a spatially inhomogeneous rf field. The raw data were computer processed, resulting in a large population of reduced data, upon which correlative studies were performed.

This investigation produced two principal conclusions. The primary conclusion was, accepting the assumptions given in the methods and materials section concerning the phantom material, that to obtain a direct estimate of the actual T_1 value in an object which may be within a spatially inhomogeneous rf field, the most accurate, precise, and time effective technique to use was three FIR images, with suitably chosen values of the inverting time, T_1 , fitted by a three-parameter exponential function. The use of IR images was equally accurate and precise, but not as temporally efficient. A second conclusion was that the use of three SE images, with suitably chosen values of the pulse sequence repetition time, TR , and fitted by a two-parameter exponential function can be more precise and time effective than the FIR technique in estimating T_1 , but was always much less accurate. These conclusions may be used a priori to design the series of images which will yield the most accurate, precise, and time efficient estimate of an in vivo T_1 value, or they may be used a posteriori to help

evaluate the accuracy of a calculated T1 value from a given series of images. Examples of each type of application are given in the results section.

Methods and Materials

NMR Imaging System

All experiments in this investigation were conducted on a Teslacon whole body NMR imager, manufactured by Technicare Corporation. The main magnetic field was produced by a six-coil, air-core, water-cooled resistive electromagnet. The magnet was nominally operated at 0.15 Tesla, but could be adjusted by altering the current in the electromagnet. The clear bore diameter was one meter, allowing access of an entire human body, with the long axis of the body aligned with the z direction of the main magnetic field.

The imager used separate rf receiver and transmitter coils, allowing separate performance optimization. The transmitter coil was for all intents and purposes a part of the imager, although it was possible to utilize a myriad of rf receiver coils. The manufacturer supplied body rf coil was used for all measurements. This permitted the investigation to be conducted over a large field of view, 0.75 meters, which facilitated the examination of spatially dependent variables.

The rf coil used in NMR is part of a resonant circuit, and it was possible to measure the quality factor, Q, of a circuit containing the body rf coil, on the bench. A sweep wave generator, manufactured by Wavetec, was coupled to the

rf coil. The frequency dependent response was monitored with an oscilloscope, and the Q was determined by

$$Q = f/\delta f$$

[3-1]

where δf was the width of the resonance curve at 70.7% of the amplitude of the response at the resonance frequency, f [Kr81]. The Q was determined with the coil both physically unloaded, and loaded with a dielectric material (0.9% NaCl aqueous solution). The ratio of the unloaded Q to loaded Q was approximately 0.7.

The Teslacon imager made use of a DEC PDP 11/24 computer for pulse sequence programming, data acquisition, and data processing. Additionally, a FPS floating point array processor aided in data processing. All experiments were conducted with the standard software supplied by the manufacturer (software release C), except for modifications implemented which allowed for continuous data acquisition with software controlled incremental timing parameters.

Phantom

The phantom used for all measurements was designed to model certain properties of the human body. Due to the spatial extent of the body it was of interest to examine the possible effects of spatially dependent parameters, such as main magnetic field and rf magnetic field inhomogeneities, upon in vivo spin-lattice relaxation measurements. Hence, the phantom's geometric design, as seen in figure 3-1,



Figure 3-1. Phantom used for all T1 measurements. Inner structure holds eight vials coaxial with the main magnetic field while outer structure could be filled with saline solution.

permitted comparative measurements to be made on identical samples which were spatially distributed within the imager's field of view. The external container could be filled with a saline solution, immersing the phantom.

The range of T_1 values within the body typically spans from 100 milliseconds to 1000 milliseconds, with a few singular exceptions (e.g. cerebral spinal fluid). As given in table 3-1, all experiments were conducted on aqueous solutions of copper sulfate with varying concentrations, spanning a T_1 range of 70 to 1100 milliseconds.

Three assumptions were made concerning this simple phantom material. First, the spin-lattice relaxation decay process was a monotonically decreasing function of time. Second, the exponential decay had a single time constant. Third, the noise spectrum was white, Gaussian, and had a zero mean. The third assumption has been verified for the NMR imager over a wide range of experimental conditions [Sa84].

The actual, or "gold standard" value of T_1 for each of the phantom materials was determined in the following manner: a single cylindrical glass vial (with a diameter of 1.0 centimeters and a length of 10.0 centimeters) containing the doped water solution under analysis, was placed at the position of maximum sensitivity of the rf transmission coil, and coaxial to the main magnetic field. Owing to the small filling factor resulting from the relatively small sample volume, the receiver gain was

Table 3-1

Concentration of Copper Sulfate Doped Water and
Resultant Spin-Lattice Relaxation Time for Phantom Material

<u>Material</u>	<u>Concentration (mM)</u>	<u>T1 (msec)</u>
B(Key 1)	5.0	73.2±14.3
C(Key 2)	3.5	154.0±13.8
D(Key 3)	2.0	277.8±23.1
E(Key 4)	1.0	540.4±57.1
F(Key 5)	0.5	1102.2±109.9

adjusted to make optimum use of the dynamic range of the analog-to-digital converters. The imager was set up to acquire an IR image, with the pulse sequence repetition time, TR, set to 10 times the expected T1 value so as to avoid saturating the signal. All magnetic field gradients, required for spatial encoding of the NMR signal, were turned off. This resulted in the imager being used as a conventional spectrometer. The inverting time, TI, was incrementally varied for over twenty values which spanned the estimated T1 value. For each value of TI, the Fourier transform of the time domain signal was observed, and ten values of maximum amplitude and mean noise were recorded. The arithmetic means of these values were fitted with a three-parameter exponential function using the data reduction routine of the program "NMR", resident on a Nicolet 1180E computer [Nm82]. This procedure was repeated for each different doped solution on two occasions, separated by over a year, with the results given in table 3-1.

In addition to effecting the Q of the rf coil, a dielectric substance will also dissipate incident rf energy. An otherwise spatially homogeneous rf field will become spatially inhomogeneous if a dielectric fills the space. Hence, the mere presence of the body in the NMR imager may alter the homogeneity of the transmitted rf field. The macroscopic implication of this effect was a variation in pulse tip angle from point to point within the body. For

example, for a given transmitted rf pulse, a region close to the surface of the body might experience a 180 degree tip angle, while an interior region, owing to rf attenuation by the tissue, might experience a 170 degree tip angle. Since T_1 measurement accuracy is often sensitive to misset tip angles, the problem of a spatially inhomogeneous rf field was studied as part of this investigation. Figure 3-1 shows the phantom holder positioned within a large cylindrical bottle. All experiments were conducted on the phantom within the empty bottle, and also within the bottle while full of saline solution of physiological concentration (0.9% NaCl). The dimensions of the bottle approximated those of a human abdomen.

Spatial Mapping of Intrinsic Inhomogeneities

T_1 is a calculated value, determined from intensity measurements. Therefore any source of intensity variation might introduce errors into T_1 calculations. Two common sources were main magnetic field inhomogeneity and rf field inhomogeneity. Before attempting any experiments, the intensity of the main magnetic field and rf transmitted field were spatially mapped utilizing the specially constructed field mapper depicted in Figure 3-2. The results are presented in Figures 3-3 and 3-4 respectively.

Since all images were single slice, it was sufficient to examine the z equal zero plane for main magnetic field and/or rf transmitted field inhomogeneities. A 56 centimeter diameter circular piece of lucite with thirty-seven small

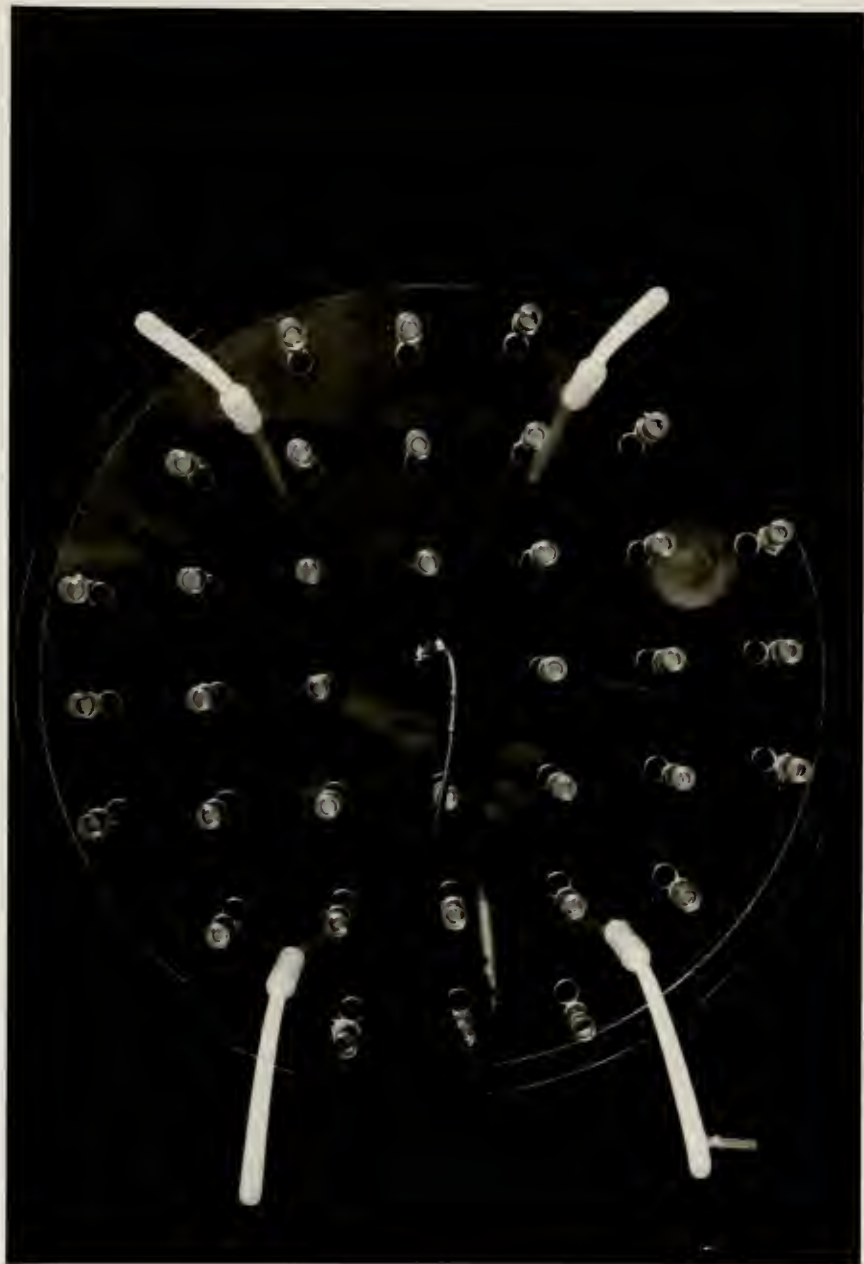


Figure 3-2. Field mapping apparatus. Multiple point source phantom with specially designed rf receiver coil shown at center. Designed for measurements in the transverse plane over a 56 centimeter diameter circular region.

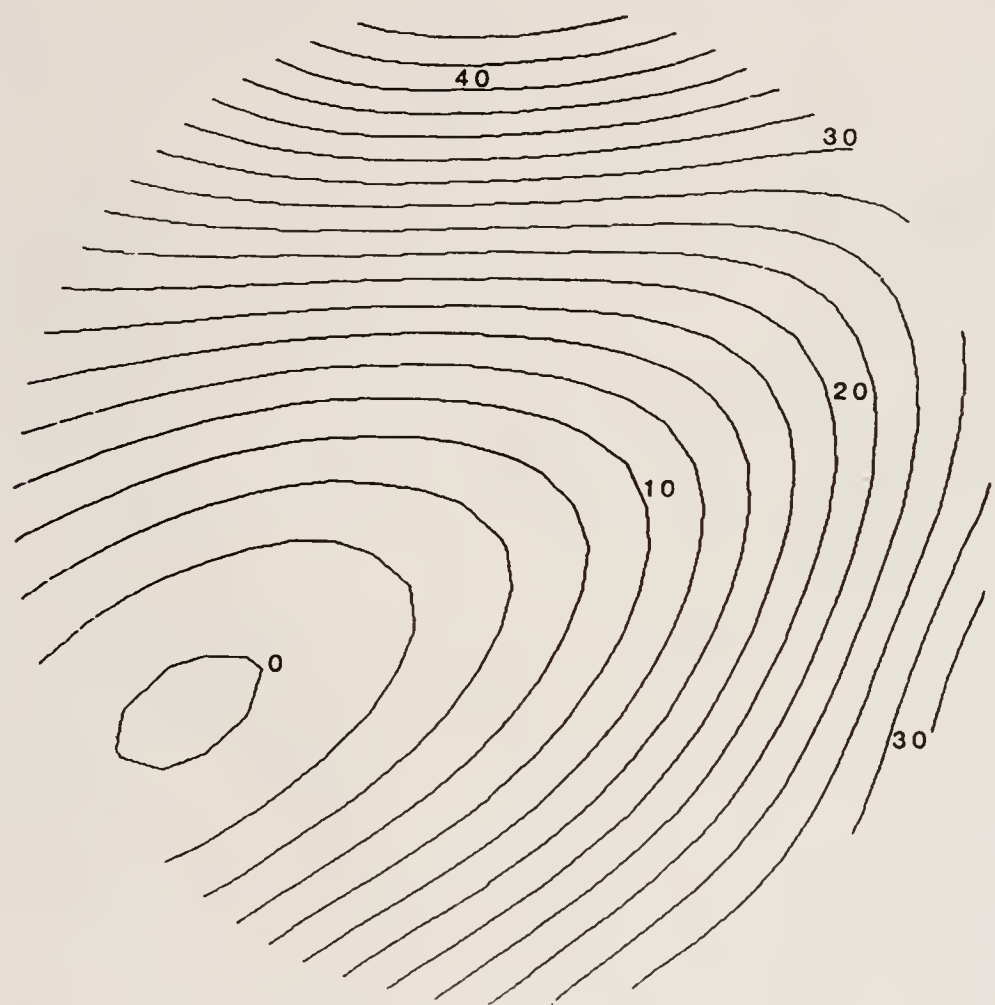


Figure 3-3. Spatial homogeneity mapping of the main magnetic field. Each isostrength curve is 2.5 ppm of the main magnetic field. Measurements were made in the transverse plane over a 56 centimeter diameter circular region.

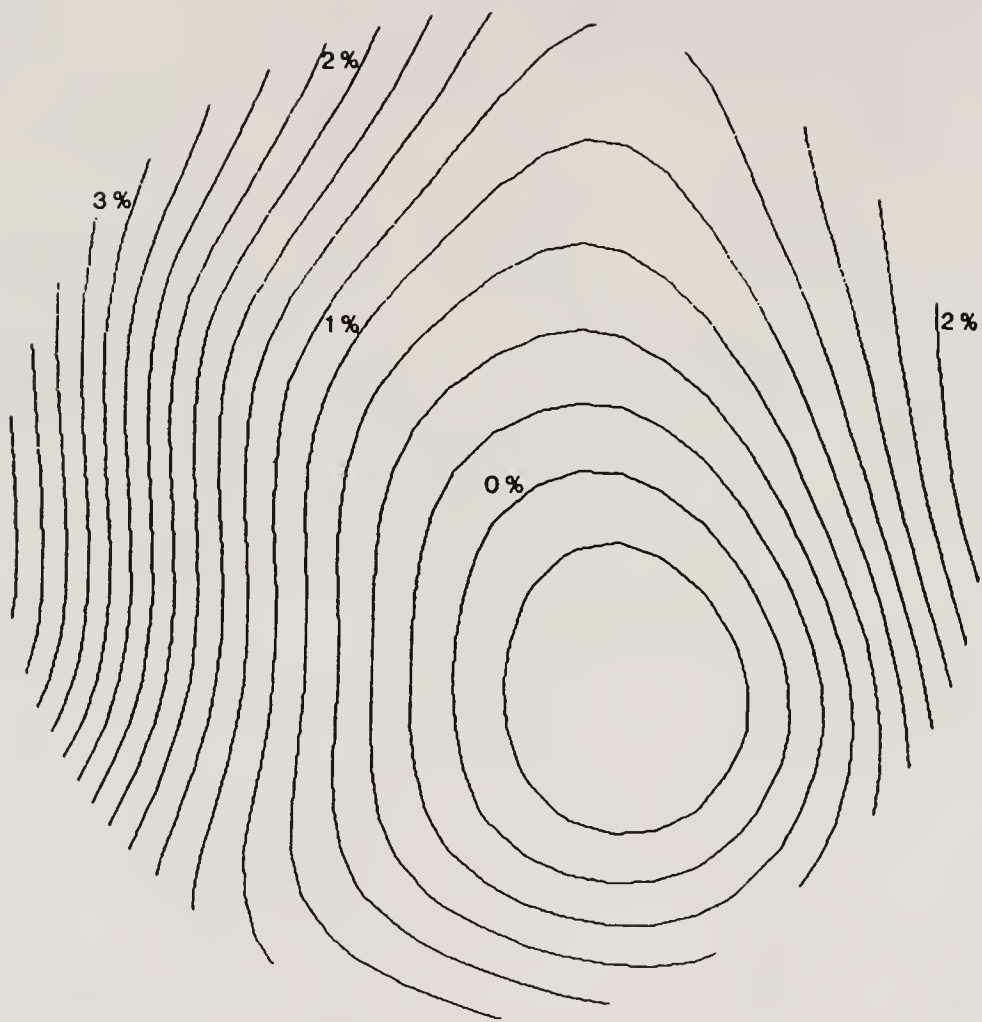


Figure 3-4. Spatial homogeneity mapping of the transmitted rf field. Each isostrength curve is approximately 0.25% of the field at the central region. Measurements were made in the transverse plane over a 56 centimeter diameter circular region.

vials of doped water embedded within it was placed in the z equal zero plane. A one centimeter diameter rf receiver coil was constructed , as seen in figure 3-2, which could be placed in turn over each small vial. The imager was operated as a spectrometer, with the only detectable source of signal being the vial over which the special rf coil was situated, resulting in essentially point source measurements.

To evaluate the main field inhomogeneity, the coil was placed on the center vial, and the main magnetic field was adjusted to insure resonance. The coil was then moved systematically from vial to vial while the registered deviation from the resonance frequency was recorded. Since no imaging gradients were in use, there was a one-to-one correlation between resonance offset and main field inhomogeneity. Over the useful field of view, a coaxial circle of thirty centimeters in diameter, the main magnetic field was homogeneous to approximately 25 parts per million of the main field. This value was within the manufacturer's specifications and was deemed experimentally acceptable.

Although this investigation considered the effects of a spatially inhomogeneous rf field, it was concerned primarily with spatial variations resulting from rf attenuation by the object, and not intrinsic, and therefore constant inhomogeneities of the transmitted rf field. This intrinsic variation was determined, for documentation purposes, in the following manner.

The special rf coil was systematically moved from vial to vial, and while on each vial the main magnetic field would be slightly altered so as to insure resonance. This was accomplished simply by altering the current in the electromagnet. With the resonance condition holding, numerous intensity measurements were recorded and later averaged. This procedure was repeated for each vial. After all intensity values had been recorded, the averaged intensities were compared to determine the transmitted rf homogeneity. If each identical point source sample experienced the same tip angle, then all intensity values should have been equal on resonance. Any variation in intensity was attributed to variation in tip angle. Over the useful field of view, a coaxial circle about thirty centimeters in diameter, the transmitted rf field varied by approximately 3.0%.

Data Acquisition Methodology

The investigation was aimed at determining the most efficient and accurate method of obtaining actual T1 values from NMR images, with consideration towards the constraints a spatially inhomogeneous rf field imposes. Nonuniform rf irradiation was a concern for it results in a spatially dependent systematic error in rf pulse tip angles, and hence in measured T1 [Fr71]. Evaluation of four pulse sequences was conducted, the spin echo (SE), the inversion recovery (IR), the progressive saturation (PS), and the fast inversion recovery (FIR). The degree of freedom of the

fitting function dictated the lower bound on the number of images required for a unique determination of the T1 value, while the upper bound was investigated as to its dependence upon pulse sequence utilized, desired accuracy in measurement, and net imaging time. Similarly, the spacing of the variable timing parameter was evaluated as a function of the measurement accuracy and net imaging time for a given pulse sequence.

For all experiments, a nonlinear least squares fitting algorithm was used, of the form

$$S(TP) = K - C[\exp(-TP/T1)] \quad [3-2]$$

where K and C were constants and S(TP) was the signal intensity as a function of a timing parameter, TP.

In PS and SE images, T1 weighting was introduced by saturating the signal with rapid pulsing. Therefore, TP was the pulse sequence repetition time, TR. The spectroscopy literature [Fr71] suggests using a fitting function with two degrees of freedom, given by setting C in equation 3-2 equal to K, to determine T1 from either PS or SE images.

T1 information was incorporated into IR images by inverting the equilibrium magnetization, allowing some time to pass during which spin-lattice relaxation occurred, and sampling the remaining magnetization by bringing it into the transverse plane where detection took place. For IR images, TP was equal to the inverting time, TI. The NMR spectroscopy

literature [Vo68] suggests using a fitting function with two degrees of freedom, given by setting C in equation 3-2 equal to $2K$, for IR images where the inverting pulse was exactly 180 degrees. When the inverting pulse was misset, possibly due to a spatially inhomogeneous rf field, the literature [Ko77] suggests the use of a fitting function with three degrees of freedom, such as equation 3-2.

The FIR images were identical to the IR images, except that a rapid IR was used, with one result being a reduction of the total image time. Typically, TR for IR images was five times T_1 or longer, while in FIR images TR was commonly two to three times T_1 . As suggested in the literature [Ca75], this rapid IR requires the use of a fitting function with three degrees of freedom, such as equation 3-2, whether the inverting pulse was misset or not.

Details of the exact experimental procedure follow. It should be noted that the specified method was performed for each of the five phantom samples as given in table 3-1, both surrounded by air and surrounded by the dielectric saline solution. This permitted the analysis to span the entire clinically useful T_1 range, and also to evaluate the effects of misset rf pulse tip angles resulting from an inhomogeneous rf field. All acquired images were single slice, at the z equal zero plane, with slice thickness of one centimeter. The Teslacon imager typically gathered 256 data points in the readout direction and 128 data points in the phase encoding direction. The displayed image was 512

pixels by 512 pixels which was derived from the stored image data which was dimensioned 256 by 256. Hence the data in the phase encoding direction were interpolated. To avoid the use of interpolated data, the data acquisition routine was modified to permit the use of 256 phase encoding gradient steps. In all experiments the echo time, TE, was maintained at its shortest value, 30 milliseconds, to minimize contributions from spin-spin relaxation and molecular self-diffusion. Two averages were taken for each image.

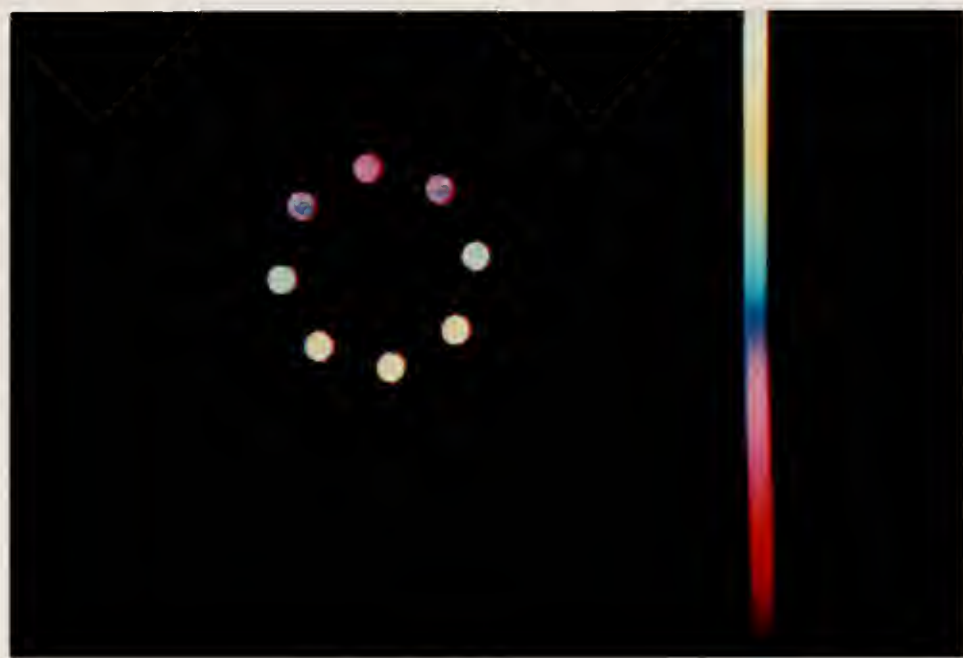
The PS and SE experiments differed in only two respects. First, the PS images relied upon the bulk magnetization's reaching a steady-state value in the presence of the rapid pulsing with $\pi/2$ rf pulses. It is suggested that the system reaches this steady-state within four pulses [Fr71], hence all PS images were preceded by four pulses prior to image acquisition. Second, PS experiments yield consistent values of T1 for TR in the range of 0.5T1 to 2.0T1, whereas SE experiments yield consistent values of T1 for TR in the range of 0.5T1 to 3.0T1. Hence, images were collected with TR ranging from its minimum value, dictated by the manufacturer to be 50ms, to a maximum of three times the actual T1. Additionally, a TR value of 5.0T1 was used to sample the unsaturated initial magnetization. In total, no less than twenty images were acquired with varying TR values. In data processing images with TR less than or equal to 1.5T1 were considered PS images, and those with TR greater than 1.5T1 were SE images.

The IR and FIR experiments, as acquired with the imager, differed in only two respects. First, the IR images were acquired assuming that the bulk magnetization was at its initial equilibrium value prior to the commencement of the pulse sequence. Therefore, TR for all IR images was set to at least five times the actual T1 value. This condition was not required for FIR images, hence the origin of "fast" in fast inversion recovery, with TR nominally set to twice the actual T1 value in the FIR images. Second, since the maximum value of TI must be less than TR, the range of TI for IR images was from its minimum value, dictated by the manufacturer to be 25 milliseconds, to just less than 5.0T1. In the FIR images, TI ranged from 25 milliseconds to just less than 2.0T1. In total, no less than ten IR images or ten FIR images were acquired with varying TI values.

Data Processing Methodology

All images acquired with the Teslacon system were displayed on a high resolution monochromatic CRT monitor, with a maximum of 1024 gray levels. It was also possible to display the images on a high resolution color monitor, as shown in figure 3-5. Each image was reconstructed, and the spatially dependent signal intensities were displayed on the CRT monitor for analysis. Reconstruction of the PS and SE images differed from that of the IR and FIR images.

The imager acquired all raw data using quadrature detection, effectively resulting in each data point's being defined by a complex number. PS and SE experiments sampled



a



b

Figure 3-5. Color NMR images of phantom. (a) With eight identical vials, (b) with all vials surrounded by saline solution.

the magnetization, whose value lay between zero and its equilibrium value. Since this is a one sided range, all positive in sign, signal intensities in PS and SE images were represented by the magnitude of the corresponding complex number. IR and FIR experiments sampled the magnetization while it was in the range of plus or minus its equilibrium value. To retain the signed information, signal intensities in IR and FIR images were determined and represented taking into account the phase of the corresponding complex number.

While in the display mode, quantitative information was obtained from the image. Signal intensity information was gathered by positioning a software controlled region of interest, ROI, about the spatial area of concern. The system made available the number of pixels enclosed in the ROI, the mean intensity value of those pixels, and the corresponding standard deviation. For all images taken with the phantom designed for this investigation, no fewer than one hundred pixels were used to define each vial. The intensity information from all eight vials in the field of view, and also the intensity information from a representative region of background noise, were determined and recorded. These measurements formed the raw data base on which all subsequent analysis was conducted.

A Fortran program, which performed a nonlinear least squares fit without the need for initial guesses of the fitted values, was written and implemented on a IBM 470

computer system. The general purpose of this program was to determine the optimal number of images, and the values of their associated timing parameters, required to accurately and precisely determine T_1 for a given pulse sequence. The details of how this was accomplished follow.

The program accepted as input the type of pulse sequence and the signal intensities as a function of the corresponding timing parameter. This information was given for each vial, for each different concentration of solution, and for both immersion in air and immersion in saline solution. In NMR spectroscopy, where the sample under investigation may be examined for any given period of time, typically ten to thirty data pairs are used in fitting the empirical data to the theoretically expected function, resulting in an estimate of T_1 . In NMR imaging, the time constraint is more restrictive. Ill patients cannot remain in the imager for an extended period of time, and the physician is usually not willing to spend an inordinate amount of time on a single procedure.

This study aimed to determine whether the acquisition of two, three, or four images resulted in the most accurate and precise T_1 estimate. If each data set contained, say, ten data pairs, the analysis program considered each possible combination of two data pairs at a time, three at a time, and four at a time. These two, three, or four data pairs were then fitted to the appropriate functional form of equation 3-2 for the given pulse sequence.

If a function with three degrees of freedom was required, then only the combinations involving three and four data pairs were used. For example, an IR data set, consisting of ten data pairs and fitted to both a function with two degrees of freedom and a function with three degrees of freedom, generated seven hundred and five fitted values of T_1 . Multiplying this by the eight vials, the five different concentration samples, and the possible immersion in air or saline resulted in over five thousand estimated T_1 values. These estimated values were compared to the actual T_1 value, and also to the estimated T_1 value obtained if all of the data pairs, for example ten, were fitted to equation 3-2. Comparison with the actual T_1 tested for precision and accuracy, while comparison with the estimated T_1 tested simply for precision. It required over five minutes of CPU time to process all the raw data and transfer in excess of twelve megabytes of reduced data.

Table 3-2 presents some typical raw data which were acquired for T_1 determination. The experiment performed was an inversion recovery experiment, conducted on phantom material C. The IR and TE values were kept constant at 1250msec and 30msec respectively. Data are presented for both the phantom material immersed and not immersed in the saline solution. Column one depicts the values of T_1 used for T_1 determination, chosen to properly span the actual T_1 value of phantom material C of 154msec. The region-of-interest derived signal intensities for vials 1

Table 3-2
Typical Raw Data Acquired for T1 Determination

<u>TI(msec)</u>	<u>SI(vial 1)</u>	<u>SI(vial 5)</u>	<u>Background</u>
<u>PHANTOM NOT IMMERSED IN SALINE SOLUTION</u>			
50	-43.7	-90.4	0.38
75	-7.1	-26.4	0.12
125	44.1	80.1	0.06
175	87.4	173.2	-0.26
225	119.5	229.5	-0.27
275	148.7	273.9	-1.32
325	163.6	326.0	1.15
400	186.2	361.4	-0.07
1000	223.9	430.0	0.05
<u>PHANTOM IMMERSED IN SALINE SOLUTION</u>			
50	16.3	24.0	0.06
75	21.8	36.0	-0.33
125	27.4	48.4	1.40
175	33.7	60.0	1.90
225	38.4	68.9	1.10
275	39.8	78.1	1.40
325	40.2	82.7	-0.74
400	47.8	86.5	-2.40
1000	51.2	95.1	-0.44

Inversion recovery experiments were conducted on phantom material C, with TR=1250msec and TE=30msec, resulting in the stated signal intensities (SI) and background values.

and 5 are presented in columns two and three respectively, in arbitrary units. Vial 1 was in a region of minimum receiver coil sensitivity, while vial 5 was in a region of higher sensitivity. Column four contains the background noise intensity values. Two points of interest are noted. One, the magnitude of all signal intensities of vial 5 are greater than the corresponding values for vial 1. This is a direct result of the receiver coil sensitivity. Second, the signal intensities for the phantom immersed in the saline solution vary dramatically from those signal intensities for the phantom not immersed in the saline solution. A possible explanation is that the saline solution absorbs a portion of the transmitted rf power, thus resulting in misset tip angles at the vials' positions.

Figures 3-6 and 3-7 present examples of fitted curves to typical data which were acquired for T_1 determination. Figure 3-6a illustrates the fitting of ten inversion recovery data sets by a three-parameter exponential function. The estimated T_1 value was 132 ± 8 msec, which happens to be within 15% of the actual T_1 value of 154 msec. In the subsequent analysis of this data, only groups of three data sets and groups of four data sets will be used to determine T_1 . Each T_1 value determined in this manner will be compared to both the natural T_1 value of 154 msec, and also the estimated T_1 value of 132 msec.

Figure 3-6b illustrates the fitting of only three out of the possible ten data sets to a three-parameter

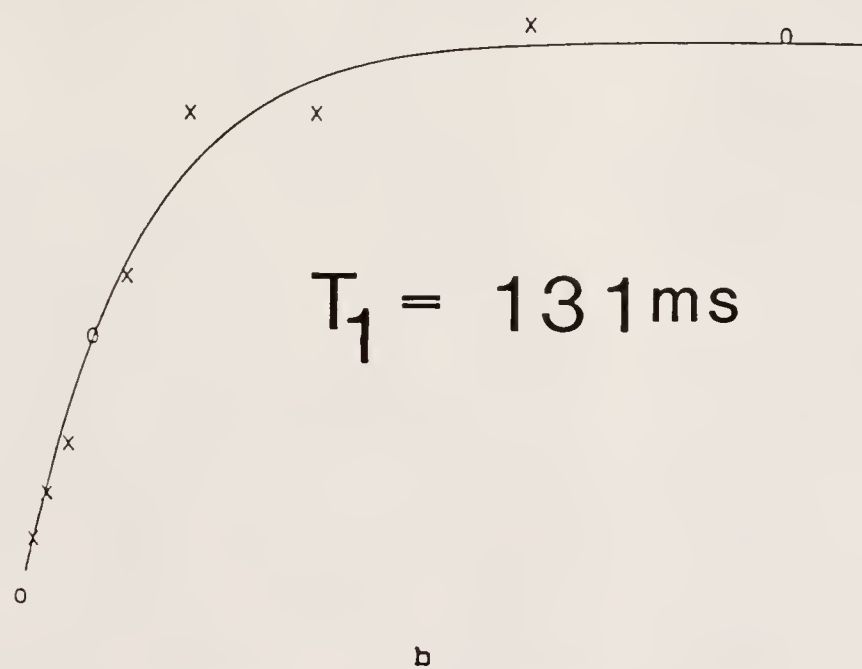
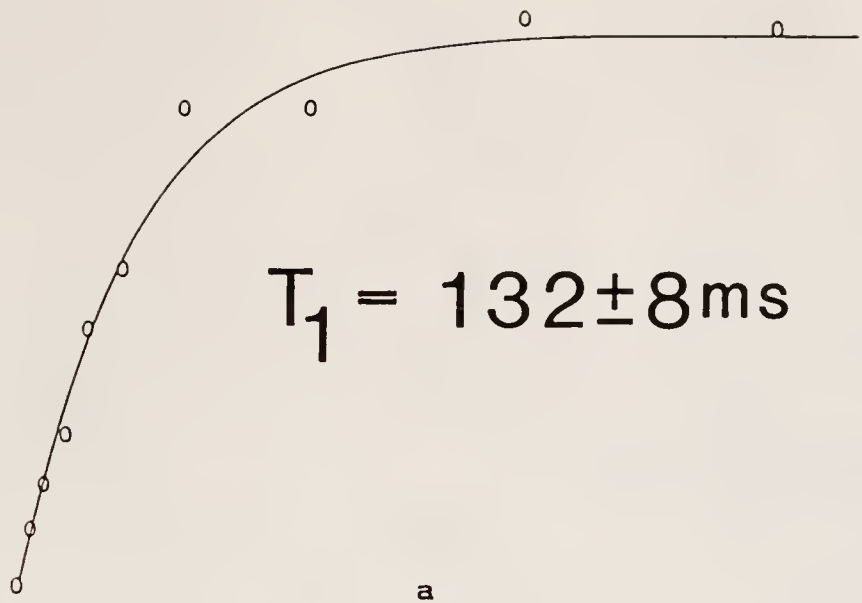


Figure 3-6. Examples of fitted data sets yielding good T_1 estimates. Curve (a) was generated by fitting all points while (b) was generated by fitting only the points denoted by "0".

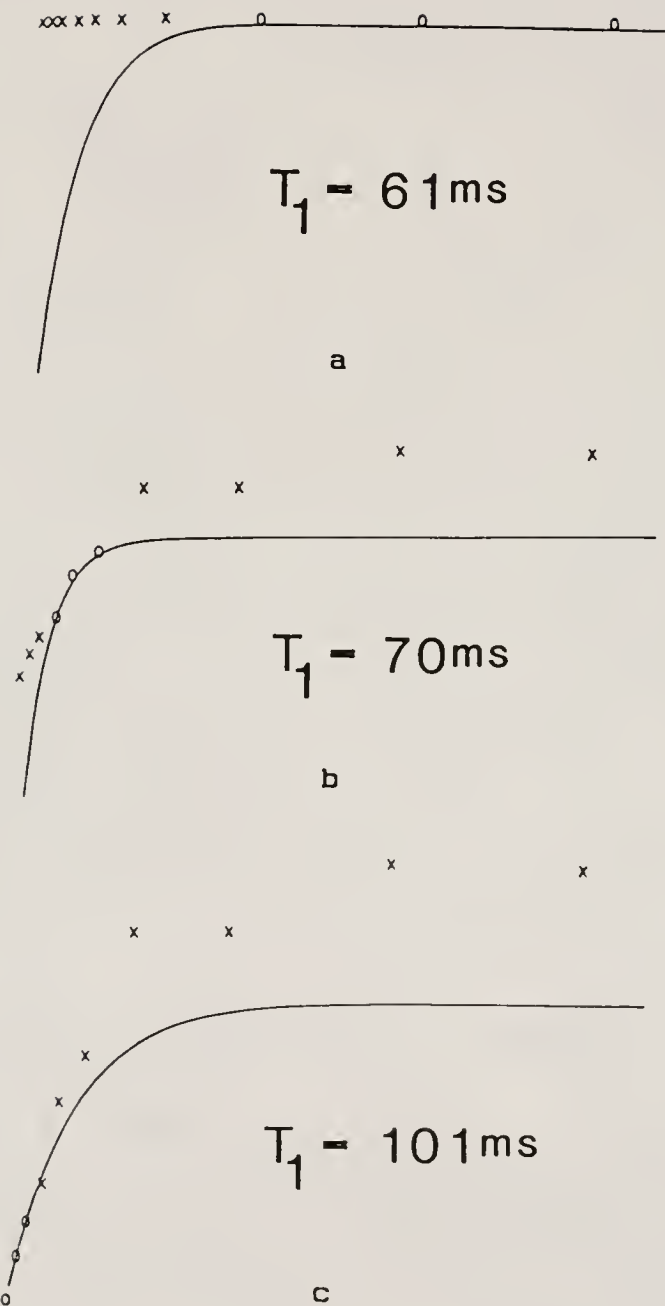


Figure 3-7. Examples of fitted data sets which yielded poor T_1 estimates. Curves (a), (b), and (c) were fitted only to the data points denoted as "0".

exponential function. The three data points used for fitting are denoted as "0", while the unused data points are presented as "X". For this particular choice of three data points, the estimated T_1 value is 131 msec. Thus, this particular value is both within 15% of the all points estimated T_1 value of 132 msec, and also within 15% of the natural T_1 value of 154 msec. Figure 3-7 presents three other possible choices of three data sets, fitted by a three-parameter exponential function. In each case, the estimated T_1 value is neither within 15% of the all points estimated T_1 value nor the natural T_1 value. These particular choices of three data sets would be deemed poor. The different grouping of the data points in figure 3-7a, b, and c, is an artifact of the curve fitting program, done so that the full fitted curve might be displayed.

The good choice of three data sets of figure 3-6b, and the bad choices of figure 3-7 illustrate certain basic characteristics. The good choice of figure 3-6b depicts three T_1 values which span the entire relaxation curve. One point defines the signal intensity at, essentially, time equal zero. Another T_1 value results in a signal intensity corresponding to almost the completely relaxed state. Finally the third T_1 value comes just about at the time the relaxation curve changes the most. Of course, these are not the only choices of T_1 values which resulted in good fits, indeed, there were many. One of the purposes of this investigation was to identify and quantify how much

variation could be tolerated from the near ideal distribution of T1 values as depicted in figure 3-6b. Obviously, the variations illustrated in figure 3-7 could not be tolerated. In each case the three T1 values were grouped very near each other, and therefore were unable to characterize the entire relaxation curve, rather, they only characterized the small region of the curve where they were located.

Data Analysis Methodology

To facilitate analysis of the numerical data, a program was developed on an APPLE 2-plus microcomputer, which down-loaded the processed data from the IBM 3330 disk pack, and permitted graphical display of correlated parameters. An example of one such output is given in figure 3-8. The graphical presentation of correlated data allowed for rapid qualitative data analysis. By this method, conclusions concerning positional dependence, dependence on the actual T1 value, optimal number of images required, variation in accuracy and/or precision in estimated T1 value as a function of phantom immersion in either air or saline solution, choice of fitting function, and relative merit of each pulse sequence were efficiently and accurately determined.

The criterion used in all evaluations was as follows: for a given set of parameters (e.g. FIR experiment, actual T1 of 277.8 milliseconds, vial number three, phantom immersed in saline solution, using three images, and fitted

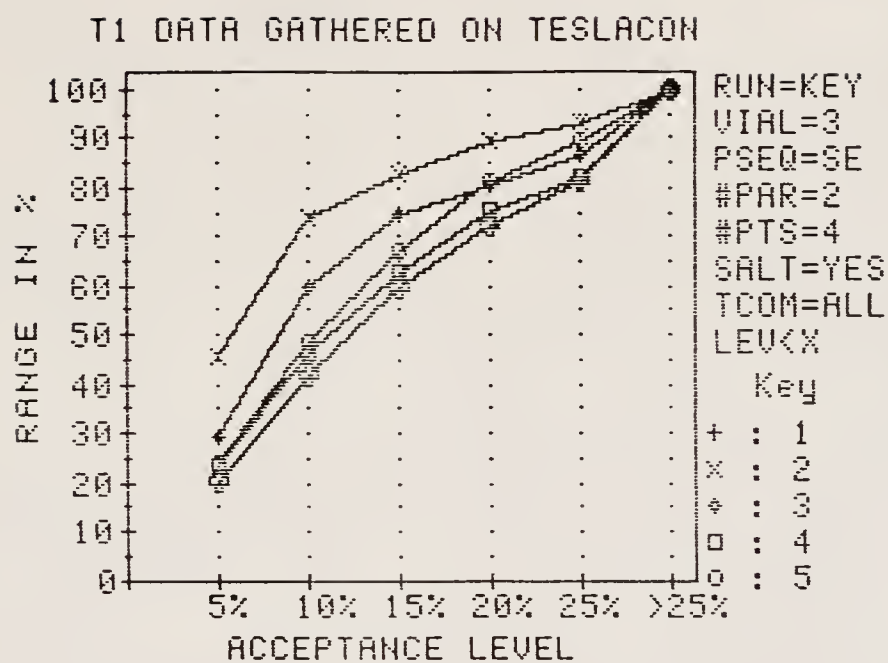


Figure 3-8. Sample computer output of data correlation program.

by a function with three degrees of freedom), the criterion was that the estimated T1 value fitted with less than a 15% relative error to either the actual T1 value or the T1 estimate obtained by fitting all the data pairs. In comparing different sets of parameters, what was actually compared was the percentage of all possible permuted data pairs which met this criterion. This percentage was denoted as "range in %" in figure 3-8.

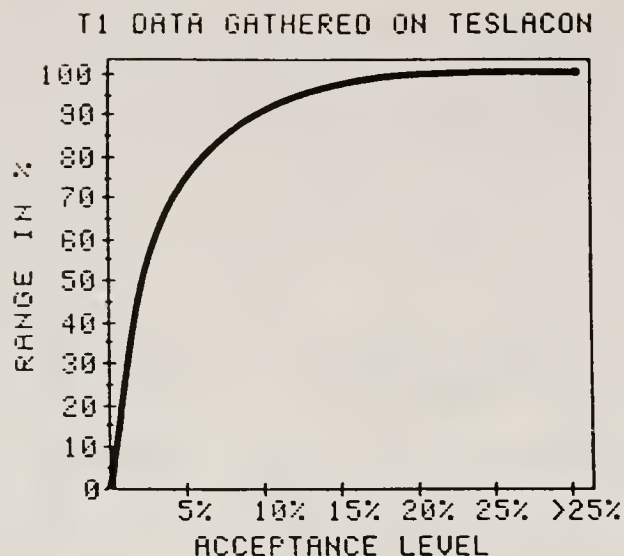
The other features of figure 3-8 are as follow. The parameter "RUN" refers to which phantom material was used in the particular run illustrated. The phrase "RUN=KEY" implies that the plot is an overlay plot of many runs, and that one is referred to the "Key" which indicates which plotting character corresponds to which phantom material. The "Key" indicates that the results of five different phantom materials are presented on this single plot. "RUN" 1 through 5 corresponds to phantom material B through F.

The parameter "VIAL" indicates from which of the eight possible vials the data came from. Similarly, "PSEQ" indicates which pulse sequence was used for the T1 estimate (i.e. PS, SE, IR, FIR). "#PAR" refers to the number of parameters in the fitting function used for T1 determination, either two or three. "#PIS" refers to the number of data points fitted to determine T1. "#PIS" was either two, three, or four for "#PAR" equal to two, or "#PIS" was three or four for "#PAR" equal to three. The parameter "SALT" indicates if the phantom was immersed in

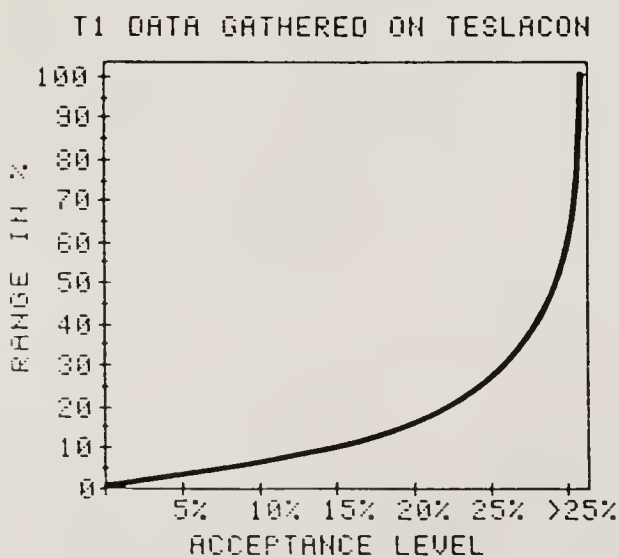
the saline solution ("SALT=YES"), or if the phantom was not immersed in the saline solution ("SALT=NO"). The parameter "ICOM" indicates what the estimated T1 was compared to, either the all points estimated T1 ("ICOM=ALL"), or the natural T1 ("ICOM=GLD"). Finally, "LEV<X" indicates that the acceptance levels are given on the x axis.

Figure 3-9 is an aid which illustrates how to interpret the graphical displays of correlated parameters. Figure 3-9a illustrates a favorable situation. This figure illustrates that approximately 50% of all experiments resulted in an estimated T1 value within 5% of the standard value. Indeed, over 95% of all experiments were within 15% of the standard. If this hypothetical curve corresponded to an inversion recovery experiment, then it could be interpreted as follows. Although many different sets of T1 values were considered, the T1 value which was estimated appeared to remain relatively constant. Thus, it would not be very crucial in practice to optimize the choice of the T1 values used to gather data for T1 determination, for so many different combinations were equally able to generate an accurate and precise estimate.

Figure 3-9b illustrates a poor situation. In this figure, less than 5% of all experiments would result in an estimated T1 value which was within 5% of the standard. Indeed, it appears that less than 30% of all experiments would result in estimated T1 values within 25% of the standard. If this hypothetical curve corresponded to real



a



b

Figure 3-9. Hypothetical output of data correlation program. Output (a) depicts a nearly ideal output, while (b) depicts a poor output.

data it would indicate that just a very few choices of the timing parameters would result in an acceptable T_1 estimate. Typically, most of the actual curves fell between the two hypothetical curves of figure 3-9.

Typically, natural biological variation will far exceed any machine error, hence total measurement errors within 10% for in vitro experiments are not uncommon [Be84].

Indeed, total measurement errors could exceed 10% for in vivo experiments, where the investigator has less control over certain biological variables. Although certain combinations of parameters resulted in estimated T_1 values of high precision (the estimated value had much less than a 15% relative error), acceptance at the 15% relative error level was chosen to coincide with typical in vivo biological variability.

After the qualitative data analysis based upon the graphical display of correlated parameters was completed, a more detailed quantitative analysis was conducted in order to determine those values of the variable timing parameter which permitted the most accurate and precise estimate of T_1 to be made. A description of the analysis method follows.

First, for a given set of experimental parameters (i.e. pulse sequence, phantom solution concentration, immersion in air or saline, particular vial, number of images used for fit, and the form of the fitting function), the values of the variable timing parameter which resulted in a fit with less than 15% relative error were noted. By way of

illustration, if one of the fixed parameters was the use of three images, then the analysis culminated in a set of, for example, one hundred groups of three numbers. Each group of three numbers was actually three values of the variable timing parameter (TR for PS and SE images, TI for IR and FIR images) which resulted in a good fit. Each value was then scaled to the TI value which the fit was being compared to. Next, a linear-multiple-regression analysis [Sp61] was performed on this set of groups, yielding a regression equation which related the three values of the variable timing parameters to each other. This is the multidimensional analog to the least-squares fit line used for two dimensional data sets. Hence, for three images, a least squares fit plane was determined which incorporated the empirical data into an analytical expression. This analytical expression could be used a priori in selecting values of the variable timing parameter, or a posteriori in evaluating the group of timing parameters used in a series of images.

Results

There were five basic results of this investigation, two of which are of primary importance. Some of the results were of a general nature, such as the dependence of measurement upon the position within the field of view, and the variation in the accuracy and precision in the estimated TI value as a function of the actual TI value. Other results were more specific, such as the determination of how many

images acquired with which pulse sequence, and fitted by which function, resulted in accurate and precise estimated T1 values, independent of the presence of the rf attenuating saline solution. Finally, particular results were quantitative, for example, the linear multiple regression analysis of the values of the variable timing parameter which resulted in accurate and precise T1 estimates.

The performance of the PS experiment was so poor in contrast to the SE, IR, and FIR experiments, for the reasons offered in the discussion section of this chapter, that it was discounted as a viable method of T1 determination. The following results apply only to SE, IR, and FIR experiments. Representative data are presented in support of all results. The reproducibility of signal intensities for a given set of parameters was at all times greater than 95%, and typically greater than 97.5%. The reproducibility was determined from a series of measurements which were all repeated ten times.

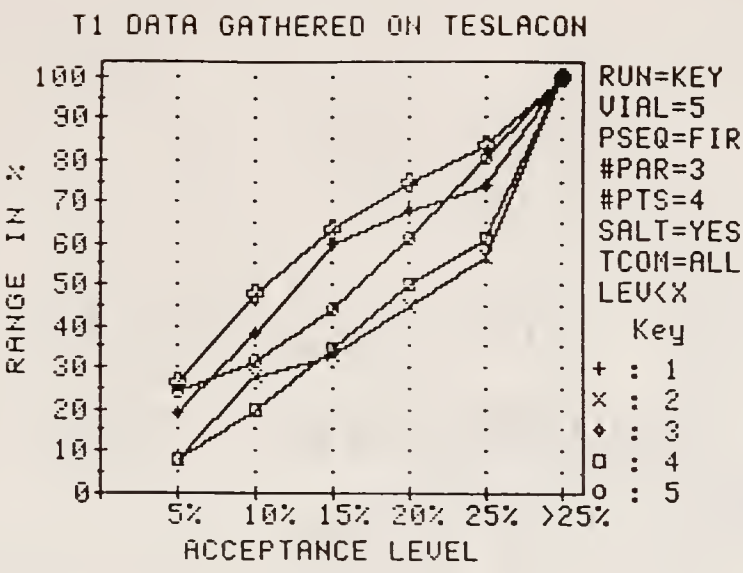
Positional Dependence

All estimated T1 values were constant within 15% to the position within the field of view from which the individual signal intensities were recorded. That is, although spatial variations in signal intensity occurred, calculated values of T1 did not exhibit these variations, within acceptable experimental limits. The signal intensity variations resulted from the intrinsic magnetic field inhomogeneity, the intrinsic transmitted rf field inhomogeneity, and mostly, the spatially inhomogeneous rf receiver coil response.

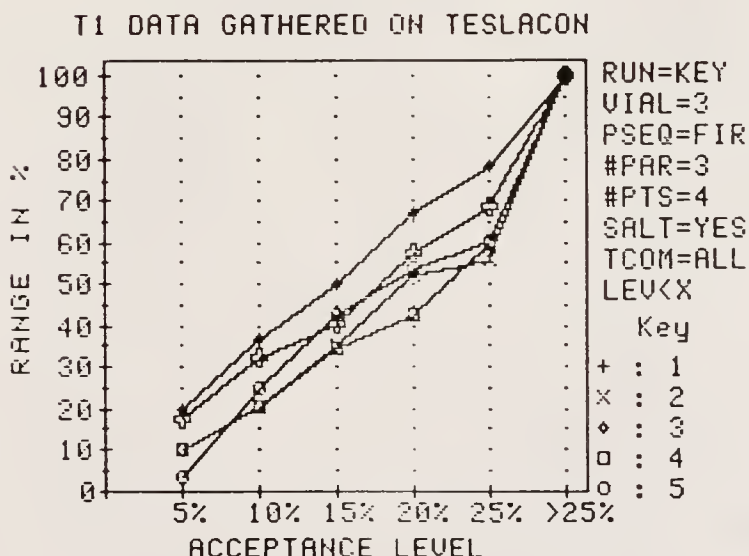
The representative data of Figure 3-10 support this result. Vial three was positioned at the site of maximum receiver sensitivity, while vial five was located at a position of poor sensitivity. A comparable percentage of experiments met the acceptance criterion (fitted T1 value had less than a 15% relative error) for both vials. Although similar estimated T1 values were calculated for both vials, typically the standard deviations in the fits for vial five were larger than those for vial three, owing to the smaller signal to noise ratio of the intensities at that position.

Dependence Upon Actual T1 Value

The percentage of experiments which met the acceptance criterion was constant within 15% to the actual T1. That is, a given set of parameters (with the values of the variable timing parameter suitably chosen for the actual T1) generated a similar number of good fitting T1 estimates, independent of the actual T1. Also, for a given set of parameters characterizing experiments which met the acceptance criterion, the values of the variable timing parameter normalized to the actual T1 were constant within 15% to the actual T1. Thus, it was possible to characterize the optimal values of the timing parameter independent of T1. The representative data of Figure 3-11 support this result. Each different "RUN" represents a different actual T1 value of the phantom material. The close grouping of the data along the "RANGE IN %" axis, as a function of "ACCEPTANCE LEVEL", indicates the insensitivity to T1 value.



a



b

Figure 3-10. Representative data indicating independence to position in field-of-view. (a) Vial 5 output, (b) identical output for vial 3.

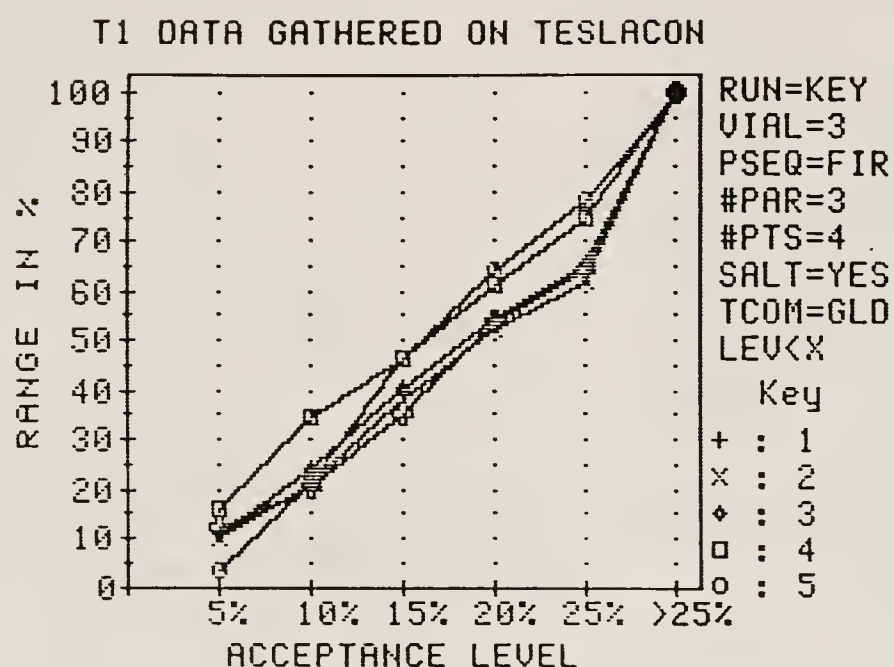


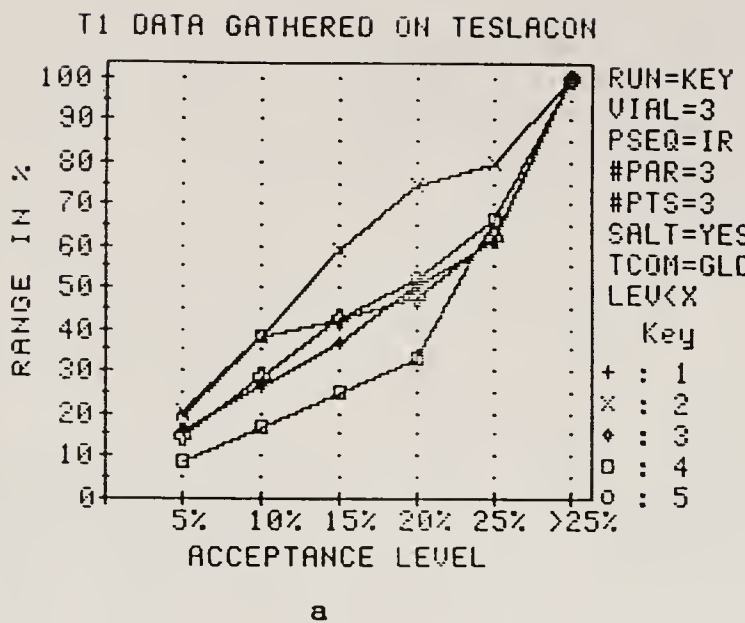
Figure 3-11. Representative data indicating independence to actual T1 value.

Dependence Upon Number of Images

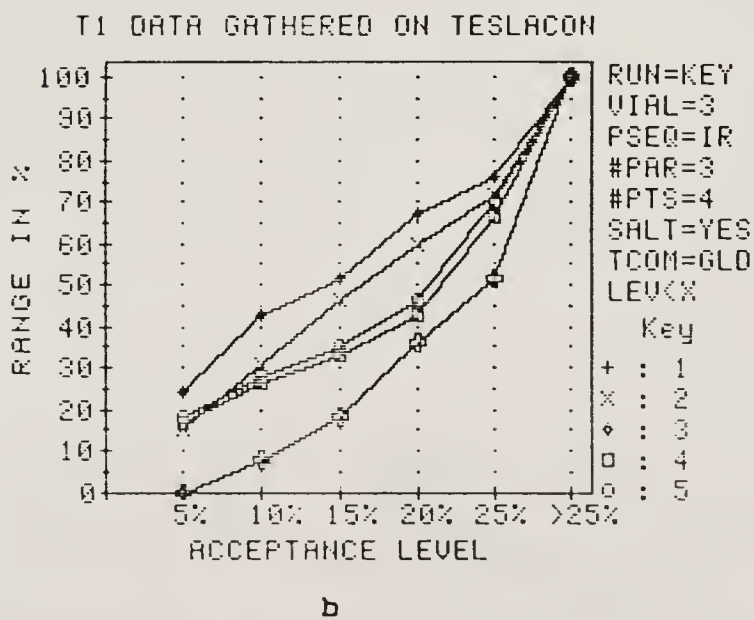
For a given set of parameters, the percentage of experiments which met the acceptance criterion utilizing a two-parameter fitting function was constant within 15% to the acquisition and use of two, three, or four images for T_1 estimation. Similarly, the percentage of experiments which met the acceptance criterion utilizing a three-parameter fitting function was constant within 15% to the acquisition and use of three or four images for T_1 estimation. That is, a given set of parameters, with the degrees of the fitting function constant, generated a similar number of good fitting T_1 estimates, independent of the number of processed images.

There was a corollary result. As explained previously, IR experiments were fitted twice, once by a function with two degrees of freedom (given by setting C in equation 3-2 equal to $2K$), and once by a function with three degrees of freedom (given by equation 3-2). For each form of the function, all IR experiments were constant within 15% to the number of images used, although fitting with the three-parameter function resulted in a substantially higher percentage of experiments which met the acceptance criterion.

The representative data of figure 3-12 support these results. Additionally, the results of fitting FIR experiments with a function with two degrees of freedom are also presented in figure 3-13.



a



b

Figure 3-12. Representative data indicating independence to number of images. (a) Using three images for T1 determination, (b) using four images for T1 determination.

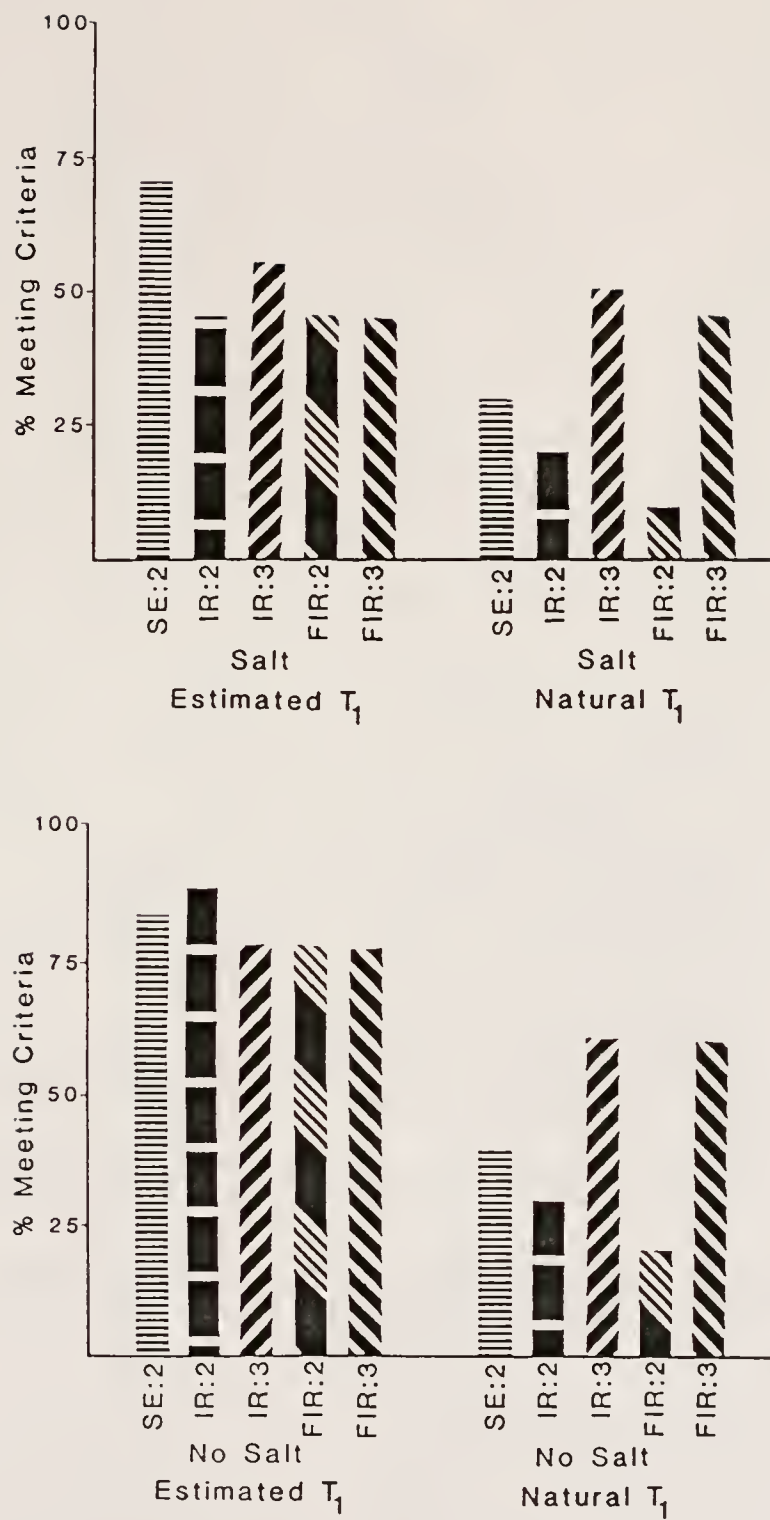


Figure 3-13. Summary of results.

Optimal Sets of Parameters

To obtain a direct estimate of the actual T_1 value in an object which may be within a spatially inhomogeneous rf field, the most accurate, precise, and time effective technique to use was three FIR images, with suitably chosen values of T_1 , fitted by a three-parameter exponential function. The use of IR images was equally accurate and precise, but not as temporally efficient.

Three SE images, with suitably chosen values of T_R , and fitted by a two-parameter exponential function can be more precise and time effective than the FIR technique in estimating T_1 , but were always much less accurate, and prone to error if an inhomogeneous rf field was present. The representative data of figure 3-13 support these results.

Optimum Variable Timing Parameter Values

For each of the three above mentioned optimum sets of parameters, a linear multiple regression analysis was conducted on the empirical values of the variable timing parameters which resulted in estimated T_1 values of 15% relative error or less. For each regression analysis, a coefficient of linear multiple correlation was determined. The coefficient may lie between 0 and 1. The closer it was to 1, the better was the linear relationship between the variables, with a value of 1 indicating a perfect correlation. The closer it was to 0, the worse was the linear relationship. For all cases, the coefficient of linear multiple correlation was 0.5 or greater.

The use of three FIR images, fitted by a three parameter exponential function, was the optimal method of estimating the actual T_1 value, in the presence of a spatially inhomogeneous rf field. The relationship between the three values of T_1 in these FIR experiments was

$$H = 1.1 + 0.6M - 0.1L \quad [3-3]$$

where the three T_1 values, H , M , and L were the highest, middle, and lowest values all scaled to T_1 by dividing the specific timing parameter by the actual T_1 value. The standard error of estimate in H was 0.3, for M it was 0.3, and for L it was 0.2.

The use of three IR images, fitted by a three-parameter exponential function, was another method of estimating the actual T_1 value, in the presence of a spatially inhomogeneous rf field. The relationship between the three values of T_1 in the IR experiments was

$$H = 1.6 + 1.1M + 0.6L \quad [3-4]$$

where the three T_1 values, H , M , and L were the highest, middle, and lowest values normalized to the actual T_1 value. The standard error of estimate in H was 1.2, for M it was 0.4, and for L it was 0.3.

A large percentage of SE experiments did not meet the acceptance criterion when the estimated T_1 value was

compared to the actual T_1 value. However, there was a large percentage of SE experiments which did meet the acceptance criterion when the calculated T_1 value was compared to the value of T_1 estimated by the fitting of all data pairs. This indicated that while estimated T_1 values from SE images were not accurate, they were precise. The relationship between the three values of T_1 for this set of parameters in the SE experiment was

$$H = 1.7 + 1.1M - 0.3L \quad [3-5]$$

where the three values, H , M , and L were the highest, middle, and lowest values normalized, in this case, to the T_1 value estimated by fitting all data pairs. The standard error of estimate in H was 1.1, for M it was 0.7, and for L it was 0.3.

Discussion

The in vivo determination of T_1 values is complicated by many factors, some of which were addressed by this investigation. The specific aim of this investigation was to evaluate empirically the suggestions offered by the NMR spectroscopy literature on T_1 determination and as to how well they applied to NMR imaging, with its unique set of experimental constraints.

The NMR spectroscopy literature offered suggestions on which pulse sequence to use, the number and values of the variable timing parameter to use, and the form of the

fitting function required to calculate T_1 from the individual signal intensity measurements. The added constraints imposed by NMR imaging were the following: measurements could be obtained from any position within a large field of view, typical T_1 values in the human body span a range of over an order of magnitude, total imaging times had to be minimized, and the human body has dielectric properties which resulted in spatially dependent rf attenuation.

Positional Dependence

It was determined that all estimated T_1 values were constant within 15% to the position within the field of view from which the individual signal intensities were recorded. If there were no spatial variation in signal intensity (for fixed experimental parameters), then this would be an expected result. As demonstrated by the signal intensity variations in figure 3-5, this was not the case.

The predominant cause of spatial variations in signal intensity measurements was the spatially inhomogeneous rf receiver coil response. The half saddle shape of the rf receiver coil produced an axially asymmetric spatial response, as seen in figure 3-5. Thus, for a hypothetical sample that filled the field of view and produced a constant, homogeneous signal from each position, the recorded signal intensity would be the constant intensity convoluted with the rf coil's sensitivity response at that location. This would influence only K and C of equation 3-2,

and not the exponential time constant. Thus, this investigation verified experimentally the theoretical prediction.

This result is significant for the following reason. Although it is tempting to make a differential diagnosis based upon differences in signal intensities (e.g. if the liver is more intense than the spleen then diagnosis A, if vice versa then diagnosis B), these differences may not be entirely organic in nature. Variations in calculated T1 values (for a constant set of imaging parameters) are a more reliable indicator of true clinical variation.

Dependence Upon Actual T1 Value

It was determined that the percentage of experiments which met the acceptance criterion was constant within 15% to the actual T1 value, for properly chosen values of the variable timing parameter. Since experiments were conducted over an actual T1 range of approximately 100 milliseconds to 1000 milliseconds, this result is valid only over this range. To justify this empirical result, it is necessary to consider two factors, the physical model of spin-lattice relaxation, and any instrumentational dependence upon T1 determination.

Spin-lattice relaxation theory predicts, for such a simple phantom material (paramagnetically doped water), a monoexponential relationship between the signal intensity and the variable timing parameter. The spin-lattice relaxation rate is directly obtainable from the exponential

time constant. This relatively simple relationship holds no T_1 dependent bias. That is, all other factors being equal, T_1 is simply a scaling factor in the exponential argument, and does not influence the general form of the function. Thus, the empirical invariance to T_1 was to be expected, on the basis of the physical model.

Although instrumental effects on T_1 determination can have many causes, ranging from rf field production to computer roundoff errors, there could not be any direct instrumentational dependence upon T_1 , for obviously the instrument could have no knowledge of the phantom's T_1 value. Thus, any T_1 dependent bias would have to have been indirectly related. Since T_1 calculations are based upon signal intensities and the values of a variable timing parameter, any direct instrumental bias towards these parameters will indirectly affect T_1 determinations.

The accuracy in defining a timing parameter was governed by the computer's CPU clock. If we consider a clock frequency of one megahertz (a value much less than even modern personal computers, let alone the PDP 11/24), then timing events could be controlled to within a microsecond. Since typical values of timing parameters were of the order of tens or hundreds of milliseconds, it seems unlikely that incorrectly set timing parameters were a large source of error in the determination of T_1 values.

On the other hand, the signal intensity was influenced by a myriad of variables, most of which were instrumental in

nature. For example, all experiments in this investigation utilized a single slice mode of acquisition. The use of multislice acquisition introduced other variables which influenced signal intensities, if all other factors remained constant.

Perhaps the greatest instrumental influence upon signal intensity was the required use of spin echo formation and imaging magnetic gradients for image signal acquisition. Conventional Fourier imaging [Ed80] relies upon the detection of spin echoes. This did not introduce further complications in the SE images, but PS, IR, and FIR experiments conventionally generate a free induction decay (FID) signal, and not an echo. Indeed, this complication could explain the poor performance of the PS sequence. The PS experiment relied upon the net magnetization's reaching a steady-state value while being subjected to repetitive $\pi/2$ rf pulses, but by its very nature a spin echo had a dynamically varying net magnetization. Although the IR and FIR experiments do not force the net magnetization to a steady-state value, altering their pulse sequence to include echo formation could have been a source of signal intensity error. The formation of spin echoes required the magnetization to remain in the transverse plane (in the rotating coordinate system) for an appreciable period of time. This introduced T2 damping of the signal intensity, and in the presence of magnetic field gradients, damping due to molecular self-diffusion [St65].

The empirically determined invariance to the actual T1 value is significant for two reasons. First, it permitted the development of general recommendations concerning the optimal values of the variable timing parameter. Second, it indicated that concerns raised about instrumental effects on T1 determination did not introduce any systematic errors in measurement, possibly only statistical errors. Thus, the results of this investigation could be applied to in vivo T1 determination without loss of accuracy due to any T1 dependence, to the extent that the phantom used in this investigation modeled the in vivo object.

Dependence Upon Number of Images

It was determined that for a given set of parameters, and with a fitting function with two degrees of freedom, the percentage of experiments which met the acceptance criterion was constant within 15% for the acquisition and use of two, three, or four images for T1 estimation. Similarly, for a fitting function with three degrees of freedom, the percentage of experiments which met the acceptance criterion was constant within 15% to the acquisition and use of three or four images for T1 estimation. This result agrees with the NMR spectroscopy literature, which states that to a first approximation, the error in estimated T1 values does not depend upon the number of data pairs used in the calculation, provided the rms error of the experimental data was less than one tenth of the signal intensity at time equal to infinity.

In this investigation, an estimated T_1 value was deemed a good approximation to the actual T_1 value if the relative error was less than 15%. For this acceptance level, only first order effects were of sufficient magnitude to influence the error in the estimated T_1 value. Therefore the observed invariance to the number of data pairs used in calculating the spin-lattice relaxation time corresponds to the NMR spectroscopy literature's suggestion concerning this point [Be80].

This result was of particular significant for the following reason. In NMR imaging, time is at a premium. This investigation sought to identify the method of spin-lattice relaxation time determination which maximized accuracy and precision, and minimized the total imaging time. One way to minimize the total imaging time was to take the least number of images required to generate mathematically unique and statistically significant results. Thus, for those techniques which were fitted by a function with two degrees of freedom, two images sufficed, while three were required for fitting functions with three degrees of freedom.

Since the earliest beginning of NMR imaging, some have made the suggestion that the best method of in vivo T_1 determination was the fitting of two SE images with a function with two degrees of freedom [Hr83, Ma79]. This result indicates that, if the signal to noise ratio was adequate in each image, two images would indeed be the reasonable number to acquire and process. This does not imply

that this method was optimal, but simply that it conformed to this "least number of images" result. Indeed, results of this work indicated that although the two image SE method was optimal in reducing the total imaging time, it was far from optimal in terms of its accuracy in estimating T_1 .

The summary of results presented in figure 3-13 contains much information concerning the appropriate choice of pulse sequence/fitting function for a given situation. The precision of each sequence was indicated by the corresponding percent of experiments meeting the acceptance criteria when the calculated T_1 was compared to the "Estimated T_1 " value. The least demanding situation was when the phantom was not immersed in the saline solution. For this situation all combinations of pulse sequence/fitting function were essentially equal in precision. This was not true when the phantom was immersed in the saline solution. In this situation the SE:2 method was slightly more precise than any other method of T_1 determination, all of which shared an essentially equal precision.

Those experiments whose calculated T_1 values met the acceptance criteria when compared to the "Natural T_1 " represented methods of determining precise and accurate T_1 estimates. For this situation both the IR:2 and FIR:2 methods were inadequate, whether the phantom was immersed in the saline solution or not. Additionally, both the IR:3 and FIR:3 methods of T_1 determination were best, while the SE:2 method performed marginally.

It was of importance to document to what degree a particular pulse sequence/fitting function varied from the "Salt" to "No Salt" case. To facilitate that analysis the percent relative difference was calculated from figure 3-13 for both the "Estimated T1" and "Natural T1" results. The percent relative difference was determined by subtracting the "% Meeting Criteria" of the "Salt" case from the "% Meeting Criteria" of the "No Salt" case, and then the result was divided by the "% Meeting Criteria" of the "No Salt" case. This was done for each pulse sequence/fitting function, for both the "Estimated T1" and the "Natural T1" results, with the outcomes given in figure 3-14.

Ideally, a given pulse sequence/fitting function would perform as well whether the phantom was immersed in the saline solution or was not immersed in the saline solution. Since this is the ideal situation, the ideal percent relative difference would be zero. The SE:2 method of T1 determination suffered the smallest loss of precision, as depicted in the "Estimated T1" result in figure 3-14. The "Natural T1" results indicated that the IR:3 was least prone to losses of accuracy and precision, while the SE:2 and FIR:3 methods were nearly as lossless. These results must not be considered out-of-context. For example, the result that the SE:2 method had a low percent relative difference for the "Natural T1" case viewed in conjunction with the results of figure 3-13 indicated that, in this particular situation, the SE:2 method went from being a poor method of

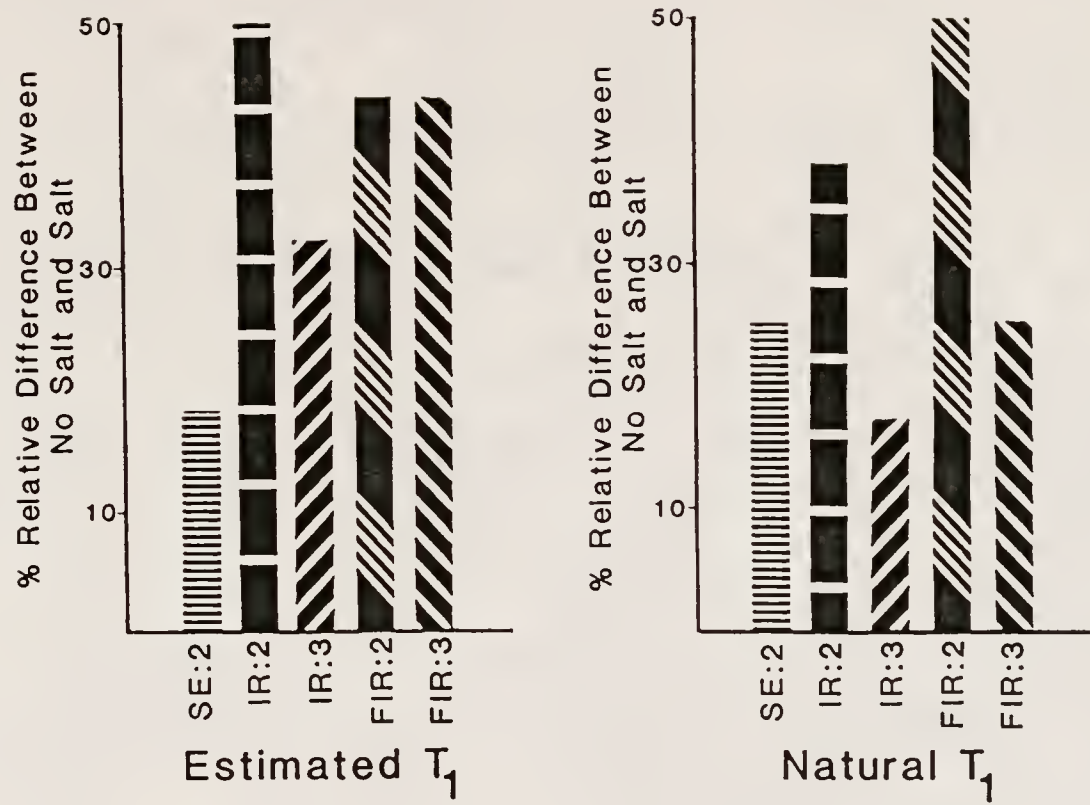


Figure 3-14. Effect of rf attenuating material upon measurement precision and accuracy.

determining accurate and precise T1 values when the phantom was not immersed in a saline solution, to being a slightly poorer method when the phantom was immersed in the saline solution!

A Priori Recommendations

All of the results of this investigation dealt with the determination of the optimal method of in vivo T1 values. Of primary importance were the results concerned with the optimal pulse sequence and optimal values of the variable timing parameter. These particular results may be used a priori to design an imaging scheme which results in reliable T1 values, or a posteriori to evaluate the reliability of a calculated T1 value. The a priori recommendations follow.

Optimal sets of parameters

The first decision to be made in the design of a T1 imaging series is the choice of pulse sequence. This decision is based upon three factors, total imaging time, and the accuracy and precision in T1 determination. The results indicate that there were three choices, three FIR images fitted by a three-parameter exponential function, three IR images fitted by a three-parameter exponential function, or three SE images fitted by a two-parameter exponential function.

The FIR series of T1 images had a number of advantages over the IR or SE series, which made it the recommended method. First, the method required, at most, half the total

time of the corresponding IR series. Second, it yielded consistent results, independent of whether the saline solution was present or not. Finally, it generated estimates of T_1 which were both accurate and precise. This meant that in vivo T_1 values could be obtained directly, without the need of a calibrated set of measurements.

There were also some disadvantages to the FIR series of T_1 images. First, being an inversion type of experiment, phase reconstruction of the images was required to make use of the full dynamic range offered by the technique. In practice, phase reconstruction is not always easily accomplished. Second, it did not always offer the minimum total imaging time. Often, the SE series of images would result in less total imaging time. Finally, the SE series often produced more precise measurements of T_1 than the FIR series did. Although the FIR series had some flaws, overall it was the most rugged method, yielding accurate and precise estimates of T_1 under the most adverse of situations.

The IR series shared many of the attributes of the recommended FIR series, but had an intrinsic tragic flaw. An IR image necessitated the use of a long total image time. This long IR would often clash with the clinical necessity of speed. An advantage the IR series had over the FIR was that, due to the extended IR time, less saturation of signal occurred. Thus, the IR images had slightly more contrast, an aid for visual evaluation, but no real advantage in the quantitative analysis required for T_1 determination.

The enigma of the investigation was the SE method of spin-lattice relaxation time determination. The SE series had many advantages. One, it often resulted in the shortest total imaging time. Two, only simple magnitude reconstruction was required. Finally, the SE series often attained estimated spin-lattice relaxation time values with very high precision. Additionally, although not a result of this investigation, the SE technique is often the clinical technique of preference, displacing the inversion techniques consistently. For these reasons, the SE method of spin-lattice relaxation time determination appears to enjoy the most widespread use. Additional results of this investigation indicated that the SE method had some serious shortcomings, and yielded quality results only in restrictive situations.

The most important disadvantage of the SE method was its lack of accuracy in estimating T1 values. The SE method always fared best when its estimated T1 value was compared to the T1 value determined by fitting all points, rather than when it was compared to the actual T1 value. Thus, in vivo T1 values could not reliably be determined directly. Instead, some type of calibration curve would need to be generated to permit actual T1 values to be gleaned from SE estimated T1 values. This conclusion agrees with other reported investigations into the use of SE images for T1 determination [Py83].

Optimum variable timing parameter values

Once the decision as to which pulse sequence to be utilized is made, either the SE, IR, or FIR imaging sequence, it is necessary to specify the values of the variable timing parameter. For FIR and IR images this is T_1 , while for SE images it is T_R . To insure optimal accuracy and precision, the results of the linear multiple regression analysis should be used. The derived linear relationships among the three values of the variable timing parameter for the FIR, IR, and SE methods have been given in equations 3-3, 3-4, and 3-5 respectively.

There are some general guidelines to be offered as to how best to use the suggested results a priori. First, the greater the uncertainty in the T_1 value under investigation, the greater should be the spread in the three values. The lowest value, L , could be picked to correspond to the shortest permissible value of the particular timing parameter. For the instrumentation used in this investigation, that was 25 milliseconds for T_1 and 100 milliseconds for T_R . The highest value of the timing parameter, H , would vary depending upon the pulse sequence. For the FIR and IR methods, H could correspond to some value close to T_R , say 0.9 T_R . The solution is not as straight forward for the SE method, where there is no fixed timing parameter of relevance on which to base the choice. In this case, H should be chosen with consideration towards the largest value in the expected T_1 range.

Often it is desired to merge the T1 determining images with the images desired for visual evaluation. In this case, one or two of the values for H, M, or L may be taken to correspond to the values associated with the images required for visual evaluation, with the remaining timing parameter determined by the linear multiple regression equation. For example, two SE images with the IR values of 500 milliseconds and 1000 milliseconds are desired for visual evaluation. Additionally, an in vivo T1 determination is desired of a tissue whose T1 is thought to be about 650 milliseconds. By setting L and M to 0.77 and 1.54, respectively, and utilizing the linear multiple regression equation for the SE method, H is determined to be 3.16, corresponding to a IR value of 2055 milliseconds. Note that nonsense answers would result, in this particular case, if the two existing IR values were assigned to L and H, or M and H. Additionally, if the T1 of concern was thought to be 350 milliseconds, then assigning M to be 0.77, and H to be 1.54 yields the third value of IR as 145 milliseconds. By a similar process, the optimal values of the timing parameters in FIR and IR series are determined.

In the manner just described, an optimal method of in vivo T1 determination may be developed a priori, based upon the available imaging time, desired accuracy and precision, and range of T1 under investigation.

A Posteriori Recommendations

It frequently happens that the desire for a quantitative determination of T_1 is not expressed until after the imaging series is completed. If the images were acquired along the lines of either the FIR, IR, or SE methods outlined earlier (i.e. three images were acquired, all with the same number of signal averages), then it would be possible to generate an estimated T_1 value, and with the aid of the linear multiple regression equations, determine the reliability of the estimate. The procedure is explained in the following scenario.

Three inversion type images were acquired, with TE equal to 30 milliseconds, TR equal to 1500 milliseconds, and three values of TI equal to 50, 550, and 850 milliseconds. All images were acquired with four signal averages. A three-parameter exponential is fitted to the data, and an estimated T_1 value of 700 milliseconds is calculated. The question is: is this a reasonable T_1 value to expect this series of images to properly characterize, or is it just the result of some mathematical fitting routine which is insensitive to certain physical realities?

Since the value of TR is approximately twice the T_1 estimate, this series is comparable to the FIR method of T_1 determination. The linear multiple regression equation for the FIR series indicates that the optimal T_1 value, for this set of TI values, is 477 milliseconds. This is obviously not equal to the estimated value of 700 milliseconds, but the

linear multiple regression equation is not without error, presented in the form of standard error of estimates in L, M, and H.

By a simple propagation of error analysis of equation 3-3, the standard error of estimate in T_1 for the FIR method of T_1 determination, $\sigma(T_1)$, may be determined to be 152 milliseconds. Thus, the optimal T_1 value to be determined by the set of T_1 values used in this example is 477 ± 152 milliseconds. The estimated value, 700 milliseconds, is nearly 1.5 standard errors greater than the optimal mean value, and it is therefore deemed an unreliable estimate. This analysis could be conducted as easily for any IR or SE series of images.

CHAPTER IV EXPLOITING THE STIMULATED ECHO IN NMR IMAGING

Introduction

There is an adage that applies equally to all multipulse NMR experiments which states it is easier to induce spin echoes than not. Rather than ignore or suppress these additional echoes in NMR imaging experiments [Du84], this investigation sought to glean added information from them. In particular, this study exploited the unique properties of the stimulated echo (STE), as first identified by Hahn [Ha50], and further quantified by Woessner [Wo61]. Although new to NMR imaging [Fr85, Ha85, Sa85a, Sa85b], stimulated echoes have been successfully applied by Tanner to the measurement of translational self-diffusion coefficients [Ta70], by Lausch and Spiess to study infrequent jumps of complex molecules [La80, Sp80], and more recently to analyze slow rotational motions of molecular solids by Sullivan et al. [Su82]. Furthermore, other investigators conducting research into stimulated echo NMR imaging, concurrently with this investigation, have recently reported their initial findings [Fr85, Ha85].

This investigation is unique in that it is the first to indicate that stimulated echoes may be applied to NMR

imaging, to specifically outline how the stimulated echo may be applied, and to present actual images utilizing the specified methods.

In NMR imaging, image contrast from area to area in the object results predominantly from the differences of the spin density, the spin-lattice relaxation time, T_1 , and the spin-spin relaxation time, T_2 . With current instruments, contrast due to relaxation is achieved through the use of either the spin echo (SE) technique, or an inverting technique, such as the inversion recovery (IR) sequence. In particular, T_1 weighting is introduced in the SE sequence by the rapid repetition of the entire pulse sequence, resulting in signal saturation, while the IR technique introduces T_1 weighting by inverting the equilibrium magnetization, initially aligned along the positive z axis, and sampling its recovery with a $\pi/2$ rf pulse.

STE imaging introduces T_1 weighting into the NMR image in the following manner. Viewed from the rotating frame of reference, an initial $\pi/2$ rf pulse, at time equal to zero, rotates the equilibrium magnetization into the transverse plane. While in the transverse plane, the net magnetization is reduced due to T_2 relaxation, molecular diffusion and precession within an inhomogeneous magnetic field. A second $\pi/2$ rf pulse, at time equal to τ_1 , will split the net magnetization equally into two orthogonal components, one of which lies in the transverse plane and the other which lies in the longitudinal plane.

The individual isochromats which comprise the net transverse magnetization will constructively interfere to form the primary echo (PE) at a time equal to twice τ_1 . The net longitudinal magnetization will be reduced due to T_1 relaxation and molecular self-diffusion. At a time τ_2 after the second 90 degree rf pulse, a third 90 degree pulse is applied which rotates this T_1 reduced net longitudinal magnetization back into the transverse plane, where the individual isochromats constructively interfere to form the STE at a time τ_1 after the third 90 degree rf pulse. It is precisely this ability to store and retrieve magnetization along the longitudinal direction, where T_1 relaxation occurs, which makes the application of the STE to NMR imaging unique.

Conventional Fourier NMR imaging [Ed80] relies upon spin echo formation for data acquisition. This investigation was unique in that it introduced the use of the STE for data acquisition in NMR imaging. STE imaging, with its unique T_1 dependence, is an ideal technique for T_1 contrast imaging. As indicated, there are two viable methods of T_1 contrast imaging currently in widespread use, the SE and IR techniques. Although the IR sequence has produced excellent results, there are a number of distinct drawbacks to its implementation. For example, one must insure a proper inverting pulse and use phase sensitive reconstruction to fully exploit the dynamic range afforded by the technique. The SE sequence is intrinsically a T_2 dependent technique,

hence images acquired with this sequence will frequently contain a high degree of mixed T1 and T2 contrast. The results of this investigation indicate that, in many ways, STE imaging bridges the gap between the accuracy of the IR technique, and the efficiency of the SE imaging technique.

The results of this investigation took the form of specific applications of the STE to NMR imaging. First, it was shown that in addition to generating T1 contrast images, it was possible to calculate quantitative T1 information from a series of STE images in which the storage time had been systematically varied. Second, a novel application of the T1 weighted STE image was obtained: the enhancement or suppression of elements in the object with different T1 values. Third, it was demonstrated that the STE was easily integrated into chemical shift imaging schemes. Fourth, two STE imaging methods were developed which permitted the acquisition of a series of STE images within one imaging sequence, where each image was progressively weighted by increasing T1 relaxation damping. Finally, a method of in vivo determination of molecular translational self-diffusion coefficients, which utilized the STE's unique T1 dependence, was proposed.

Theory

Introduction

Echo phenomena have long held a prominent role in spectroscopy, with applications in various fields spanning from magnetic resonance to laser spectroscopy. Echoes were

detected in NMR for the first time in 1950 by Hahn [Ha50], and spin echoes have subsequently been applied in NMR to various ends, including the measurement of T1 values [Ca54], the investigation into molecular diffusion processes [St65], the determination of scalar coupling constants [Fr75], the indirect detection of magnetic resonance [Em60], coherence transfer [Ma78], and NMR imaging [Ed80]. Also, the same effects have been exploited in electron spin resonance [Mi72], microwave spectroscopy [Gl76], and in laser optical spectroscopy [Ku64].

An echo is usually created by exciting the system under investigation at least twice, where the excitation is often pulses of electromagnetic radiation. All species in the system experience the same initial pulse, hence a coherence is produced. In time, inhomogeneous interactions within the system act to destroy the coherence. This is accomplished in NMR by an inhomogeneous magnetic field, by an inhomogeneous Stark field in microwave spectroscopy, or by the Doppler effect in optical spectroscopy [Ma78]. A second pulse, applied at a time τ , inverts the accumulated effects of the inhomogeneous interaction. Thus, the initial coherence is regained and an echo occurs at a time 2τ . Under particular conditions, portions of the coherence will continue to defocus, even after the application of the second pulse, and hence will not participate in echo formation. This component is dubbed the narcissus, after Narcissus in Greek mythology, who refused the love of Echo [Ha58].

In 1946, Bloch introduced a phenomenological vector equation to describe NMR [B146]. It accurately characterized an isolated particle of spin 1/2 in the presence of a static magnetic field. Feynman et al. [Fe57] have demonstrated that this description is complete, that is, a geometric representation of the Schrödinger equation is possible. Also, Pegg et al. [Pe81] have shown this description to be perfectly rigorous, because the vectors are equivalent to Heisenberg operators in the Heisenberg representation of quantum mechanics. It was advantageous to utilize this graphical method of analysis, and results derived in this manner are correct without restriction.

Bloch's model of NMR assumed that the magnetization of bulk material, influenced by a magnetic field, conformed to the laws of classical electrodynamics. Based on this premise, a vector differential equation was developed relating the bulk magnetic moment vector, M , to the applied magnetic vector field, B , such that

$$dM/dt = \Gamma(M \times B) \quad [4-1]$$

where Γ is a proportionality constant called the gyromagnetic ratio. The geometric interpretation of equation 4-1 is that the magnetic moment rotates about the applied magnetic field with the frequency ω , such that

$$|\omega| = |\Gamma B| \quad [4-2]$$

This relationship between the precession frequency and the applied magnetic field is referred to as the Larmor equation. The frequency ω is the Larmor frequency. The Larmor equation, expressed as in equation 4-2, indicates that the precessional frequency ω is proportional to the magnetic field B , where Γ is the constant of proportionality.

The Larmor equation may be obtained from an argument based upon classical physics, as outlined here, or derived in identical form from a quantum mechanical argument. This unique property indicates why the classical formulation offers added insight into the NMR phenomenon. Additionally, the absence of the Planck constant in the Larmor equation given in equation 4-2 further justifies the classical treatment of the resonance phenomenon.

Further support of the classical formulation of the NMR phenomenon is offered by the correspondence principle of quantum mechanics [Wa53], which is based on the assumption that quantum theory, or at least its formalism, contains classical mechanics as a limiting case. This idea was first expressed by Planck [Pl06], when he showed that in the limit the Planck constant approaches zero, all quantum theoretic conclusions converge towards classical results.

Formation of the Primary Echo Image

Consider a spin system in thermal equilibrium with its surroundings, subjected to the rf pulse and magnetic field gradient experiment displayed in Figure 4-1. In the graphical representation of Figure 4-2a, the initial

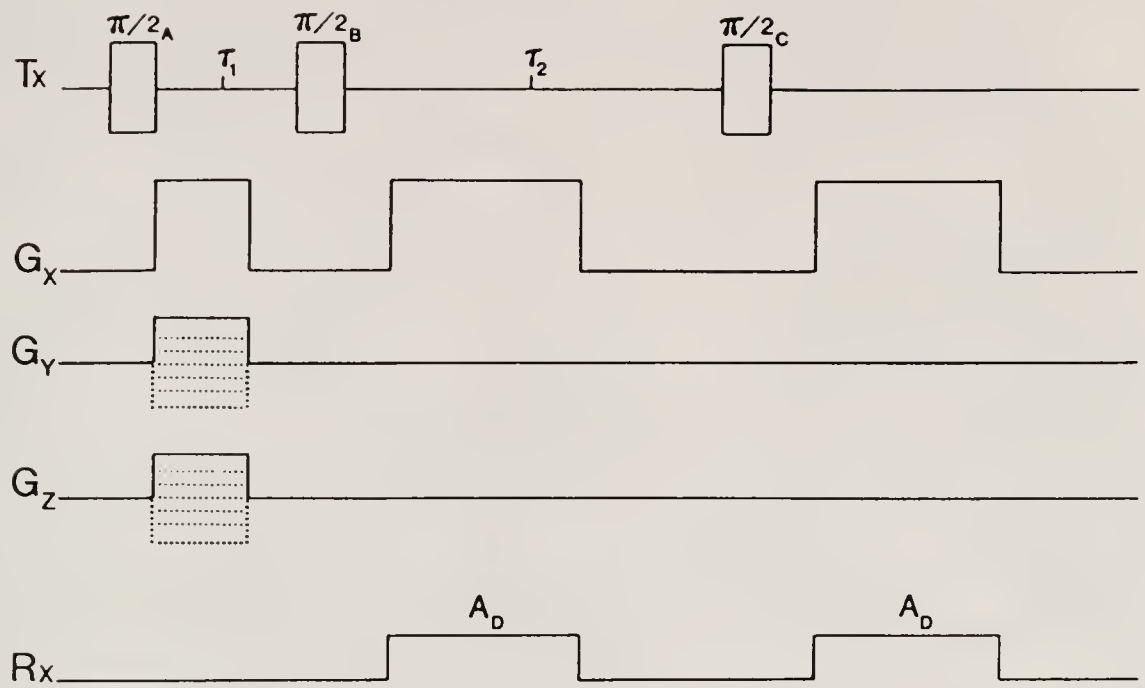


Figure 4-1. Basic stimulated echo imaging sequence.

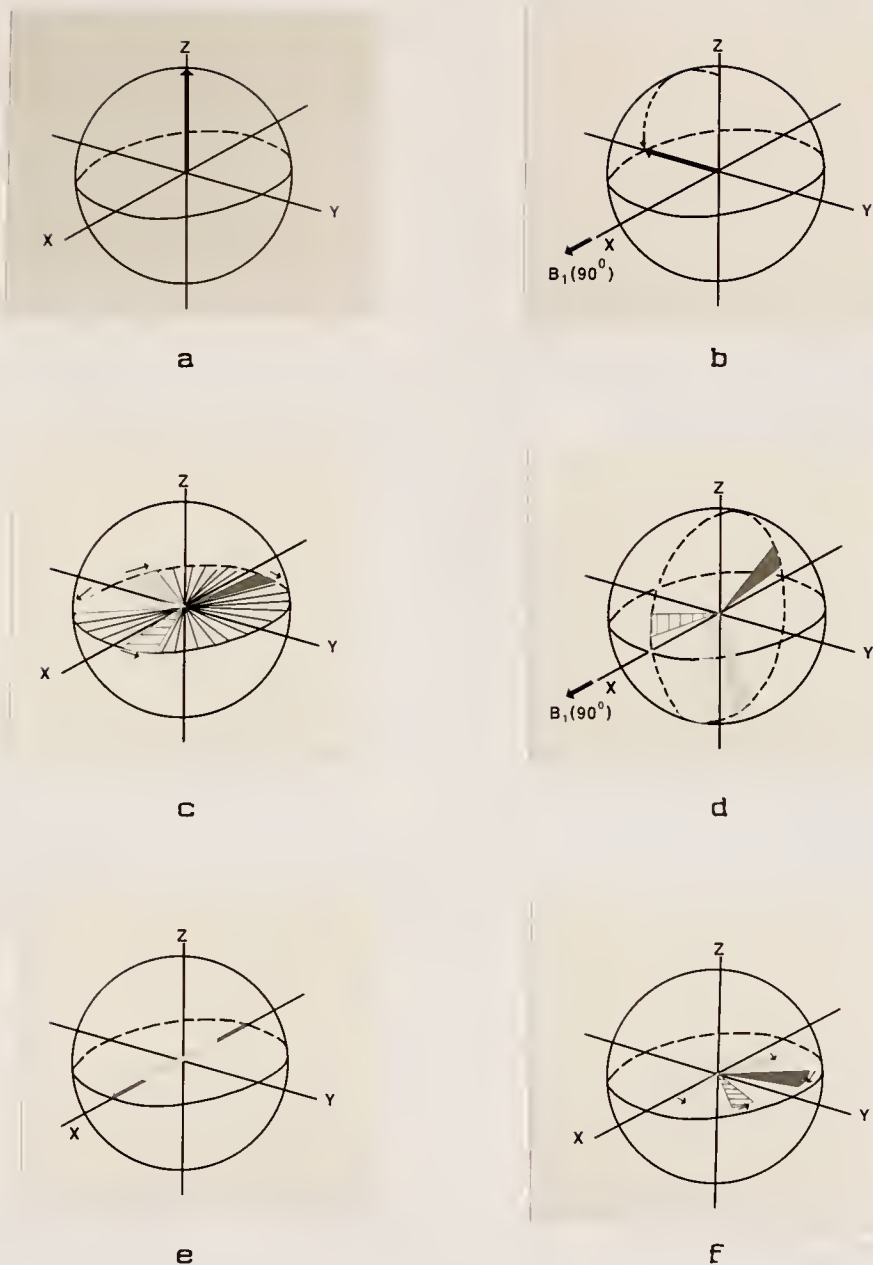


Figure 4-2. The formation of a primary echo.

equilibrium magnetization of the spin system, M_0 , is depicted as being initially aligned along the z direction, coaxial with the main magnetic field. The net magnetization is rotated into the plane transverse to the main magnetic field by the transmission (T_x) of a 90 degrees, or $\pi/2$ rf pulse applied as shown in figure 4-2b. It is assumed that the rf pulse is of frequency $\omega(p)$ and width $t(p)$, such that $t(p)$ is small compared to T_1 and T_2 , and excites the entire chemical shift frequency bandwidth equally. If, for example, the rf pulse has a phase α equal to 90 degrees (i.e. along the positive x direction as depicted in Figure 4-2b), then the transverse magnetization will initially be aligned with the negative y direction, in the rotating frame of reference.

The rotating frame of reference refers to a set of axes which are rotating about the z axis, the direction of the main applied magnetic field. The z axis of the rotating frame is parallel to the z axis of the laboratory frame of reference, as defined by the main applied magnetic field. The two rotating axes orthogonal to the z axis rotate with an angular speed equal to the effective component of the rf magnetic field. The rotating axis in the direction of the rf magnetic field is referred to as the in-phase component, while the other axis is the out-of-phase component. The rotating frame of reference is a useful construction for two reasons. One reason is that the phenomenological vector equation which describes NMR takes on a simpler form when

expressed in terms of the rotating frame of reference. Also, a simpler physical picture of events is possible when considered in the rotating frame of reference.

For a given nucleus, theory indicates that resonance occurs at a single frequency, dictated by the main magnetic field strength as in equation 4-2. In practice, resonance takes place over a range of frequencies determined by the inhomogeneity of the main magnetic field throughout the sample. Therefore, the object may be considered to be comprised of an ensemble of magnetic moments, whose resonance frequencies are symmetrically distributed about the Larmor Frequency, ω . Figure 4-2c illustrates the free precession (i.e. Larmor type precession and not rf pulse induced rotation) of all these isochromats during the time interval τ_1 . Since figure 4-2c depicts the dynamics of the magnetization in a frame of reference rotating at frequency ω , the isochromatic moment pairs maintain a symmetry about the y direction, but rotate in opposite directions. This is indicated in figure 4-2c in the following manner. The light gray regions represent a range of isochromats which deviate less from ω than do the range of isochromats represented by the dark gray, that is, the light gray region precesses slower than the dark gray region, in this frame of reference. In each case, solid area versus hatched area indicates positive versus negative deviation from ω .

Within this time interval τ_1 , pulsed linear magnetic field gradients are applied as in the conventional Fourier

imaging technique [Ed80]. The preparatory readout gradient is embodied in the effective x gradient, (G_x), whereas G_y and G_z are employed for phase encoding. The effect of these pulsed magnetic field gradients is the spatial encoding of the NMR signal in a precise manner. If one, two, or three orthogonal pulse field gradients are used for image formation, then a one, two or three dimensional Fourier transform of the time domain NMR signal will result in an image where signal intensity is a function of one, two, or three spatial dimensions. Obviously, z direction discrimination could also be achieved with a selective $\pi/2$ rf pulse applied in the presence of a slice selective G_z [Ho77].

After the time interval τ_1 , a second 90 degree rf pulse is applied, as indicated in figure 4-2d. Whereas prior to the second rf pulse all magnetization was lying in the transverse plane (assuming negligible T1 relaxation during the interval τ_1), after the second rf pulse the net magnetization has components in the longitudinal plane as well as the transverse plane. Figure 4-2e illustrates the transverse component of the net magnetization immediately following the second rf pulse, obtained by simply projecting the net magnetization of figure 4-2d onto the transverse plane. Since prior to the second rf pulse all magnetization was lying in the xy plane, all magnetization after the second pulse lies in the xz plane (if the rf pulse is applied along the positive x direction as indicated), hence

the projection of the net magnetization onto the transverse plane, immediately following the second rf pulse, lies completely on the x axis.

The intrinsic properties of the isochromats have not been altered by this magnetization gymnastics. The sense and speed of free precession in the transverse plane for the isochromats following the second rf pulse is identical to the sense and speed of free precession prior to the second rf pulse (i.e. as indicated in figure 4-2c). Hence, from time τ_1 on, the isochromats will freely precess as in figure 4-2f. From time τ_1 to time $2\tau_1$ the isochromat vectors will interfere amongst themselves, with maximum constructive interference occurring at time $2\tau_1$. This constructive interference constitutes a primary echo (PE), with maximum amplitude at time $2\tau_1$, and so named to distinguish it from the spin echo which results from a $\pi/2-\tau-\pi$ rf pulse sequence. The maximum amplitude of the PE at time $2\tau_1$, $M(PE)$, is given by

$$M(PE) = M_i \sin \theta_i \sin^2 \left(\frac{\theta_i}{2} \right) \exp(-2\tau_1/T_2) f(G, D, \tau_1) \quad [4-3]$$

where M_i is the equilibrium magnetization, θ_i is the tip angle of the i th pulse, and $f(G, D, \tau_1)$ corresponds to the diffusional damping resulting from molecular diffusion in the presence of magnetic field gradients. For a constant steady magnetic field gradient, $f(G, D, \tau_1)$ is given by

$$\exp\left(-\frac{2}{3}D\Gamma^2 G^2 \tau_1^3\right), \text{ where } G \text{ is the magnetic field gradient}$$

and D is the translational self diffusion coefficient. It should be noted that pulsed magnetic field gradients have been used in this investigation, hence the functional form of $f(G, D, \tau_1)$ will be different [St65]. The two cases are identical, in the limit, as we pass from pulsed to continuous application of the gradient.

As illustrated in Figure 4-1, the G_x readout gradient is imposed, centered about the time $2\tau_1$, to frequency encode the PE with x direction spatial dependence. Additionally, the receiver (R_x) is gated open during this same time, to permit acquisition (A) of the spatially encoded PE. If all pulses are ideal $\pi/2$ rf pulses, then the PE image is identical to the image produced by conventional spin echo imaging, except for a factor of one half in signal intensity. This reduction in the signal to noise ratio would be intolerable unless it is possible to recover it, or reap some compensating benefit. Fortunately the other half of the magnetization is not dissipated, rather it has been stored as longitudinal magnetization by the second $\pi/2$ rf pulse.

Formation of the Stimulated Echo Image

It can be shown that the solution to the Bloch equation in the rotating frame [B146] takes on the form

$$M_x(t+tp) = M_x(t) \quad [4-4]$$

$$M_y(t+tp) = M_y(t)\cos\theta - M_z(t)\sin\theta \quad [4-5]$$

$$M_z(t+tp) = M_y(t)\sin\theta + M_z(t)\cos\theta \quad [4-6]$$

in response to a rf pulse about the x axis commencing at time t and of width tp , corresponding to a tip angle of θ degrees. In this representation the rotating portion of the net magnetization is decomposed into two orthogonal components. M_x is taken to be in phase with respect to the x axis rotating frame of reference, while M_y is 90 degrees out of phase. Of prime interest is equation 4-6, which characterizes the longitudinal magnetization, and in particular its dependence on $M_y(t)$. Since the spin system is initially in thermal equilibrium, $M_y(t=0) = 0$. Hence, by equation 4-6, $M_z(t=tp) = 0$ for an ideal $\pi/2$ rf pulse. As applied to the experiment of figure 4-1, the implication is that during the interval τ_1 , M_z simply approaches the equilibrium magnetization, if the effect of relaxation is considered.

If τ_1 is of the order of T_2 or less, then $M_y(t=\tau_1)$ is surely nonzero. That is, at time τ_1 we will have appreciable transverse magnetization. Therefore the second $\pi/2$ rf pulse, in addition to inducing the PE, will also produce net longitudinal magnetization, that is, $M_z[t=\tau_1+tp]$ is nonzero. This becomes quite apparent when a graphical analysis is conducted.

Figure 4-3a is simply the graphical representation of the net magnetization immediately following the second $\pi/2$ rf pulse of figure 4-1. Indeed, figure 4-3a is identical to figure 4-2d. Whereas we considered the transverse projection of this net magnetization in order to describe the formation

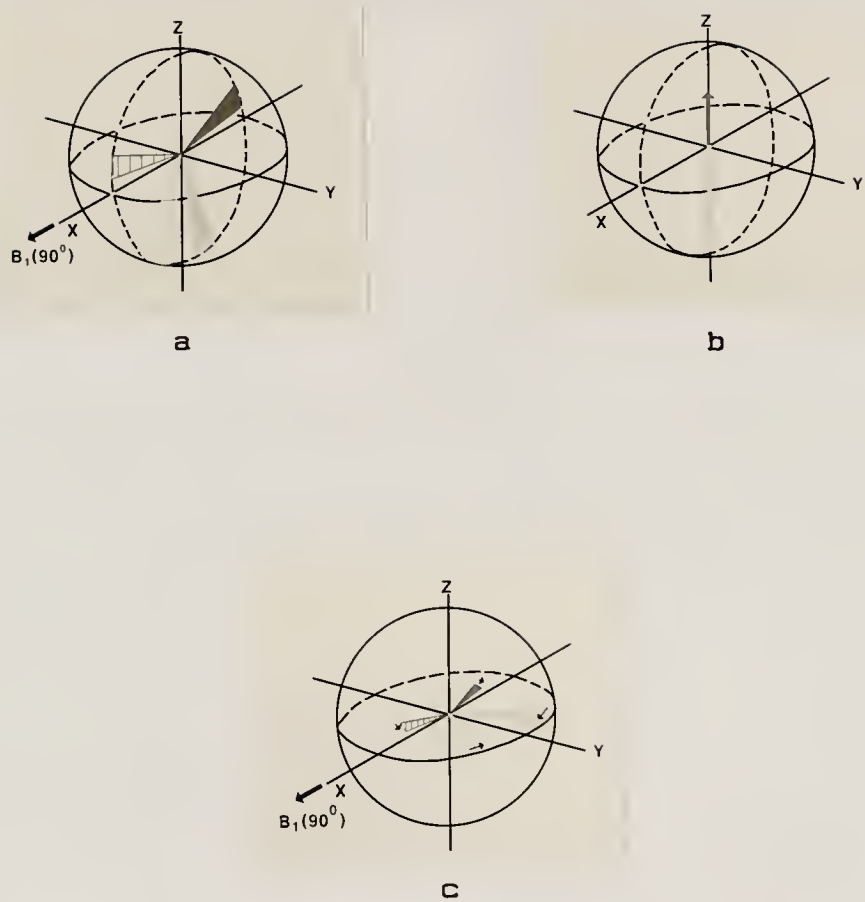


Figure 4-3. The formation of a stimulated echo.

of the PE, we now consider the longitudinal component of the net magnetization immediately following the second rf pulse, illustrated in figure 4-3b. For the duration of τ_2 the longitudinal magnetization is affected solely by spin-lattice relaxation. Furthermore, even the readout pulsed magnetic field gradient for the PE image does not influence the longitudinal magnetization.

The third 90 degree pulse, which comes at the end of the τ_2 interval, simply rotates the stored longitudinal magnetization back to the transverse plane, as depicted in figure 4-3c. The intrinsic properties of the isochromats have not been altered by the additional magnetization gymnastics. Indeed, the sense and speed of free precession in the transverse plane for the isochromats following the third rf pulse is identical to the sense and speed of free precession prior to the second rf pulse, which is indicated in figure 4-2c. Hence, after the application of the third rf pulse, the isochromats will freely precess as in figure 4-3c. Since the only time this magnetization was influenced by the inhomogeneous main magnetic field was during the interval τ_1 , the isochromat vectors will interfere amongst themselves during the interval τ_2 , with maximum constructive interference occurring at a time τ_1 after the third rf pulse, for $\tau_2 > \tau_1$. This constructive interference constitutes the stimulated echo (STE), with maximum amplitude at a time τ_1 past the application of the third rf pulse. Thus, the maximum amplitude of the STE at a time τ_1 after the third rf

pulse, $M(SIE)$, is given by

$$M(SIE) = 1/2M_i \sin\theta_1 \sin\theta_2 \sin\theta_3 \exp[-(2\tau_1/T_2 + \tau_2/T_1)] * F(G, D, \tau_1, \tau_2) \quad [4-7]$$

where θ_i is the i th rf pulse, and $F(G, D, \tau_1, \tau_2)$ is the diffusional damping term for the SIE. For a constant steady magnetic field gradient, $F(G, D, \tau_1, \tau_2)$ is given by

$$\exp[-(2/3)D\Gamma G (\tau_1 + \tau_1 \tau_2)],$$
 and is modified for pulsed magnetic field gradients [Ta70].

The relaxation damping term tells the history of the magnetization that went into the SIE's formation. Since spin-lattice relaxation occurred only within the interval τ_2 , the magnetization must have been stored along the longitudinal direction during that interval. Likewise, the magnetization can be traced to the transverse direction for both the τ_1 interval between the first and second rf pulse, and also for a time τ_1 subsequent to the third rf pulse, for a total time of T_2 influence amounting to $2\tau_1$.

As illustrated in Figure 4-1, the G_x readout gradient is imposed, centered about a time τ_1 after the third rf pulse, to frequency encode the SIE with x direction spatial dependence. Additionally, the receiver (Rx) is gated open during this same time, to permit acquisition (A) of the spatially encoded SIE. If each θ_i was an ideal $\pi/2$ rf pulses, and ignoring relaxation and diffusional damping, it is noted from equation 4-7 that $M(SIE)$ is proportional to

$(1/2)M_i$. This is the other factor of one half we noted earlier after the formation of the PE. Whereas the conventional spin echo imaging experiment yields a single image whose intensity is proportional to M_i , the stimulated echo imaging sequence may yield two images, each proportional to $(1/2)M_i$, and each in spatial registration with the other. The utility of these images lies not in this proportionality, but rather in the unique T_1 dependence of the SIE image. Applications which further extend and exploit this T_1 dependence are presented later in this chapter.

Formation of Secondary Echoes

As was previously outlined, the rf pulse sequence given in Figure 4-1 will yield both the primary echo and the stimulated echo. Additionally, the application of the three $\pi/2$ rf pulses may yield up to three other secondary echoes, for a total of five echoes resulting from three rf pulses. The origins of these secondary echoes are as follows.

The same echo formation mechanism which results in the primary echo after the application of the first two rf pulses may also cause the formation of two of the three secondary echoes. If we consider the three rf pulses taken two at a time, then there are three unique combinations, the first and second pulses, the first and third pulses, and the second and third pulses. Each combination will result in an echo, with the first case simply being the primary echo. The second case results in an echo at a time $\tau_1+\tau_2$ after the third rf pulse, and the third case results in an echo at a

time τ_2 after the third rf pulse. Each of these echoes will have different T2 weighting, dependent upon the time the magnetization spends in the transverse direction.

The final secondary echo is derived from the PE. At time τ_1 after the second rf pulse the PE has an amplitude maximum. That is, at this time, the coherence imparted by the first rf pulse has been regained. Indeed, there is as much coherence amongst the isochromats which comprise the PE at time τ_1 after the second rf pulse as there was immediately following the first rf pulse, ignoring the coherence lost due to relaxation and the diffusion process. Therefore, for all intents and purposes, the PE at time τ_1 after the second rf pulse behaves as if it was transverse magnetization just after the application of a rf pulse. Thus, after the time τ_1 past the second rf pulse, the isochromats which comprise the PE will begin to lose coherence until the third rf pulse acts to refocus them, resulting in an echo at a time $\tau_2-\tau_1$ after the third rf pulse.

Thus, the application of three rf pulses may result in as many as five echoes. Each of these echoes could be used for image formation, although the simplicity of the PE and the unique T1 dependence of the STE make these two echoes ideal for image formation. The addition of a fourth rf pulse results in the formation of eighteen echoes, and an example based upon this extended sequence is given late in the chapter.

Materials and MethodsThe NMR Imager/Spectrometer Systems

All proton NMR experiments were conducted on one of two NMR imager/spectrometer systems. The majority of experiments were performed on a Nicolet (GE-NMR) NI-80 spectrometer located in the Department of Radiology at the University of Florida. A single experiment, the TART imaging sequence, was conceived and developed at the University of Florida, but was implemented on a prototype General Electric CSI imager/spectrometer located in the applications lab of General Electric NMR Instruments, Fremont, California.

The Nicolet (GE-NMR) NI-80 spectrometer was coupled with an Oxford 80/310 MR superconducting magnet operated at 1.89T, with a clear bore diameter of 31 centimeters. Transient gradient pulses were generated with the Oxford 2320 room temperature shim power supply, which was modified by J.R. Fitzsimmons and R.G. Thomas so as to improve its temporal response time. The power supply was under the direct control of the Nicolet 293C pulse programmer, so as to allow pulse control of the x, y, and z gradients. Controlling software was written in Nicolet 1280 assembly language by I.H. Mareci, M.D. Cockman, and R.G. Thomas. The DAC outputs to x, y, and z were dependent upon the state of six TTL inputs, two for each direction so as to allow pulse sequences to be implemented which required the sign of the magnetic gradient pulse to be reversed in the course of the experiment. These six TTL inputs, U, A, V, C, W, and H

(corresponding to x, y, and z respectively) could be gated on during any pulse or time delay in the imaging pulse sequence.

Imaging pulse sequences were generated directly with the available pulse sequence generating software resident on the Nicolet system, once the pulsed magnetic gradient controlling hardware/software was implemented. Additional assembly language software was developed by M.D. Cockman to permit the sequential incrementation of the pulsed magnetic field gradients, required for the Fourier imaging technique used in this investigation.

The Nicolet spectrometer uses a twenty bit word length, hence single precision data acquisition resulted in twenty bit deep data. In conjunction with M.D. Cockman, an assembly language routine was developed which scaled the twenty bit deep data to five bits (permitting image display with thirty-two gray levels), and transferred the scaled data over a RS232 transmission line to a Cromemco Z-2D computer for image processing and display. The image processing and display software was developed by L.T. Fitzgerald. All images presented, except those associated with the TART experiment, were acquired and processed in a like manner, unless otherwise noted. The images generated with the TART experiment were acquired and processed with the resident hardware and software which was standard on the General Electric CSI imager/spectrometer.

Residual Gradients

As outlined in the previous section, the stimulated echo imaging scheme of figure 4-1 has, as its backbone, the rf pulse sequence $\pi/2 - \tau_1 - \pi/2 - \tau_2 - \pi/2$. A PE image is obtained at a time τ_1 after the second $\pi/2$ rf pulse, with relaxation weighting $\exp(-2\tau_1/T_2)$. The STE image is obtained at a time τ_1 after the third $\pi/2$ rf pulse, with its relaxation weighting given by $\exp(-2\tau_1/T_2)\exp(-\tau_2/T_1)$. Since the spatial encoding is identical for the PE image and the STE image, the two are in spatial registration, though residual gradients may act in a manner which alters this registration, as to be explained.

Consider the effect of residual gradients in the following gedanken experiment. Phase encoding pulsed magnetic field gradients are applied within the interval τ_1 of the basic STE imaging sequence as depicted in figure 4-1. Ideally there would be no residual gradients present, that is, there would be no field gradient once the current pulse which produced the phase encoding gradient had died down. Now consider the effect of a residual gradient which remains even after the current pulse ceases. All isochromats in the interval τ_1 will experience a phase shift θ as a result of the phase encoding pulsed gradient. At time τ_1 , half the magnetization is rotated to the longitudinal direction, and thus is no longer influenced by field gradients. The remaining transverse magnetization experiences a phase reversal of sorts at time τ_1 , which accounts for the

formation of the PE. If there is a residual gradient, the transverse isochromats will rephase in its presence, resulting in an additional phase shift of $\phi(\text{PE})$. The stored longitudinal magnetization is not influenced by the residual gradient until it is brought back to the transverse plane, where it rephases to form the STE. If a residual gradient is present, there will be an associated additional phase shift of $\phi(\text{STE})$.

Both $\phi(\text{PE})$ and $\phi(\text{SIE})$ are negative relative to π , for they were incurred after a phase reversing rf pulse, and $|\phi(\text{PE})|$ is greater than $|\phi(\text{SIE})|$, since the magnitude of a residual gradient is typically a monotonically decreasing function of time. Consequently, the PE experiences a total phase shift which is less than that of the STE by $|\phi(\text{PE}) - \phi(\text{SIE})|$. Since ideally there is a one-to-one mapping of total phase shift to spatial location, the different total phases of the PE image and the SIE image result in different spatial mappings along the phase encoding direction. That is, since the total phase of the PE is less than that of the SIE, the apparent extent of the phase encoded direction will be less in the PE image than in the SIE image. For example, points separated by 10 centimeters in the SIE image, along the phase encoded direction, might be depicted as having only an apparent 8 centimeter separation in the phase encoding direction of the PE image. Since the readout direction is essentially unaffected by the residual gradient, the aspect ratio for all STE images will

be, ideally, one, while for the PE images the aspect ratio will vary as a function of the magnitude of the residual gradient, and the time it is influential on the transverse magnetization. In all images presented, except those corresponding to the TART experiment, the phase encoding direction is displayed along the horizontal direction, or y direction.

To evaluate the residual gradient problem on the NI-80 spectrometer, the following experiment was conducted. A single one centimeter diameter vial of paramagnetically doped water was centered in the rf coil of the spectrometer. The magnet was then shimmed with the sample in place, resulting in an approximate 10 ppm line width. A pulse sequence was developed, and implemented, to evaluate the duration and extent of the residual gradient.

The pulse sequence consisted of six steps. The first step was simply a time delay, set equal to one second so as to insure the entire sequence was not so rapidly repeated as to cause signal saturation. The second step was the application of a pulsed magnetic field gradient of 0.18 mT/m, for a duration of two seconds. This duration was chosen so as to insure that the field gradient had sufficient time to reach its full magnitude. The next step in the sequence was a variable timing delay, which was incremented from 25 milliseconds to 725 milliseconds in 25 milliseconds increments, with a single initial value of one microsecond. At the end of this variable time delay, the

fourth step in the sequence commenced, a 90 degree rf pulse, with the next step simply the opening of the receiver gate. The sixth and final step in the sequence was a time delay equal to the total acquisition time, as dictated by the sweep width and the data acquisition block size. This permitted the receiver gate to remain open for the acquisition of the free induction decay (FID) resulting from the 90 degree rf pulse.

The significance of the experiment was as follows. Obviously, if there was no pulsed magnetic field gradient applied in step two, the signal intensities of the Fourier transformed FIDs would not be dependent upon the variable time delay of step three. Similarly, if there was a gradient applied in step two, but its magnitude was reduced to zero prior to the application of the $\pi/2$ rf pulse, then the resultant signal intensities from the transformed FIDs would still not be dependent upon the variable time delay of step three. Rather, consider the case where a gradient is applied in step two, and its magnitude had not reduced to zero prior to the application of the $\pi/2$ rf pulse. This is what is meant by a residual gradient, and in this case the corresponding signal intensities of the transformed FIDs will be reduced. Thus, by incrementing the variable time delay it was possible to temporally map out the extent of the residual gradient. The plot of signal intensity as a function of the variable time delay is given in Figure 4-4.

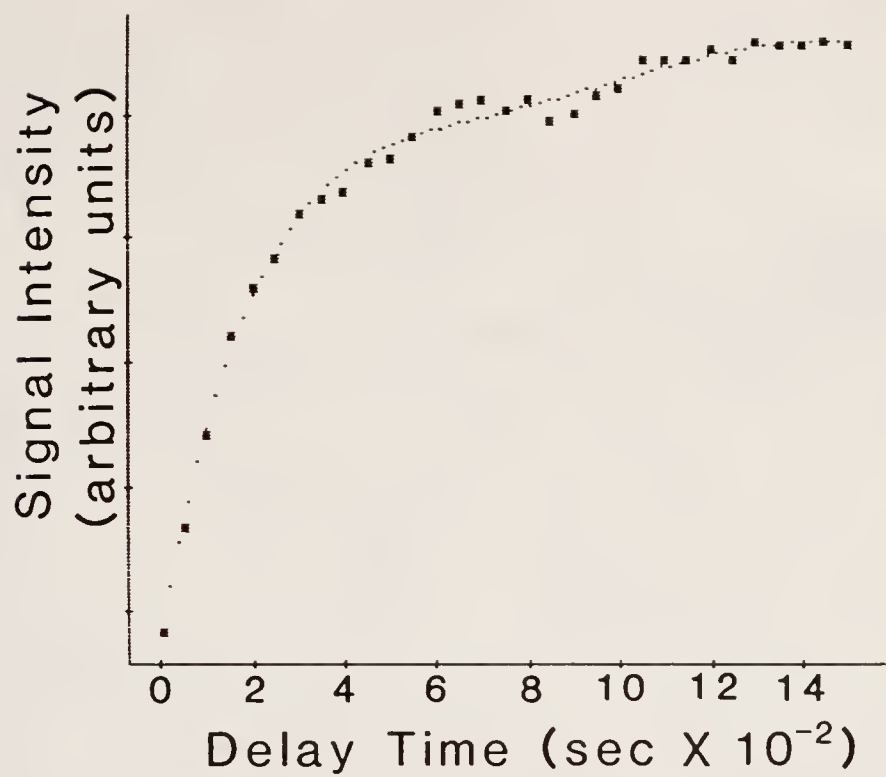


Figure 4-4. The evaluation of a residual gradient.

It was apparent from the results of this experiment that there was a residual gradient present after application of a pulsed field gradient, and its effect was significant for nearly 120 milliseconds. Since the magnitude of the field gradient used in this experiment was typical of the values used in the SIE imaging experiments, and since the time extent of the residual gradient was comparable to the time scale used in the experiments, it was concluded that the problem of residual gradients could not be ignored in this investigation.

Figure 4-5 illustrates the effect which the residual gradient has upon image formation. As outlined earlier, the effect of residual gradients was upon the spatial mapping in the phase encoding direction. The images are of two, one centimeter diameter vials filled with paramagnetically doped water. The images are displayed as intensity contour plots, rather than gray scale images. Horizontal is the phase encoding direction and vertical is the readout direction. The image in figure 4-5a was formed from transverse magnetization in the presence of a residual gradient for 100 milliseconds, while the image in figure 4-5b was in the presence of the residual gradient for 250 milliseconds, and figure 4-5c for 350 milliseconds.

As predicted, the more time the transverse magnetization spends in the presence of the residual gradient, the less is the apparent separation of the vials in the phase encoding direction. Indeed, in the limit where

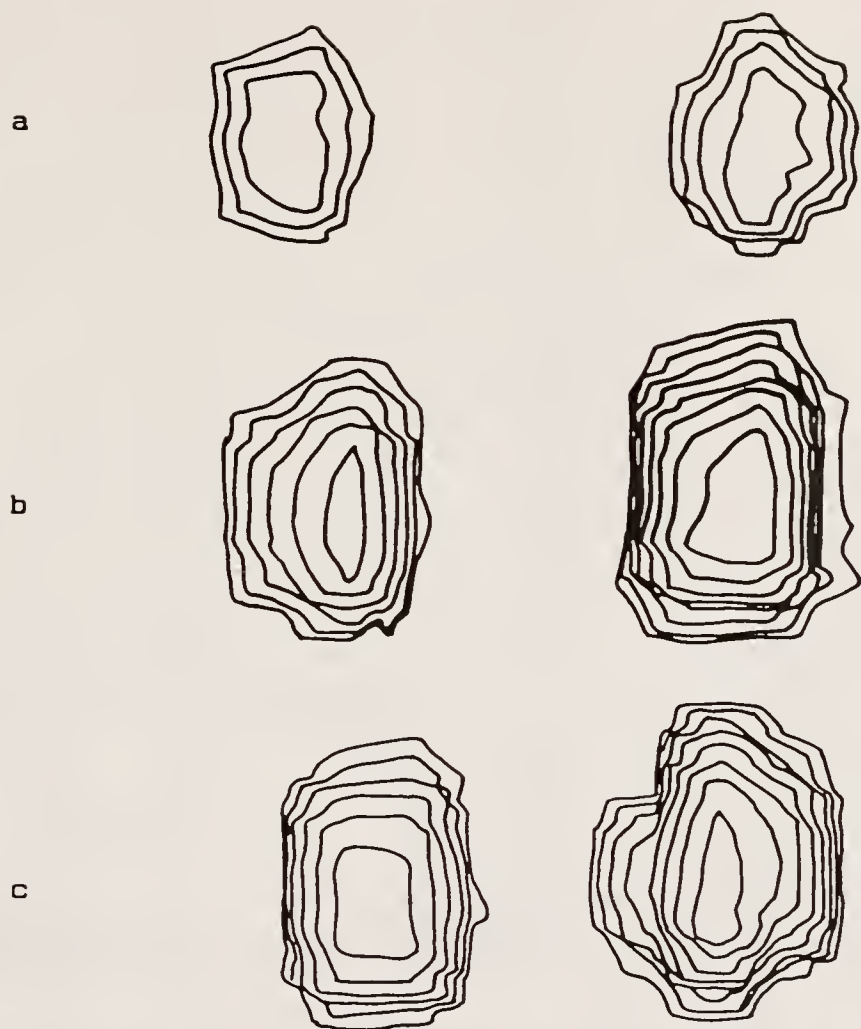


Figure 4-5. Effect of residual gradients on image formation.

the integrated effect of the residual gradient just balances that of the phase encoding gradient, there would be no effective phase encoding gradient, and hence no spatial separation in the image along the phase encoding direction.

Phase Cycling

A drawback to the SIE imaging sequence as described is its insensitivity to signed phase information. Because there is only pure amplitude modulation of the signal as a function of the gradients applied during the interval τ_1 , it would normally be necessary to set the Tx frequency outside the spectral frequency range, employ single phase detection, and use only one sided phase encoding gradients to avoid aliasing. Fortunately a simple modification afforded by phase cycling of the rf pulses and the receiver circumvented this problem by converting the amplitude modulation into phase modulation.

The two step phase cycling, used in conjunction with quadrature detection, consisted of the first two acquisitions as depicted in table 4-1. Here, A, B, C, and D refer to the phase of the rf pulses and the receiver, as illustrated in figure 4-1. Nagayamo et al. have used a closely related phase cycling procedure in spin echo correlated spectroscopy [Na79].

The first two phase cycling steps select the echo component of the transverse magnetization over the narcissus component. If either the main field inhomogeneity or the readout gradient was of sufficient magnitude to suppress the

Table 4-1

Four-Step Phase Cycling Used in
Stimulated Echo Imaging

<u>Acquisition</u>	Phase (degree)			
	A	B	C	D
1	0	0	0	0
2	270	0	0	90
3	180	0	0	180
4	90	0	0	270

narcissus component, then the two step cycle would not be needed, for only the echo component would be available for acquisition. Recall, the narcissus component is comprised of magnetization which continues to defocus even after the phase reversing pulse has been applied. The defocus of the narcissus would be advanced if the inhomogeneity of the magnetic field is enhanced, and a magnetic field gradient may be considered as just a large field inhomogeneity. Thus, the narcissus component would have defocused to essentially zero when the time came to acquire the echo. For this scenario, the two step phase cycling would be superfluous.

Although the two step phase cycling sequence was adequate, often it was extended to four steps in order to suppress artifacts resulting from longitudinal magnetization recovery during the interval τ_1 [Ba81]. The four step phase cycling is illustrated in its entirety in table 4-1. The phases of B and C are arbitrary, as long as they remain equal and constant throughout the entire experiment. For a properly adjusted instrument, and with all rf pulses being slice selective, the last two phase cycling steps in table 4-1 could be ignored. Indeed, under suitable conditions, SIE imaging could be conducted with a single step, without the need to phase cycle.

In practice, an additional spoiling pulsed magnetic field gradient was applied immediately following the primary echo's readout gradient, and prior to the third $\pi/2$ rf pulse, along G_x . This reduced artifacts in the stimulated

echo image by eliminating the three other possible overlapping secondary echoes which may occur after the third rf pulse. Since the STE's magnetization is stored along the longitudinal direction during the time interval τ_2 , the spoil pulse dispersed only the transverse magnetization which would have gone on to create additional secondary echoes subsequent to the third rf pulse.

Image Acquisition

Unless otherwise noted, all images acquired with the NT-80 spectrometer/imager were done so in a like manner. Although figure 4-1 indicates that Gz phase encoding was possible in the STE imaging sequence, none was performed in practice. This resulted in z direction averaged images (into the page). The reason for this was to save time and data storage space, and does not reflect any inherent limitation of the imaging system. The Gx readout gradient was 0.5 mT/m, and was applied for 32ms. There were 64 equal steps of the Gy phase encoding gradient, ranging from 0.5 to -0.5 mT/m, each applied for 16ms, excluding any contribution from residual gradients. The data matrix for each image consisted of 128 X 64 complex data points. The field-of-view was 10 X 10 centimeters, corresponding to a resolution of 1.5 millimeters in the y direction and 0.75 millimeters in the x direction. Four averages were done to take advantage of the four step phase cycling given in table 4-1. The $\pi/2$ rf pulse width was 260 microseconds. All pulse sequence repetition times were set so as to avoid signal saturation effects.

All images displayed corresponding to the TART experiment were acquired in the following manner. The two dimensional images were acquired with a field of view of 15 X 15 centimeters, and a slice thickness of 2 millimeters. Each image forming echo was defined with a data block size of 512 data points. There were 256 equal phase encoding steps. This resulted in a final image matrix of 512 X 512 points, after zero filling in both directions.

Experiments

Seven experiments which exploited the unique properties of the stimulated echo in NMR imaging were conducted. These experiments covered a wide spectrum of application. Presented in this section are the methods of using STE imaging to perform T1 contrast imaging, quantitative T1 imaging, water-lipid contrast imaging, chemical shift imaging, multiecho STE imaging, and diffusion coefficient weighted imaging.

Experiment one: T1 contrast imaging

To demonstrate the T1 contrast imaging capabilities of the STE imaging sequence, the basic imaging sequence given in figure 4-1 was used, in conjunction with the phase cycling scheme of table 4-1. The image phantom consisted of a red Delicious apple with a one centimeter vial of copper sulfate doped distilled water embedded in its center. A short τ_1 value was used to emphasize the poor T1 contrast of the PE image, while the long τ_2 value emphasized T1 differences dramatically in the STE image.

Experiment two: quantitative T1 imaging

In addition to T1 contrast imaging, STE imaging permits the quantitative measurement of T1 values. It can be shown that the diffusional damping of the STE, $f(G, D, \tau_1, \tau_2)$, is functionally dependent on τ_1 to second and third order, for both constant and pulsed magnetic field gradients [Ha50, Ta70]. Hence, an analysis of equation 4-7 yields the result that for τ_1 very small, a plot of the logarithm of the stimulated echo's maximum amplitude versus τ_2 will yield a straight line whose slope is a measure of T1. If the effect of diffusion is not completely negligible, such that corrections for higher order in τ_1 must be made, then a better value of T1 can be obtained by noting that for τ_1 much less than τ_2 , the stimulated echo's maximum amplitude decreases with τ_2 as $\exp[-\tau_2/T(\text{eff})]$, where the effective relaxation time $T(\text{eff})$, is given by

$$1/T(\text{eff}) = 1/T_1 + g(G, D, \tau_1) \quad [4-8]$$

with $g(G, D, \tau_1)$ being the diffusional contribution to second order in τ_1 . This term, for a constant steady gradient, is

given by $g(G, D, \tau_1) = \Gamma^2 G^2 D \tau_1^2$, while the functional form of $g(G, D, \tau_1)$ for pulsed magnetic field gradients is different, though the τ_1 squared dependence is maintained [Ta70]. Hence, a plot of $1/T(\text{eff})$ against τ_1 squared yields a straight line whose intercept on the ordinate yields the value of T1.

Experiment three: water-lipid contrast imaging

A novel application of the T1 weighted STE image is either the enhancement or the suppression of elements in the object with different T1 values. In a conventional spin echo image of an object with various T1 elements, the longer T1 elements may be suppressed by saturation of the signal via rapid pulse sequence repetition times. In contrast, with SIE imaging it is possible to suppress the shorter T1 elements via T1 weighting. This capability of STE imaging was clearly demonstrated by imaging a hen's egg, where the difference in the T1 values between the albumen and yolk (corresponding to a water dense and a lipid dense element, respectively) allowed for easy visualization of this STE image property.

Experiment four: chemical shift imaging

The STE is easily integrated into chemical shift imaging schemes. Any existing chemical shift imaging technique, which currently makes use of echo formation [Ma83], could benefit from the unique properties of STE imaging. Chemical shift STE imaging was conducted on a phantom consisting of a vial of water and a vial of oil, spatially separated in the y direction, but not the x direction. No readout gradient was employed so as to retain chemical shift information, and the x direction was the phase encoded direction.

Experiment five: extended STE multiecho imaging

The three $\pi/2$ rf pulse STE imaging sequence given in figure 4-1 was extended to a T1 weighted multiecho imaging

sequence as depicted in figure 4-6. The addition of a fourth $\pi/2$ rf pulse results in the formation of up to thirteen additional tertiary echoes (IE), six of which have a TI dependence in their relaxation damping term [Wo61].

The practical factors which entered into the decision as to which IE to use for imaging were as follows. With the possible production of so many echoes, it was important to locate one which could be isolated from the other echoes. By the proper choice of the time intervals τ_1 , τ_2 , and τ_3 , it was possible to create some echoes which did not overlap others. Additionally, it was desired to be able to acquire the PE, the STE, and a TE all within a single pass of the imaging sequence. Hence, since the formation of the PE and STE require $\pi/2$ rf pulses, the IE chosen for echo formation could not have a cosine tip angle dependent term, as is seen in equation 4-9 which follows.

Of primary concern was the relative intensity of the echo. For any given echo, there were three factors which acted to reduce the echo signal intensity, the tip angle dependence, the relaxation damping, and the damping due to diffusion in an inhomogeneous magnetic field. Although there were certain definite applications of the tip angle dependence term, this investigation was concerned primarily with exploiting the applications inherent in the relaxation damping term. Hence, it was advantageous to image with echoes that had a tip angle dependence as close to one as possible. Although the diffusion damping term was of

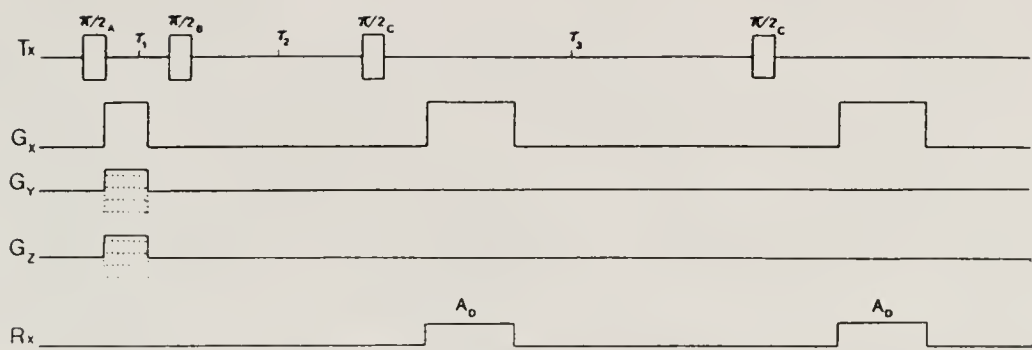


Figure 4-6. The extended stimulated echo imaging sequence.

interest, it was the form of the relaxation damping term which finally dictated which echo was to be used for image formation. It was desirable to use a TE with as simple a relaxation damping term as possible.

All these conditions were fulfilled by the TE whose maximum occurs at a time $\tau_2 - \tau_1$ after the application of the fourth $\pi/2$ rf pulse, whose amplitude at that time, $M(TE)$, is given by

$$M(TE) = -(1/2)M_i \sin\theta_1 \sin(\theta_2/2) \sin\theta_3 \sin\theta_4 * \\ \exp[-(2\tau_2/T_2 + \tau_3/T_1)] F(G, D, \tau_1, \tau_2, \tau_3) \quad [4-9]$$

where M_i is the equilibrium magnetization, θ_i represents the tip angle of the i th pulse, T_2 is the spin-spin relaxation time, T_1 the spin-lattice relaxation time, and $F(G, D, \tau_1, \tau_2, \tau_3)$ corresponds to the diffusional damping [Wo61], where G represents the magnetic field gradients and D the translational self-diffusion coefficient. The time intervals τ_1 , τ_2 , and τ_3 are defined as in figure 4-6.

This echo is a tertiary stimulated echo, resulting from the storage of the primary echo magnetization by the third rf pulse. The fourth rf pulse rotates this stored magnetization into the transverse plane for echo formation and detection. Using all $\pi/2$ rf pulses, the PE, STE, and TE were all produced and available for image formation via the execution of a single imaging pulse sequence.

In practice, the software which was resident on the imager/spectrometer permitted the acquisition of only two

echoes during a single sequence, hence the sequence had to be repeated twice so as to acquire all three echoes. The entire sequence was used each time, so this limitation did not have any effect upon the results. This problem has been resolved by the recent addition of more flexible data acquisition software.

Experiment six: TART multiecho imaging

The extended STE multiecho imaging sequence resulted in a series of images, each progressively weighted with spin-lattice relaxation. Although the underlying concept was correct, some of the intrinsic problems with the technique acted to limit its usefulness. For example, with so many echoes being generated in one pass of the sequence it often was difficult to insure that there was no overlapping of undesired echoes with desired echoes. This problem would be compounded if the sequence was extended to five, or more, $\pi/2$ rf pulses.

Fortunately, another method of forming a series of T1 weighted images was suggested by earlier work in the observation of T1 relaxation [Fr83] and zero quantum coherence [Ba80]. In both these cases, the spin system was manipulated into a given state, and the subsequent time evolution of the system was monitored with a series of sampling rf pulses, sufficiently weak so as to minimize their perturbing effect on the evolving spin system.

It was possible to apply the storage and retrieval properties of the STE (along the longitudinal direction) to

an advantage in multiecho T1 imaging. Described earlier, and illustrated in figure 4-3, the application of the first two $\pi/2$ degree rf pulses in the STE imaging sequence resulted in storing magnetization along the longitudinal direction (figure 4-3b). In the basic STE imaging sequence, all of this longitudinal magnetization was rotated into the transverse plane after a T1 weighted interval τ_2 , to form the STE image. As indicated in equation 4-7, the echo amplitude is dependent upon the sine of the third rf tip angle. Indeed, if an ideal $\pi/2$ rf pulse was used, then the resultant tip angle dependence was simply unity. Fundamental to the understanding of the TART sequence is the fact that, although the first two rf pulses of the basic STE imaging sequence resulted in a net longitudinal magnetization, there was no reason that this entire magnetization had to have been brought into the transverse plane all at once by the third rf pulse. Indeed, it was possible to bring only a portion of the magnetization into the transverse plane by using tip angles less than or equal to 90 degrees.

Figure 4-7 is the tip angle reduced T1 (TART) imaging sequence. In this version of the sequence, slice selection was determined by the first 90 degree rf pulse, applied in the presence of a magnetic field gradient, and was selective perpendicular to the z axis. The phase of the first rf pulse, A, and the phase of the receiver, B, were cycled in the same manner as the rf pulse and receiver phases in the basic STE imaging sequence. Following convention, the time

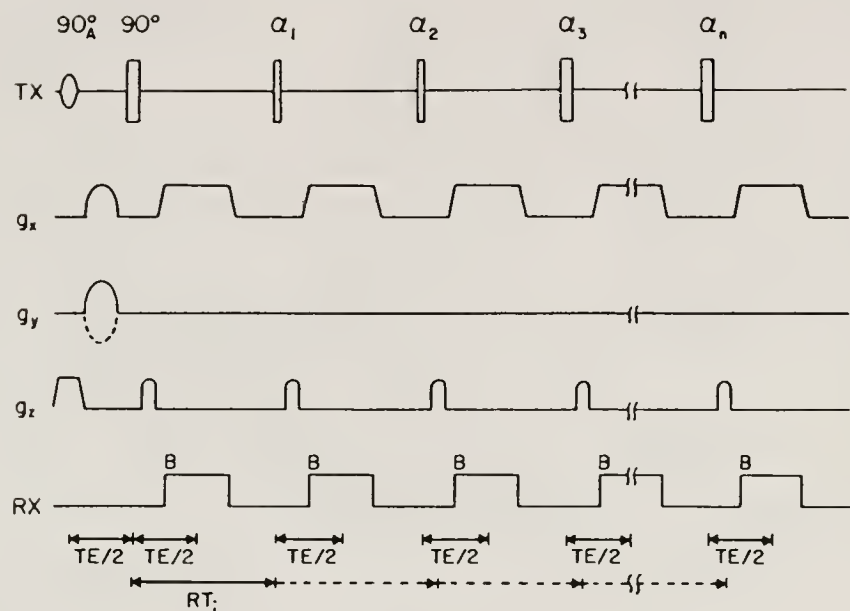


Figure 4-7. The tip angle reduced T1 (TART) imaging sequence.

from the first rf pulse to the maximum amplitude of the PE was denoted as TE , thus the time between the first and second rf pulses was $TE/2$. All phase encoding was performed during this initial interval $TE/2$, therefore the PE and the resultant series of STE images were in spatial registration. In contrast with the basic STE imaging sequence where a single 90 degrees rf pulse was used to form a single STE image, the TART imaging sequence used a series of rf pulses, whose tip angles were 90 degrees or less, to form a series of T_1 weighted STE images. The reduced tip angle rf pulses were denoted by $\alpha_1, \alpha_2, \alpha_3$, and generalized to α_n in figure 4-7. The T_1 recovery time, from the second 90 degree rf pulse to the rf pulse with tip angle α_i , was denoted as RT_i . Thus, the i th STE image had a T_1 weighting given by $\exp(-RT_i/T_1)$.

The utility of the TART imaging sequence lies in the fact that, with the correct choice of RT_i values, the entire spin-lattice relaxation curve was sampled during a single pass of the imaging sequence, with each sampling point corresponding to one of the STE images in the series. The fact that each STE shared a common T_2 dependence, given by $\exp(-TE/T_2)$, aided in simplifying the resulting echo amplitude expressions, although the expressions were complicated by the fact that each STE had a different trigonometric dependence upon the rf tip angles.

This complication was eliminated in the following manner. Figure 4-8 illustrates the use of four nonequal,

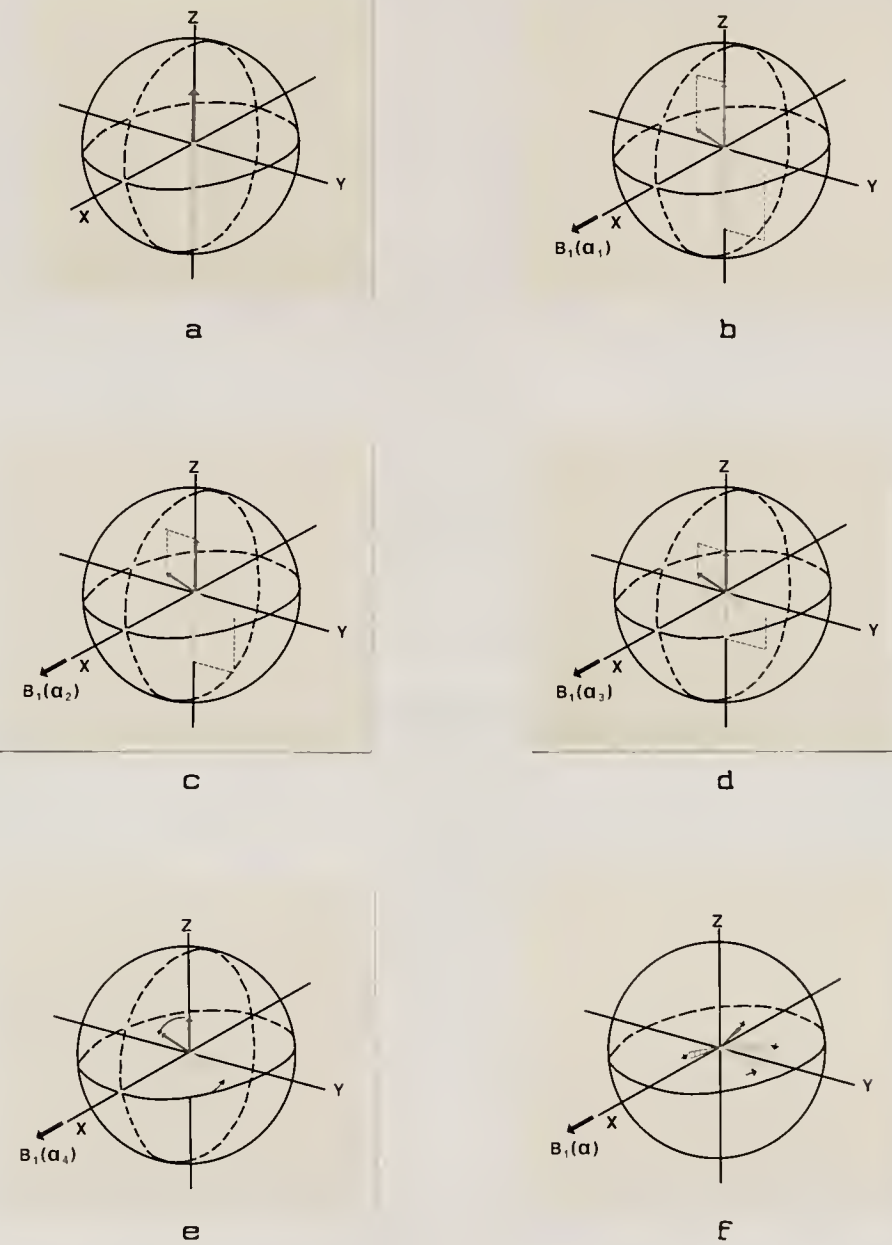


Figure 4-8. The formation of a series of TART images.

reduced tip angles to generate a series of four STE images which were identical in tip angle dependence and T2 relaxation weighting, differing solely in T1 weighting. Figure 4-8a is the longitudinal component of magnetization immediately after the second rf pulse of figure 4-7. Indeed, figure 4-8a is identical to figure 4-3b. If ideal $\pi/2$ rf pulses were used for the first two rf pulses, and T2 relaxation during the interval τ_1 is ignored, then this component is simply $(1/2)M_l$. Thus the application of the first tip angle reduced rf pulse, with tip angle α_1 , will rotate into the transverse plane a quantity of magnetization equal to $(1/2)M_l \sin \alpha_1$, leaving a quantity $(1/2)M_l \cos \alpha_1$ in the longitudinal plane. This is illustrated in figure 4-8b. The procedure is repeated, as in figure 4-8c, when the second tip angle reduced rf pulse with tip angle α_2 rotates a quantity of magnetization $(1/2)M_l \cos \alpha_1 \sin \alpha_2$ into the transverse plane, leaving a quantity $(1/2)M_l \cos \alpha_1 \cos \alpha_2$ of magnetization along the longitudinal direction. Figures 4-8d and 4-8e illustrate the application of the third and fourth reduced tip angle rf pulses. This procedure may be generalized to the application of n reduced tip angle rf pulses, where the quantity of magnetization rotated into the transverse plane, now including the relaxation terms but ignoring diffusional effects, is given by

$$S_n = (1/2)M_l \sin \alpha_n \left(\pi - \cos \alpha_1 \right) \exp \left[-(T_E/T_2 + RIn/T_1) \right] \quad [4-10]$$

where S_n is the maximum signal intensity of the n th STE. All other terms have been previously defined.

Equation 4-10 is comprised of four separate factors. One factor is the term dependent upon the total longitudinal magnetization available prior to the application of any reduced tip angle rf pulses, simply $(1/2)M_0$. This factor is the same for each STE image in the series. A second factor which is the same for each STE in the series is the T_2 relaxation damping term. A third factor, the T_1 relaxation damping term, is different for each STE image in the series, by design, for this is the source of image to image contrast. The final factor in equation 4-10 is the tip angle dependence. Although fundamentally different for each STE image, it was possible to adjust the values of the reduced tip angles in a manner which resulted in identical tip angle dependence in each STE image. This is graphically displayed in figure 4-8, where the tip angles are such that a constant amount of transverse magnetization is produced with each application of a tip angle reduced rf pulse, ignoring T_1 relaxation. Thus, when each STE in the series is formed, as depicted in figure 4-8F, the only difference in each image's maximum amplitude is the different exponential T_1 weighting. Although a qualitative argument based on figure 4-8 indicates that each successive reduced tip angle must be greater than the previous one (for the quantity of longitudinal magnetization diminishes with each rf pulse, yet it is desired to keep the quantity of induced transverse

magnetization a constant), it is possible to quantitatively determine the specific values of the reduced tip angles required.

There are two key points to consider in the development of a quantitative expression for the values of the reduced tip angles which will result in each STE image of the series having the same tip angle dependence. The first point is the most obvious, it is necessary to set the trigonometric form of the tip angle dependence of the nth STE equal to the trigonometric form of the tip angle dependence of the (n-1)th STE. For example, if n equals four, then setting $\sin\alpha_4\cos\alpha_3\cos\alpha_2\cos\alpha_1$ equal to $\sin\alpha_3\cos\alpha_2\cos\alpha_1$ results in the relationship $\sin\alpha_4 = \tan\alpha_3$. The generalized recursive relationship is given by

$$\alpha(n-1) = \arctan[\sin\alpha(n)] \quad [4-11]$$

where $\alpha(n)$ and $\alpha(n-1)$ are the nth and (n-1)th reduced tip angles, respectively.

Equation 4-11 is useful in assessing the relationship amongst the reduced tip angles, but it does not suggest any specific values. The second key point to consider is the fact that, since the nth STE image is the last of the series, a $\pi/2$ rf pulse should be used so as to rotate all the remaining longitudinal magnetization into the transverse plane. Thus, this initial (actually, final) condition, in conjunction with the recursive relation of equation 4-11, will yield all the reduced tip angles required. Listed in

decreasing order, the first ten reduced tip angles are; 90 degrees, 45 degrees, 35.26 degrees, 30 degrees, 26.57 degrees, 24.09 degrees, 22.21 degrees, 20.70 degrees, 19.47 degrees, and 18.43 degrees. Obviously, this list could be extended for any value of n , although the practical limitation is the available signal to noise ratio of the STE image. It is interesting to note that these values are invariant to the value of n . That is, the five reduced tip angles of a n equal five series are the same as the last five reduced tip angles in a, for example, n equal fifty series. The same recursive relationship has been developed by Mansfield [Ma84] for use in a different application.

The TART experiment was performed on a phantom of seven vials filled with water, and doped with copper sulfate to various concentrations. The vials were 2.5 centimeters in diameter, and were stacked so that only the wall thickness separated them. The T_1 values of the vials are given in table 4-2, in the following section. Vial seven contained a gel solution to reduce its T_2 value. Thus, any unexpected T_2 dependent weighting in the TART sequence would result in signal intensity variations, in the images of vial seven, which could not be explained by T_1 weighting. The value of TE was 15 milliseconds, and each RTI was incremented in steps of 50 milliseconds, with an initial value of 50 milliseconds. The entire pulse sequence was repeated every 715 milliseconds.

Experiment seven: diffusion coefficient mapping

In addition to characterizing an object by its relaxation times, T_1 and T_2 , and its chemical shift, NMR experiments afford the opportunity to characterize the molecular translational self-diffusion coefficient of the sample. One may utilize the T_1 dependence of the STE image indirectly to aid in spatially mapping the diffusion coefficient. Recently reported methods of in vivo diffusion coefficient measurement [Ta85, We84] rely upon the $\pi/2-\tau-\pi$ spin echo imaging technique. Since in vivo, T_1 is typically greater than T_2 , the relative effect of relaxation on signal intensity might be lessened by observing the diffusional attenuation of the STE rather than that of the PE in the $\pi/2-\tau_1-\pi/2-\tau_2-\pi/2$ sequence, or the spin echo in the $\pi/2-\tau-\pi$ sequence. A proposed imaging sequence is presented in figure 4-9.

The modification to the basic STE imaging sequence of figure 4-1 is the addition of diffusive pulsed magnetic field gradients, shown in figure 4-9 as a part of G_z . Assuming the influence of any constant background field gradient is negligible, the effect of the diffusive gradients is given by

$$F(G, D, \delta, \Delta) = \exp[-\Gamma G D \delta (\Delta - \delta/3)] \quad [4-12]$$

with δ and Δ depicted as in figure 4-9, where $\Delta = \Delta_1$ for the PE image and $\Delta = \Delta_2$ for the STE image. Hence, the T_1 dependence of the STE facilitates diffusion coefficient

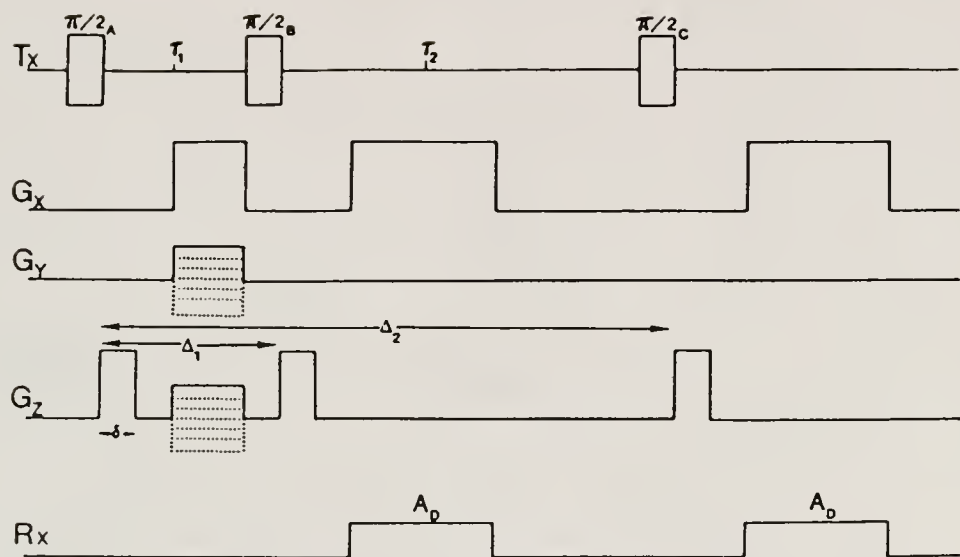


Figure 4-9. The stimulated echo-diffusion coefficient imaging sequence.

determination by permitting a greater range in $\Delta 2$ values. In sequences where relaxation damping is strictly $T2$ dependent (e.g. spin echo imaging, primary echo imaging), relaxation effects often dominate the diffusional effect. This is of primary concern in systems which undergo restricted diffusion [Wo63], for example living cells [Ta68], when it is desired to extend the diffusion effect to the maximum.

Results

Introduction

The time domain response of a spin system to three $\pi/2$ rf pulses is given in Figure 4-10. This is simply the stimulated echo rf pulse sequence, without applied pulsed magnetic field gradients, generated with the NI-80 spectrometer and presented here for illustrative purposes only. Following the notation of Figure 4-10, (a) is the response to the first $\pi/2$ rf pulse applied at time zero, with a FID following immediately. A second $\pi/2$ rf pulse was applied after a time interval $\tau 1$ equal to 400 milliseconds, with a FID following immediately. This response is noted as (b) in Figure 4-10. A PE was formed at time $2\tau 1$, 800 milliseconds from time equal zero, and is indicated in Figure 4-10 as (c). At a time $\tau 2$ equal to 675 milliseconds after the second rf pulse, a third $\pi/2$ rf pulse is applied, with a FID following immediately. This response is noted as (d) in Figure 4-10. A STE was formed at a time $\tau 1$ after the third rf pulse, 1475 milliseconds from time equal zero, and is noted in Figure 4-10 as (e). Three other secondary echoes

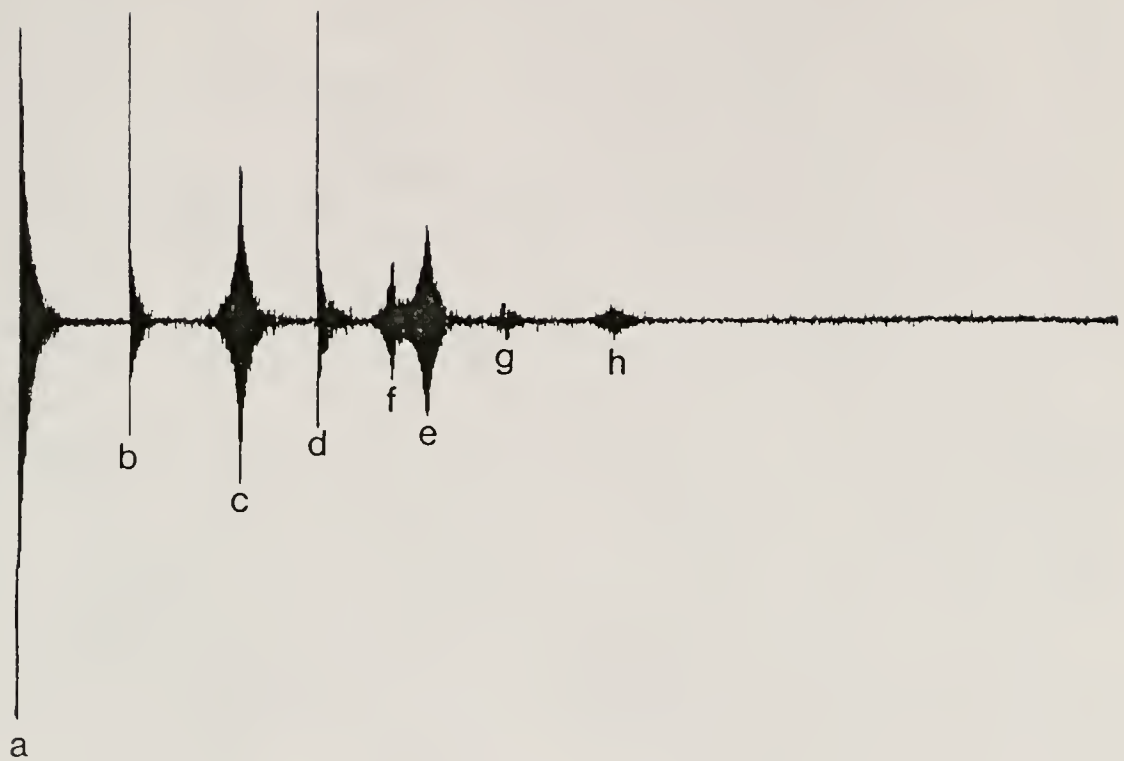


Figure 4-10. The response to the stimulated echo sequence.

are formed, denoted in figure 4-10 as (f), (g), and (h). The corresponding times were, $2\tau_2$ (1350 milliseconds from time equal zero), $\tau_1+2\tau_2$ (1750 milliseconds from time equal zero), and $2(\tau_1+\tau_2)$ (2150 milliseconds from time equal zero).

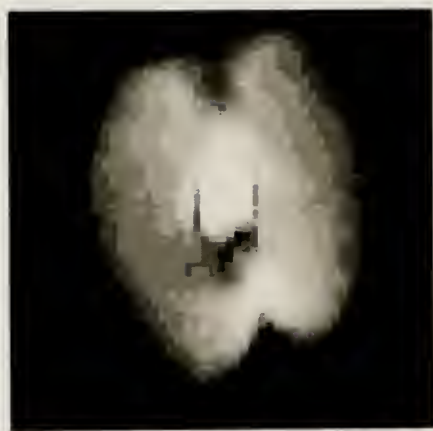
One problem associated with STE imaging is highlighted in figure 4-10. It should be noted that the STE is not temporally isolated from the secondary echo which formed at time $2\tau_2$. Artifacts would be introduced into a STE image based upon this particular STE. It was possible to adjust the values of τ_1 and τ_2 so as to isolate the STE, but this approach would result in restricting the timing parameters to certain values. As mentioned earlier, in practice a spoiling magnetic field gradient pulse was applied after the formation of the PE, but prior to the application of the third rf pulse. This spoil pulse eliminated all transverse magnetization prior to the application of the third rf pulse, thus no secondary echoes were formed.

Experiment one: T1 contrast imaging

Figure 4-11 presents typical results from a basic STE imaging sequence. The phantom shown in figure 4-11a is a red Delicious apple with a one centimeter diameter vial of copper sulfate doped distilled water embedded in its center, dubbed the "William Tell phantom." Figure 4-11b is the PE image ($\tau_1 = 20$ milliseconds), and figure 4-11c is the STE image ($\tau_1 = 20$ milliseconds, $\tau_2 = 586$ milliseconds).



a



b



c

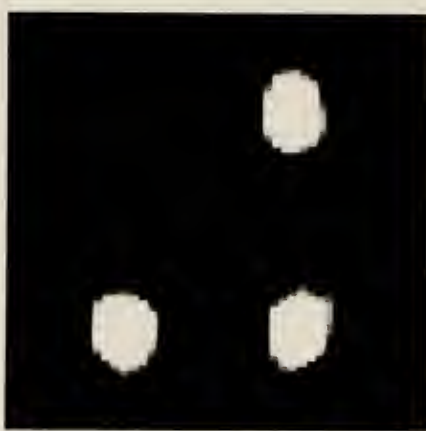
Figure 4-11. The William Tell phantom. (a) au naturel, (b) the PE image, (c) and the SIE image.

Owing to a short τ_1 value, the doped water and apple flesh did not vary greatly in intensity in the PE image. Most of the variation in intensity within the image was due to volume averaging, except for the region of low intensity directly beneath the water vial. This appeared to be the region of low flesh density where the seeds reside. The source of high intensity at the base of the apple was not known with certainty, but could be the result of a bruise.

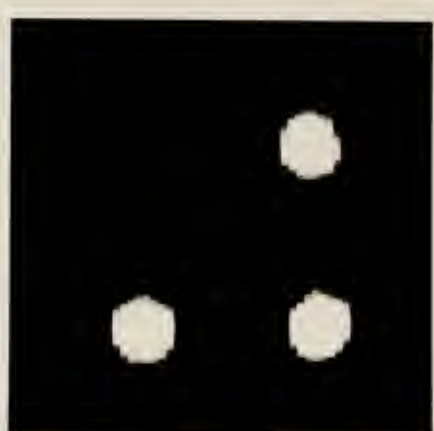
The T_1 of the doped water solution was determined to be 513 ± 17 milliseconds by an inversion recovery sequence utilizing a composite π pulse without applied gradients. In a similar fashion the T_1 of apple flesh was determined to be less than 200 milliseconds. This spread in T_1 values was dramatically demonstrated in Figure 4-11c by the STE image.

Experiment two: quantitative T_1 imaging

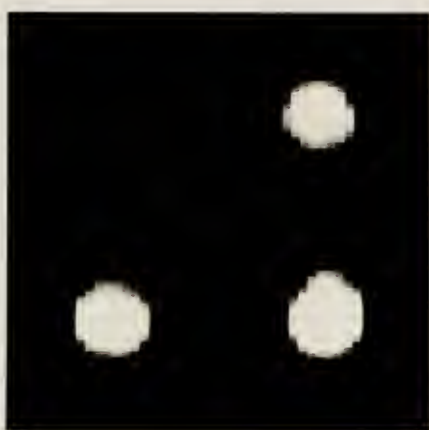
In addition to T_1 contrast imaging, STE imaging permitted quantitative measurements of T_1 values as outlined earlier. Figure 4-12 depicts the results of quantitative T_1 imaging with stimulated echoes. The phantom consisted of three one centimeter diameter vials of copper sulfate doped water. The top right vial had a T_1 of 250 ± 9 milliseconds, the bottom left vial had a T_1 of 399 ± 3 milliseconds, and the bottom right vial had a T_1 of 512 ± 17 milliseconds. These T_1 values were determined individually by an inversion recovery sequence utilizing a composite π pulse, without applied magnetic field gradients.



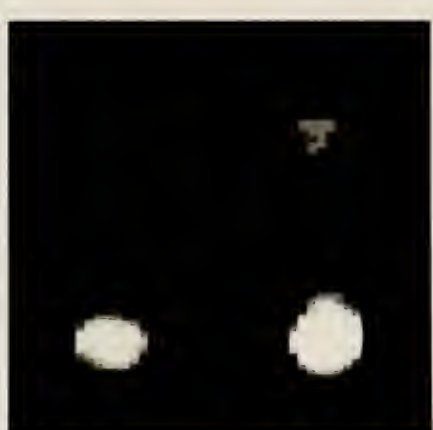
a



b



c



d



e



f

Figure 4-12. The quantitative use of the STE image.

Figure 4-12a is the PE image ($\tau_1 = 20$ milliseconds), while figures 4-12b thru 4-12f are STE images of the same phantom, each acquired with a different τ_2 value ($\tau_1 = 20$ milliseconds, $\tau_2 = 100, 250, 500, 1000$, and 1500 milliseconds respectively). The T_1 value for the bottom left vial was determined in two ways, based upon the maximum signal amplitudes of the image of that vial in each of the STE images. The first method, plotting the logarithm of the STE's maximum amplitude versus τ_2 , yielded a value for T_1 of 382 ± 2 milliseconds. This calculated value represented less than a five percent relative error when compared to the actual T_1 value. As outlined earlier, a more precise calculated value of T_1 could be determined if the effects of diffusion were considered, in the manner of equation 4-8. When the data were analyzed in the manner specified in the text following equation 4-8, a calculated value for T_1 of 388 ± 2 milliseconds was obtained, which represented less than a three percent relative error when compared with the actual T_1 value. These results were within acceptable experimental limits.

Experiment three: water-lipid contrast imaging

Figure 4-13 is a water-lipid T_1 contrast image of a hen's egg, by STE imaging. Figure 4-13b is the PE image ($\tau_1 = 20$ milliseconds), and Figure 4-13c is the STE image ($\tau_1 = 20$ milliseconds, $\tau_2 = 186$ milliseconds). Consider Figure 4-13c, where the high intensity signal is from the egg's albumen (the water dense element), the circular region of

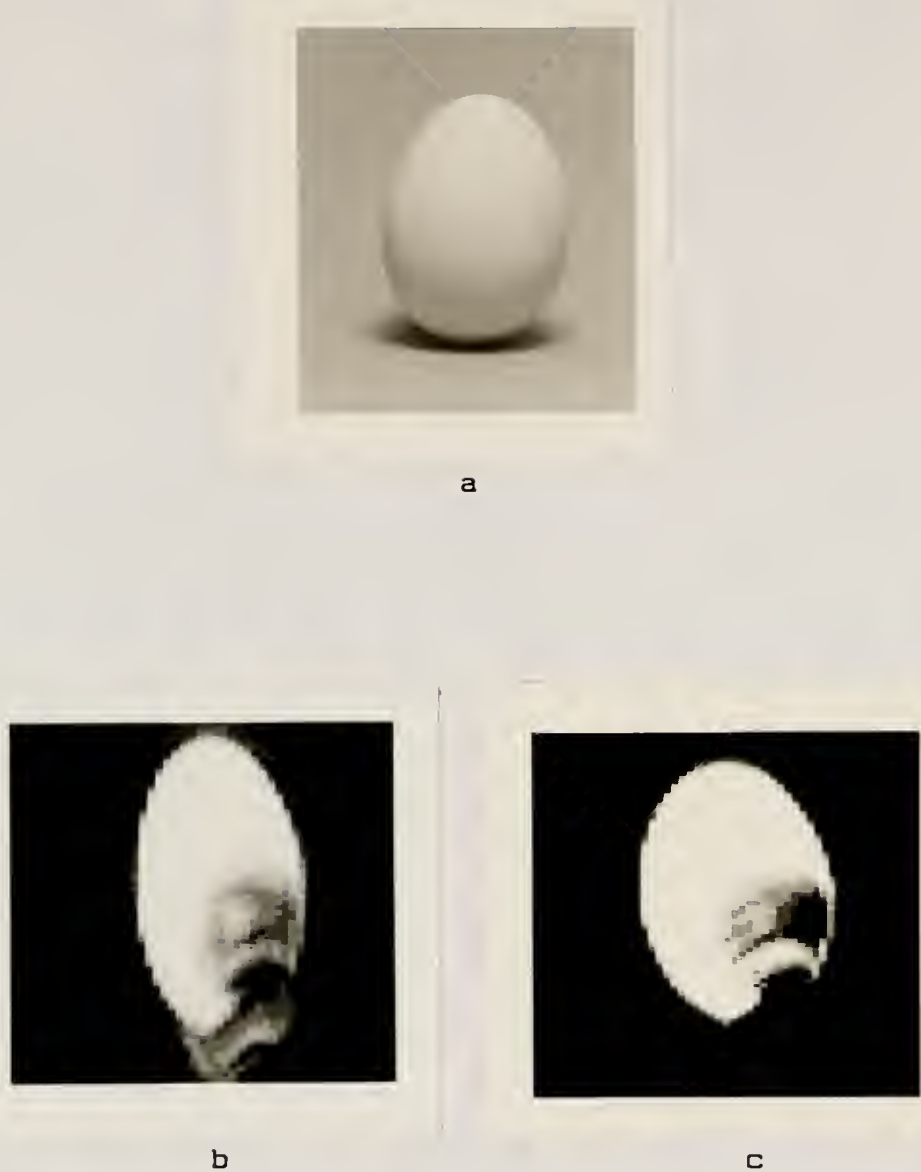
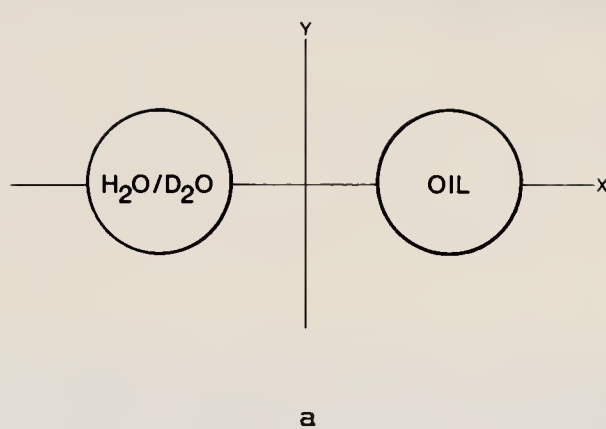


Figure 4-13. A water-lipid image of a hen's egg. (a) au naturel, (b) the PE image, (c) and the STE image.

low intensity is from the egg's yolk (the lipid dense element), and the "missing" semicircular portion near the bottom is the egg's air sac. The magnitude of the readout gradient used in both figures 4-13b and 4-13c was 0.5 mT/m, which was insufficient to overcome the lipid chemical shift from the yolk [Di84], most apparent in the PE image. This shift appears in the readout direction (vertical) of figure 4-13b, but is suppressed in figure 4-13c due to the relatively short T1 of the lipid component of the yolk. Additionally, figure 4-13b suffers from a distorted aspect ratio, owing to the influence of residual gradients. Hence, the phase encoding direction (horizontal) is reduced in figure 4-13b relative to figure 4-13c.

Experiment four: chemical shift imaging

Figure 4-14 is an example of STE chemical shift imaging. The phantom used in this experiment, depicted in figure 4-14a, consisted of two, one-centimeter diameter vials separated spatially in the y direction but not the x direction. One vial was filled with vegetable oil having a T1 of 204 ± 2 milliseconds, as determined by an inversion recovery experiment with a composite π pulse, without applied magnetic field gradients. The second vial contained a mixture of distilled water and deuterated water, having a T1 of 2.8 ± 0.1 seconds, determined in a like manner. The deuterated water was added to reduce the signal amplitude, so that the unsaturated signal intensities of the two vials were similar.



a



b

c

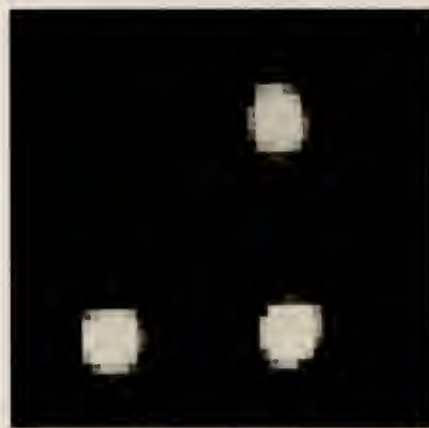
Figure 4-14. A STE chemical shift image. (a) The phantom, (b) the PE image, (c) and the STE image.

To retain chemical shift information (along the cs axis as depicted in figure 4-14), no readout gradient was employed. The x direction was phase encoded (depicted as the x axis in figure 4-14). The images are displayed as stacked plots of spectra. The PE image ($\tau_1 = 20$ milliseconds), figure 4-14b, demonstrates the near equal intensities of the two vials for short τ_1 , and the 3.5 ppm relative chemical shift. In the STE image ($\tau_1 = 20$ milliseconds, $\tau_2 = 250$ milliseconds) of figure 4-14c, the oil image is suppressed due to the large difference in T_1 between the water and oil. Each image was scaled to maximum peak intensity.

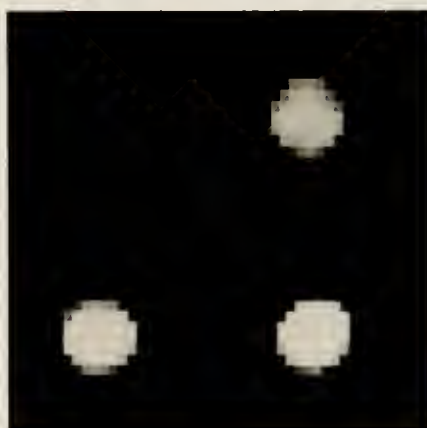
Experiment five: extended STE multiecho imaging

Figure 4-15 illustrates the results of the extended STE multiecho imaging sequence, as given in Figure 4-6. The phantom consisted of three, one centimeter diameter vials of copper sulfate doped water. The top right vial had a T_1 of 250 ± 9 milliseconds, the bottom left vial had a T_1 value of 399 ± 3 milliseconds, and the bottom right vial had a T_1 of 512 ± 17 milliseconds. All T_1 values were determined by an inversion recovery experiment utilizing a composite π pulse, without applied magnetic field gradients.

Figure 4-15a is the PE image ($\tau_1 = 20$ milliseconds), figure 4-15b is the STE image ($\tau_1 = 20$ milliseconds, $\tau_2 = 148$ milliseconds), and figure 4-15c is the TE image ($\tau_1 = 20$ milliseconds, $\tau_2 = 148$ milliseconds, and $\tau_3 = 548$ milliseconds). Note the T_1 contrast imposed on the STE image and the TE image as a function of τ_2 and τ_3 , respectively.



a



b



c

Figure 4-15. An extended SIE multiecho series of images. (a) The PE image, (b) the SIE image, (c) and the TE image.

The aspect ratio of the STE image was one, for residual gradient influence along the phase encoding direction (horizontal) was negligible for this echo. Both the PE image and the TE image were influenced along the phase encoding direction by residual gradients. The amount of influence was a function of how much time the magnetization, which was used in echo formation, spent in the transverse direction after initial phase encoding within the τ_1 interval, and the magnitude of the residual gradient during this time. The influence was greatest on the TE image, for although the PE spent a time τ_1 (equal to 20 milliseconds) in the transverse direction while in the presence of a residual gradient, the TE spent a time τ_2 (equal to 148 milliseconds) in the transverse direction in the presence of the residual gradient. Indeed, the time spent by the TE overlapped that of the PE. All images were scaled identically.

Experiment six: TART multiescho imaging

Figure 4-16 is a comparison of the images obtained with the conventional spin echo imaging sequence, and that obtained from the PE of the TART sequence. The images are presented as signal intensity contour plots. As predicted by equation 4-3, the signal to noise ratio of the PE image is reduced by a factor of two compared to that of the spin echo image. The images in figure 4-16, and all other images presented which were generated with the TART sequence, were phase encoded in the x direction (horizontal), and with the read out gradient applied along the y direction (vertical).

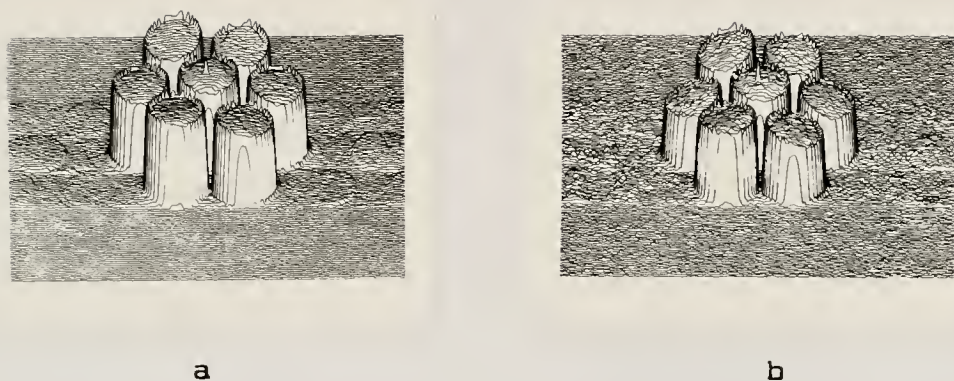


Figure 4-16. A comparison of the spin echo image and the primary echo image. (a) The spin echo image, (b) and the primary echo image.

The T1 weighted series of STE images generated by the TART sequence are depicted in figure 4-17. The images are presented as signal intensity contour plots. The recovery time, RT, progressed from 50 milliseconds in figure 4-17a, to 200 milliseconds in figure 4-17d, in 50 millisecond increments.

Qualitatively, the T1 weighted series of STE images represented the available contrast difference due to variations in spin-lattice relaxation rates. The quantitative nature of the intensity variations in the TART imaging series is represented in table 4-2. The first column of the table gives the T1 value determined for each vial by an inversion recovery experiment, where eight data points were fitted to a three parameter exponential curve. Each vial was measured separately by positioning the vial at the center of the rf coil, and operating the CSI unit as a spectrometer, without applied magnetic field gradients. Column two is simply the standard error in these T1 values estimated with the inversion recovery technique.

Column three of table 4-2 gives the T1 values determined for each vial by fitting the signal intensities from the four STE images to a two parameter exponential curve. The intensity values were determined by averaging pixels over a fixed size region within the image boundaries of each vial. Column four is simply the standard error in these T1 values estimated with the TART imaging sequence.

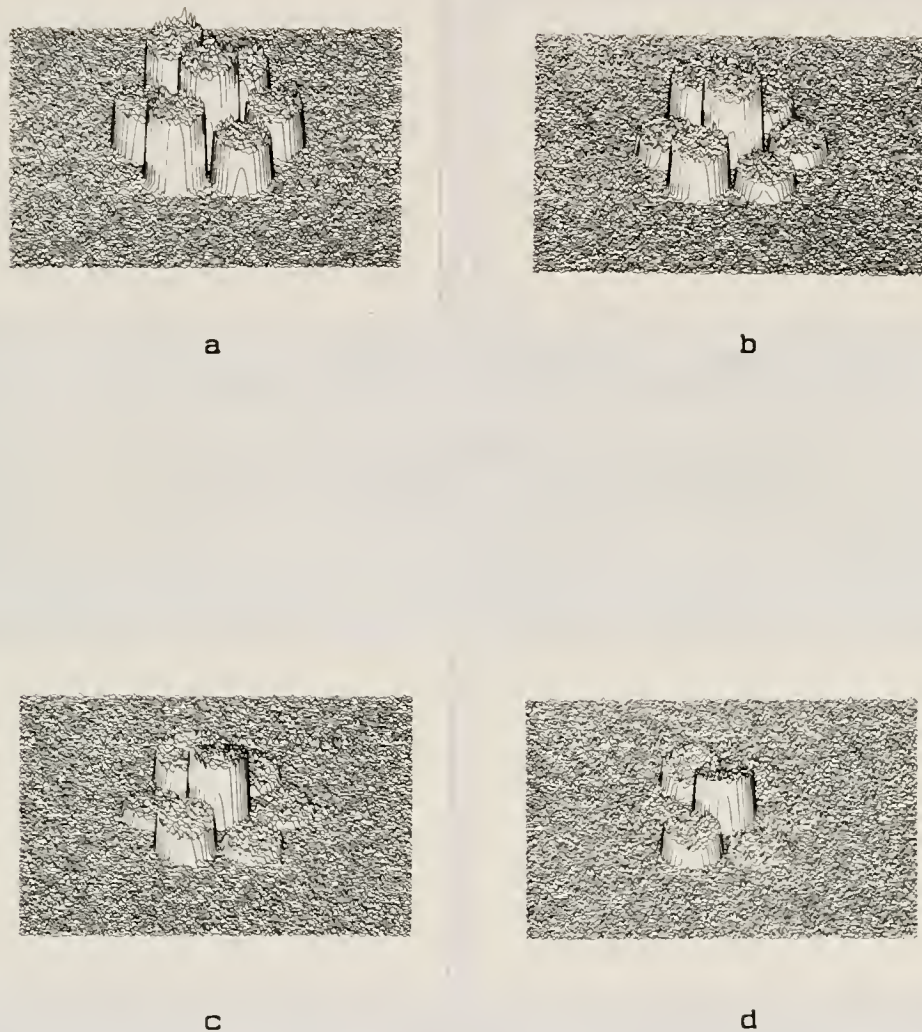


Figure 4-17. A series of TARTI images.

Table 4-2

Calculated T1 Values From Phantom in TART Experiment

Vial	IR	T1 Values (msec)	
		Standard error	TART
1	115	±0.7	103
2	63	±0.09	66
3	58	±0.04	61
4	63	±0.02	65
5	115	±0.7	117
6	64	±0.2	63
7	246	±1.7	227

Experiment seven: diffusion coefficient mapping

As indicated in figure 4-4, there was an appreciable residual gradient present after the application of a pulsed magnetic field gradient. Its influence on image quality was predominately qualitative, resulting in nonunity aspect ratios. Unfortunately, the residual gradient was sufficient to render quantitative diffusion coefficient mapping impractical, although an example of qualitative diffusion coefficient contrast imaging has recently been presented by others [Me85], which utilized an imaging sequence identical to that in figure 4-9.

Discussion

Exploiting stimulated echoes in NMR imaging involved the judicious use of the ability to store and retrieve information along the longitudinal direction, afforded by the stimulated echo. The results of this investigation took the form of specific examples which prudently used this unique property of the STE in NMR imaging. First, it was shown that in addition to generating T1 contrast images, it was possible to calculate quantitative T1 information from a series of STE images in which the storage time had been systematically varied. Second, a novel application of the T1 weighted STE image was accessed; the enhancement or suppression of elements in the object with different T1 values. Third, it was demonstrated that the STE was easily integrated into chemical shift imaging schemes. Fourth, two STE methods were developed which permitted the acquisition

of a series of STE images within one imaging sequence, where each image was progressively weighted by increasing T1 relaxation damping. Finally, a method of in vivo determination of molecular translational self-diffusion coefficients, which utilized the STE to lessen the effect of T2 relaxation, was proposed. A detailed discussion of each of these results follows.

Experiment One: T1 Contrast Imaging

The PE and SIE images of the William Tell phantom illustrated in figure 4-11 indicate that stimulated echo imaging not only works, but also works well to produce T1 contrast images. It is worthwhile to elaborate on the unexpected high intensity regions in the images. In both the PE and SIE image, there was a high intensity region at the base of the apple, hypothesized to be a bruise. Also, there is a region of high intensity surrounding the position where the cylindrical vial was located. Since the resolution of the image was 1.5 X 0.75 millimeters, and since edges were well defined in spite of volume averaging, it seems likely that the region of high intensity surrounding the vial was not a structural component of the apple, and it is suggested to be associated with apple flesh which was bruised while forcing the vial through the apple. The reason bruised apple flesh would result in increased signal intensity is explained by the following.

The full wrath of the Bloembergen, Purcell and Pound [B148] theory of relaxation need not be brought to bear

against this problem, rather, just one simple result of the theory. The result is that the spin-lattice relaxation rate is proportional to the correlation time τ_c , in the extreme narrowing situation. This result, coupled with the fact that a more mobile solution has a lower τ_c , suggests a reason why bruised apple flesh resulted in increased signal intensity.

An apple is predominately made up of water, although the flesh is quite cellular in nature, offering a natural restriction to molecular mobility. When the apple flesh is bruised, that is, when the cellular structure is broken down, the molecular mobility increases. This increased mobility results in a lower τ_c , and in turn results in an increase T_1 value. Hence, bruised regions have longer T_1 values, and would therefore appear increased in intensity over the surrounding unbruised regions.

Although the STE in figure 4-11c admirably displayed T_1 contrast, the relaxation damping of the stimulated echo is not solely determined by T_1 , for there is a $\exp(-2\tau_1/T_2)$ dependence also. To obtain a "pure" T_1 mapped image, simple post acquisition processing is required. It may be noted that the ratio of the STE's maximum, given by equation 4-7, to the PE's maximum, given by equation 4-3, $M(STE/PE)$, is given by

$$M(STE/PE) = \frac{1}{2} \left[\frac{\sin \theta_2 \sin \theta_3}{\sin(\theta_2/2)} \right] \exp(-\tau_2/T_1) * r(G, D, \tau_1, \tau_2)$$
[4-13]

where all the terms have been previously defined, with $r(G, D, \tau_1, \tau_2)$ being the ratio of the diffusional damping of the STE to that of the PE. For ideal $\pi/2$ rf pulses and negligible diffusional damping, $M(STE/PE)$ equals $\exp(-\tau_2/T_1)$, assuming the pulse sequence repetition time is sufficiently long so as to avoid additional T_1 dependence via saturation. Hence, images with strictly T_1 contrast could readily be generated from a single pass of the STE imaging sequence and appropriate post acquisition data manipulation. Furthermore, it is noted that $M(STE/PE)$ is functionally independent of θ_1 , making it insensitive to changes in θ_1 .

Experiment Two: Quantitative T_1 Imaging

The results of this experiment indicate that STE imaging is not only capable of T_1 contrast imaging, but that the STE imaging sequence may be as quantitative as the conventional inversion recovery or spin echo techniques. Indeed, STE imaging has some advantages over the conventional techniques which yield calculated T_1 values.

The conventional inversion recovery imaging sequence introduces T_1 weighting into the image by inverting the equilibrium magnetization, taken to be positive initially, along the negative z axis. The magnetization is sample by a 90 degree rf pulse as it relaxes along the z axis from the negative to the positive. Conventional state of the art NMR imagers handle this situation in one of two ways. Some instruments offer the capability of retaining this signed

information by performing a phase sensitive type of image reconstruction. This procedure is, at best, difficult to optimize when the object imaged is so diverse as the human body. The second option offered is a simple magnitude reconstruction of the image, where all signed information is lost. This approach, although simple to implement, could result in confusion when regions of the object which are equal in intensity but opposite in sign are displayed as identical. Since in STE imaging all T1 weighting is one sided (e.g. all positive), the simple magnitude reconstruction suffices to display all available T1 information without ambiguity.

Experiment Three: Water-Lipid Contrast Imaging

The images of figure 4-13 illustrate a unique feature of STE imaging, the ability to suppress the shorter T1 elements in an object by T1 weighting.

Conventional SE imaging techniques introduce T1 weighting by saturating the signal. That is, the sequence is repeated so rapidly that there is little time between repetitions for T1 relaxation. Thus, those elements with short T1 values are able to return to their equilibrium value prior to the next repetition of the sequence, whereas those elements with longer T1 values are destined, just as Sisyphus was [Ha58], to never fully regain their equilibrium value before the pulse sequence starts over. Thus, elements with longer T1 values are suppressed, whereas elements with shorter T1 values are seemingly enhanced.

In contrast, the simple $\exp(-\tau_2/T_1)$ weighting of the STE image results in the suppression of shorter T_1 elements, while longer T_1 elements are seemingly enhanced. For example, consider the case where τ_2 is 150 milliseconds, and two different elements exist in the object, one with T_1 equal to 100 milliseconds, and the other with a T_1 of 1000 milliseconds. Based solely upon this difference in T_1 values, with all else being equal, the longer T_1 element would appear nearly four times as intense as the shorter T_1 element. The clinical utility of this characteristic of STE imaging has yet to be explored. However, since many abnormalities, and in particular malignancies, have longer T_1 values, this raises tantalizing possibilities.

Experiment Four: Chemical Shift Imaging

It has been demonstrated, in figure 4-14, that the stimulated echo imaging technique is sufficiently flexible so as to permit its incorporation into any existing chemical shift imaging scheme which relies upon spin echo formation. Not only may the basic stimulated echo sequence be used in chemical shift imaging, but so may either of the two multiecho stimulated echo sequences presented in this investigation. Additionally, quantitative analysis of T_1 could easily be done for each of the chemically shifted components as outlined previously. Extension of this technique to nuclei other than hydrogen would be beneficial, for example, phosphorus, where T_1 is often much longer than T_2 [Ho75].

Experiment Five: Extended STE Multiecho Imaging

In contrast with the basic STE sequence, the extended STE multiecho sequence allows for greater T1 contrast for a given imaging time, and offers a convenient method of T1 estimation. The spin echo multipulse sequence affords similar advantages for T2 contrast imaging. The T1 weighted multiecho imaging scheme has the added advantage that, in addition to the train of T1 weighted images, the T2 weighted PE image is also produced. Thus, this single sequence yields a T2 dominated image, and a series of T1 weighted images, all in spatial registration. This would be quite useful in medical applications, where typically a spin echo image with a short echo time is useful for anatomical differentiation, and images with high T1 contrast are useful in pathological differentiation.

Experiment Six: TART Multiecho Imaging

The TART imaging sequence provides both a series of STE images progressively weighted with T1 relaxation and constant T2 weighting, and also a T2 dominated PE image. Both the spatial resolution and the total imaging times are comparable to the conventional NMR imaging techniques. Although clinical utility has yet to be realized, the flexibility of the technique promises wide applications. For all the virtues of TART imaging, there is one major vice, the reduction in the signal to noise ratio of the TART images over the corresponding spin echo image.

NMR imaging makes available a myriad of information concerning the object under investigation. Unfortunately, there is always a trade off involved, the most common one being the trade off between derived information on the one hand, and imaging time and signal to noise ratio on the other. Typically, if one wants to glean additional information from a spin system, either additional time must be spent or a reduction in the signal to noise ratio must be tolerated. This is precisely the situation in TART imaging. Additional T1 information is obtained through the series of STE images, but only by paying the price of a reduced signal to noise ratio.

The signal to noise ratio of the PE and the series of STE images may be quantified and compared to the signal to noise ratio of the conventional spin echo image. If the equilibrium magnetization is M_i , then, ignoring relaxation and diffusional damping, the maximum amplitude of the spin echo image is simply M_i . This is the ruler by which we measure the PE and STE images of the TART sequence.

As indicated in equation 4-3, the maximum amplitude of the PE image, ignoring relaxation and diffusional damping and assuming ideal $\pi/2$ rf pulses, is $(1/2)M_i$. Thus, the PE image, which has the same relaxation weighting as the conventional spin echo image, has a signal to noise ratio reduced by a factor of two. The other half of the signal to noise is available for STE image production.

If only a single SIE image is produced, then its signal to noise ratio is simply a half of that for the spin echo image. If the stored longitudinal magnetization is used to create a series of SIE images, as in the TART sequence, then the available $(1/2)M_i$ is vectorially divided amongst each SIE image. Since, in the TART imaging sequence, each SIE has the identical tip angle dependence, this factor is properly given by $\sin\alpha_1$, simply the tip angle dependence of the first SIE image in the series. Recall, the vector sum of all the SIE images in the series, neglecting relaxation and diffusion damping, must be equal to $(1/2)M_i$. For a series of n images, the vector sum of all the SIE image's maximum amplitudes, ΣM , is given by

$$\Sigma M = [(1/2)M_i \sin\alpha_1]^2 + [(1/2)M_i \sin\alpha_2 \cos\alpha_1]^2 + \dots + [(1/2)M_i \sin\alpha_n (\sin\alpha_1 \cos\alpha_1)]^2 \quad [4-14]$$

which may be simplified, as noted, by realizing each reduced tip angle term equals the first reduced tip angle term, $\sin\alpha_1$. Thus, ΣM equals the square root of $n[(1/2)M_i \sin\alpha_1]$. Since ΣM must be equal to $(1/2)M_i$, $\sin\alpha_1$ must be inversely equal to the square root of n . Thus, since $\sin\alpha_1$ is the reduced tip angle factor for all the SIE images in a TART sequence with n images, it may be said that the signal to noise ratio of each image is reduced by a factor of the square root of n . A similar result was expressed by Mansfield [Ma84] for a different application.

CHAPTER V SUMMARY AND CONCLUSIONS

The emphasis of this work was two-fold. One, the accurate and precise determination of the spin-lattice relaxation time with a conventional state-of-the-art NMR imager, and two, the application of the stimulated echo (STE), with its unique T_1 dependence, to NMR imaging.

It was shown that under certain conditions it is possible to obtain an accurate and precise estimate of T_1 with a commercial NMR imager. The most reliable method involved the acquisition of three fast inversion recovery images, with suitably chosen values of the inverting time as given in equation 3-3. If the signal intensities from these images are fitted to a three-parameter monoexponential function, then an estimated T_1 value was determined which was insensitive to whether the object was in an inhomogeneous rf field or not. The source of the field inhomogeneity may be the rf coil itself, or the rf attenuating properties of the human body which act to perturb the transmitted rf field.

Additionally, it was also shown that three spin echo images, with suitably chosen values of the pulse sequence repetition time as given in equation 3-5, could be used for T_1 estimation. In this case, the signal intensities

would be fitted to a two-parameter monoexponential function. Obtaining estimated T1 values in this fashion could be more precise and time efficient than the fast inversion recovery technique, but was always much less accurate.

The results of this work had additional value in that they could be applied a priori to aid in designing an entire imaging scheme which would result in reliable T1 estimates, or the results could be used in an a posteriori fashion, to evaluate the reliability of a calculated T1 value.

Although wide in scope and exacting in execution, this investigation did have some necessary errors of omission. By limiting the forms of the fitting functions to those suggested by the NMR spectroscopy literature, certain refinements unique to imaging were not considered [Py83]. Additionally, two-point estimates of T1 values based upon mixtures of inverting and noninverting techniques were not considered [Li85]. Never-the-less, the conclusions of this investigation are correct and useful, as long as they are utilized within the context of the study.

This work was also unique for it introduced the use of the stimulated echo for data acquisition in NMR imaging. First, it was shown that in addition to generating T1 contrast images, it was possible to calculate quantitative T1 information from a series of stimulated echo images, in which the storage time had been systematically varied. Also, a novel application of the T1 weighted STE was demonstrated:

the enhancement or suppression of elements in the object with different T1 values. Additionally, it was demonstrated that the stimulated echo could be integrated into chemical shift imaging schemes. Perhaps of most significance were the two STE imaging methods presented which permitted the acquisition of a series of STE images within one imaging sequence, where each image is progressively weighted with increasing T1 relaxation damping. Stimulated echo imaging was also shown to have the potential to be a method of in vivo determination of molecular self-diffusion coefficients.

STE imaging has certain characteristics which makes it a welcomed addition to NMR imaging. Since all STE sequences use tip angles of 90 degree or less, the instantaneous and integrated rf power deposition in the human body is less than in comparable SE imaging techniques, with no loss in the net signal-to-noise ratio. This feature indicates that STE imaging techniques might be ideal for imaging at higher frequencies, where the body is a more efficient antenna.

Since the STE may be used wherever the spin echo is currently used in NMR imaging, the spatial resolution and the total imaging time may be the same as for a conventional image. Additionally, STE imaging lends itself to multislice imaging. Thus, multislice and T1 weighted multiecho STE images could be acquired much as multislice and multiecho spin echo images are currently acquired.

Both of these investigations, although different in emphasis, were formulated based upon the same fundamental premise, that it was possible to use the microscopic properties of matter as investigative tools with which to examine the macroscopic properties of matter. Indeed, it is just this fact, that the phenomenon of NMR is based on interactions with the atomic nucleus, which gives NMR imaging the potential to be one of the most important probes yet devised with which to examine matter. Other investigative techniques which rely upon interactions with the electron energy levels of an atom have the potential to alter the chemical, or biochemical environment of the object under investigation. NMR imaging is unique in that it only slightly perturbs the nuclear energy levels of an atom, although the price paid is that the information gleaned is done so with relatively poor sensitivity. It is thought that the conclusions of these investigations into spin-lattice relaxation in NMR imaging have contributed to a more efficient use of the information which NMR imaging is able to supply.

REFERENCES

Au76 W.P. Aue, E. Bartholdi, and R.R. Ernst, J. Chem. Phys. 64:2229 (1976).

Ba81 A. Bax, R. Freeman, and G. Morris, J. Magn. Reson. 42:104 (1981).

Ba80 A. Bax, I. Mehlkopf, J. Smidt, and R. Freeman, J. Magn. Reson. 41:502 (1980).

Be84 P.T. Beall, S.R. Amtey, and S.R. Kasturi, NMR Data Handbook for Biomedical Applications; New York: Pergamon Press (1984).

Be80 E.D. Becker, J.A. Ferretti, R.K. Gupta, and G.H. Weiss, J. Magn. Reson. 37:381 (1980).

Bl46 F. Bloch, Phys. Rev. 70:460 (1946).

Bl48 N. Bloembergen, E.M. Purcell, and R.V. Pound, Phys. Rev. 73:679 (1948).

Bo78 P.A. Bottomley and E.R. Andrew, Phys. Med. Biol. 23:630 (1978).

Bo84 P.A. Bottomley, T.H. Foster, R.E. Argersinger, and L.M. Pfeifer, Med. Phys. 11:425 (1984).

Da71 R. Damadian, Science 171:1151 (1971).

Di84 W.T. Dixon, Radiology 153:189 (1984).

Do82 F.H. Doyle, J.M. Pennock, and L.M. Banks, AJR 138:193 (1982).

Du84 J.H. Duijn, J.H.N. Creyghton, and J. Smidt, Abstracts of Papers, Third annual meeting of the Society of Magnetic Resonance in Medicine, New York (1984).

Ca75 D. Canet, G.C. Levy, and I.R. Peat, J. Magn. Reson. 18:199 (1975).

Ca54 H.Y. Carr and E.M. Purcell, Phys. Rev. 95:630 (1954).

Ed80 W.A. Edelstein, J.M.S. Hutchison, G. Johnson, and T. Redpath, Phys. Med. Biol. 25:751 (1980).

Em60 M. Emschwiler, E.L. Hahn, and D. Kaplan, Phys. Rev. 118:414 (1960).

Fe57 R.P. Feynman, F.L. Vernon, Jr., and R.W. Hellwarth, J. Appl. Phys. 28:49 (1957).

Fr85 J. Frahm, K.D. Merboldt, W. Hanicke, and A. Haase, J. Magn. Reson. 64:81 (1985).

Fr71 R. Freeman and H.D.W. Hill, J. Chem. Phys. 55:3604 (1971).

Fr75 R. Freeman and H.D.W. Hill, in Dynamic NMR Spectroscopy; New York: Academic Press (1975).

Fr83 L.J. Friedman, Ph.D. Dissertation; New York: Cornell University (1983).

Gl76 P. Glorieux, J. Legrand, and B. Macke, Chem. Phys. Letters 13:567 (1976).

Gr83 J. Granot, J. Magn. Reson. 53:386 (1983).

Ha85 A. Haase and J. Frahm, J. Magn. Reson. 64:94 (1985).

Ha76 U. Haeberlen, Adv. Magn. Reson. Suppl. 1 (1976).

Ha50 E.L. Hahn, Phys. Rev. 80:580 (1950).

Ha58 E. Hamilton, The Greek Way; New York: W.W. Norton and Company, Inc. (1958).

Ha81 H. Hanssum, J. Magn. Reson. 45:461 (1981).

Ho77 D.I. Hoult, J. Magn. Reson. 26:165 (1977).

Ho75 D.I. Hoult and R.E. Rochards, Proc. R. Soc. London Ser. A 344:311 (1975).

Hr83 H. Hricak, R.D. Williams, K.L. Moon, A.A. Moss, C. Alpers, L.E. Crooks, and L. Kaufman, Radiology 147:765 (1983).

Ka78 R. Kaptein, NMR Spectroscopy in Molecular Biology; Dordrecht (1978).

Ko77 J. Kowalewski, G.C. Levy, L.F. Johnson, and L. Palmer, J. Magn. Reson. 26:533 (1977).

Kr81 R.G. Krieger, A Reference Guide to Practical Electronics; New York: McGraw-Hill, Inc. (1981).

Ku64 N.A. Kurnit, I.D. Abella, and S.R. Hartmann, Phys. Rev. Letters 13:567 (1964).

La80 M. Lausch and H.W. Spiess, Chem. Phys. Letters 71:182 (1980).

La73 P.C. Lauterbur, Nature (London) 242:190 (1973).

Le81 G.C. Levy and D.J. Craik, Science 214:291 (1981).

Li85 M.S. Lin, Magn. Reson. Med. 2:234 (1985).

Ma79 J.R. Mallard, J.M.S. Hutchison, W. Edelstein, C.R. Ling, and M.A. Foster, J. Biomed. Eng. 1:153 (1979).

Ma84 P. Mansfield, Magn. Reson. Med. 1:370 (1984).

Ma78 A.A. Maudsley, A. Wokaun, and R.R. Ernst, Chem. Phys. Lett. 55:9 (1978).

Ma83 A.A. Maudsley, S.K. Hilal, W.H. Perman, and H.E. Simon, J. Magn. Reson. 51:147 (1983).

Me85 K.D. Merboldt, W. Hanicke, and J. Frahm, Abstracts of Papers, Fourth annual meeting of the Society of Magnetic Resonance in Medicine, London (1985).

Mi72 W.B. Mims, in Electron Paramagnetic Resonance; New York: Plenum Press (1972).

Na79 K. Nagayamo, K. Wuthrich, and R.R. Ernst, Biochem. Biophys. Res. Commun. 90:305 (1979).

Nm82 NMC-1280 Manual, Nicolet Magnetics Corporation, Fremont, California (1982).

Pe81 D.T. Pegg, M.R. Bendall, and D.H. Doddrell J. Magn. Reson. 44:238 (1981).

P106 M. Planck, Vorlesungen über die Theorie der Warmestrahlung (1906).

Py83 I.L. Pykett, B.R. Rosen, F.S. Buonanno, and T.J. Brady, Phys. Med. Biol. 6:723 (1983).

Sa84 W. Sattin, L.I. Fitzgerald, and K.N. Scott, Presented at the twenty-sixth annual meeting of the American Association of Physicists in Medicine, Illinois (1984).

Sa85a W. Sattin, I.H. Mareci, and K.N. Scott, J. Magn. Reson. 64:177 (1985).

Sa85b W. Sattin, T.H. Mareci, and K.N. Scott, J. Magn. Reson. 65 (1985).

Sp61 M.R. Spiegel, Theory and Problems of Statistics; New York: McGraw-Hill Book Company (1961).

Sp80 H.W. Spiess, J. Chem. Phys. 72:6755 (1980).

St85 R.E. Steiner, AJR 145:883 (1985).

St65 E.O. Stejskal and J.E. Tanner, J. Chem. Phys. 42:288 (1965).

Su82 N.S. Sullivan, D. Esteve, and M. Devoret, J. Phys. C 15:4895 (1982).

Ta70 J.E. Tanner, J. Chem. Phys. 52:2523 (1970).

Ta68 J.E. Tanner and E.O. Stejskal, J. Chem. Phys. 49:1768 (1968).

Ta85 D.G. Taylor and M.C. Bushell, Phys. Med. Biol. 30:345 (1985).

Va76 Van Nostrand's Scientific Encyclopedia, Fifth Edition; New York: Van Nostrand Reinhold Company (1976).

Ve77 S. Vega and A. Pines, J. Chem. Phys. 66:5624 (1977).

Vo68 R.L. Vold, J.S. Waugh, M.P. Klein, and D.E. Phelps, J. Chem. Phys. 48:3831 (1968).

Wa53 R.K. Wangsness and F. Bloch, The Phys. Rev. 89:728 (1953).

We84 G.E. Wesby, M.E. Moseley, M.I. Hrovat, and R.L. Ehman, Abstracts of Papers, Third annual meeting of the Society of Magnetic Resonance in Medicine, New York (1984).

Wo61 D.E. Woessner, J. Chem. Phys. 34:2057 (1961).

Wo63 D.E. Woessner, J. Phys. Chem. 67:1365 (1963).

Zi57 J.R. Zimmermann and W.E. Brittin, J. Phys. Chem. 61:1328 (1957).

BIOGRAPHICAL SKETCH

William Sattin, born in 1957, is the son of Edward and Sallie Sattin. After attending four elementary schools, two junior high schools, and three high schools, he graduated from his secondary schooling in 1975, and entered the University of Miami in the same year. Tired of switching schools, he stayed at the University of Miami for seven years, receiving a Bachelor of Science degree in physics in 1978, a Master of Science degree in physics in 1980, and a Master of Science degree in radiological sciences in 1982. Interspersed with all this education he experienced the happiest day of his life in 1980, when he took Wendy Albin for his bride. Seeking greener pastures, he enrolled at the University of Florida in 1982, to pursue a Doctor of Philosophy degree with emphasis on nuclear magnetic resonance imaging. A most extraordinary set of circumstances have recently left him a father, to Emily Albin Sattin, aged three months.

I certify that I have read this study and that in my opinion it conforms to acceptable standards of scholarly presentation and is fully adequate, in scope and quality, as a dissertation for the degree of Doctor of Philosophy.

K. N. Scott

Katherine N. Scott, Chairman
Associate Professor of Nuclear
Engineering Sciences

I certify that I have read this study and that in my opinion it conforms to acceptable standards of scholarly presentation and is fully adequate, in scope and quality, as a dissertation for the degree of Doctor of Philosophy.

Alan M. Jacobs

Alan M. Jacobs
Professor of Nuclear Engineering
Sciences

I certify that I have read this study and that in my opinion it conforms to acceptable standards of scholarly presentation and is fully adequate, in scope and quality, as a dissertation for the degree of Doctor of Philosophy.

E. Raymond Andrew

E. Raymond Andrew
Professor of Nuclear Engineering
Sciences

I certify that I have read this study and that in my opinion it conforms to acceptable standards of scholarly presentation and is fully adequate, in scope and quality, as a dissertation for the degree of Doctor of Philosophy.

Leon W. Couch

Leon W. Couch
Professor of Electrical
Engineering

I certify that I have read this study and that in my opinion it conforms to acceptable standards of scholarly presentation and is fully adequate, in scope and quality, as a dissertation for the degree of Doctor of Philosophy.

James R. Brookeman

James R. Brookeman
Associate Professor of Physics

I certify that I have read this study and that in my opinion it conforms to acceptable standards of scholarly presentation and is fully adequate, in scope and quality, as a dissertation for the degree of Doctor of Philosophy.

Thomas H. Mareci

Thomas H. Mareci
Assistant Professor of Radiology

This dissertation was submitted to the Graduate Faculty of the College of Engineering and to the Graduate School and was accepted as partial fulfillment of the requirements for the degree of Doctor of Philosophy.

December, 1985

D. G. Shaffer

Dean, College of Engineering

Dean, Graduate School

UNIVERSITY OF FLORIDA



3 1262 08554 1380